Probing the dynamics of nanoparticles at oil-water interfaces using high-speed total-internal-reflection dark-field microscopy

Anne Y. Schumacher

Exeter College

University of Oxford

Supervisor: Prof. Philipp Kukura

A thesis submitted for the degree of

Doctor of Philosophy (DPhil) in Physical and Theoretical Chemistry

August 7, 2020

List of publications

The work I carried out between October 2015 and July 2020 led to the following publications:

1. X. Meng, A. Sonn-Segev, **A. Y. Schumacher**, G. T. Young, D. Cole, S. Thorpe and P. Kukura, Towards maximally efficient single particle tracking with total-internal reflection-based darkfield microscopy, to be submitted.

2. **A. Y. Schumacher**, A. Sonn-Segev and P. Kukura, Probing the dynamics of nanoparticles at oil-water interfaces using total-internal reflection dark-field microscopy, to be submitted.

Contents

1 Introduction **1**
- 1.1 Applications of particles at fluid interfaces . . . 1
  - 1.1.1 Pickering emulsions . . . 2
  - 1.1.2 Chemical synthesis . . . 4
  - 1.1.3 Basic science . . . 6
- 1.2 Behaviour of particles at liquid-liquid interfaces . . . 8
  - 1.2.1 Stability . . . 10
  - 1.2.2 Dynamics of single particles . . . 13
  - 1.2.3 Inter-particle interactions . . . 18
  - 1.2.4 Surfactants . . . 20
  - 1.2.5 Expected time scales for nanoparticle dynamics . . . 24
- 1.3 Scope of this thesis . . . 28

2 Experimental **30**
- 2.1 Selecting a particle-tracking method . . . 30
  - 2.1.1 Interferometric scattering vs. dark-field microscopy . . . 33
  - 2.1.2 High-performance dark-field microscopy . . . 36
- 2.2 Preparation of liquid-liquid interfaces . . . 40
  - 2.2.1 Development of a suitable protocol . . . 42
    - 2.2.1.1 Producing a planar oil-air interface contained by a grid . . . 44
    - 2.2.1.2 Producing a stable oil-water interface . . . 48
    - 2.2.1.3 Planarity . . . 51
    - 2.2.1.4 Contaminants . . . 52
  - 2.2.2 Preparation of water-on-silicone oil interfaces . . . 53
  - 2.2.3 Materials . . . 56
- 2.3 Total-internal-reflection dark-field microscopy . . . 59
  - 2.3.1 Detailed description of the experimental setup . . . 60
  - 2.3.2 Camera characterisation: Quantifiying the signal . . . 64
  - 2.3.3 Signal-to-background and signal-to-noise ratios . . . 70
  - 2.3.4 Localisation precision . . . 72

3 Analysis Methods **77**
- 3.1 Observables . . . 78
  - 3.1.1 Observables obtained directly from the tracking algorithm . . . 78
  - 3.1.2 Diffusive behaviour . . . 84
  - 3.1.3 Deviations from averaged behaviour . . . 89
- 3.2 Data analysis . . . 94
  - 3.2.1 Visualisation . . . 95
  - 3.2.2 Tracking algorithm . . . 97

3.2.2.1 Detection 99
3.2.2.2 Linking frames into trajectories 104
3.2.3 Patterned noise from the camera 107

4 High-speed dynamics of single nanoparticles at oil-water interfaces 109
4.1 Method and expected results 109
4.2 Results 111
4.2.1 Representative trajectories 111
4.2.2 Ensemble diffusion analysis 114
4.2.3 Scattering intensity 117
4.2.4 Correlation between scattering intensity and diffusion 121
4.2.5 Displacement distributions 123
4.2.6 Confinement of larger particles 127
4.3 Summary and discussion 130

5 Out-of-plane dynamics of nanoparticles at oil-water interfaces 133
5.1 Method and expected results 135
5.2 Identification of partially adsorbed states and transitions between states 137
5.3 Results 142
5.3.1 Adsorptions 144
5.3.2 Desorptions 150
5.3.3 Skims 153
5.3.4 Other partially adsorbed states 158
5.3.5 Transitions between immersion states 160
5.4 Summary and conclusions 162

6 Summary and future directions 165
6.1 Methods 165
6.2 Results and implications 167
6.3 Future directions 171

7 Appendix 184
7.1 Reduction of interfacial energy 184
7.2 Time dependence of experimental variables 185
7.3 Correlation between scattering intensity and instantaneous diffusion coefficient 186
7.4 Towards probing the interfacial potential energy landscape . . 187

Abstract

Particles at fluid-fluid interfaces have a wide range of powerful uses in industry, technology and science. There is therefore a strong interest in exploring the dynamics of these systems — to understand and gain more control in applications, as well as for fundamental investigations in condensed matter and statistical physics. Questions remain in particular about what governs adsorption dynamics and inter-particle interactions, and how mixtures of different-sized particles as well as particles and surfactants behave.

This thesis probes the dynamics of nanoparticles at oil-water interfaces using high-speed total-internal-reflection dark-field (TIR-DF) microscopy, comparing gold particles of diameters 20, 40 and 80 nm, and investigating the effect of an added surfactant (n-dodecyl-β-D-maltoside (DDM)). We built a TIR-DF microscope with a spatiotemporal resolution of up to 1 nm and 20 μs, and used home-written tracking and analysis software to characterise the particle motion. The diffusive motion within the interfacial plane is measured directly; out-of-plane motion is inferred from light scattering and in-plane motion.

The addition of DDM was found to qualitatively alter the interaction between the particles and the interface, with adsorptions becoming reversible and an

inversion of the size trend in diffusivity (with larger particles diffusing faster than smaller ones, contrary to expectations). This, in combination with a paucity of adsorption events in larger particles, leads us to propose size-dependent barriers to adsorption to DDM interfaces. In addition, at DDM interfaces, many particles' diffusive behaviour changed over the course of a trajectory, indicating several different immersion states that are stable on the experimental timescale ($\approx$1 s).

This study shows that there remain qualitatively new dynamics of nanoparticles at oil-water interfaces to be explored. These dynamics can only be resolved at a high spatial resolution, and many of them only at high imaging speed, underlining the importance of novel imaging approaches probing the barriers of achievable spatiotemporal resolution.

1 Introduction

The study of particles at liquid-liquid and liquid-gas interfaces has resulted in a wide range of applications both in technology and science. It has become a highly dynamic and interdisciplinary field in recent years as many long-established applications are not understood on a fundamental level while new ones continue to emerge. [1]

The most important applications of particles at liquid-liquid interfaces are listed in section 1.1. Section 1.2 summarises what is currently known about the dynamics and some open questions of current interest. Section 1.3 presents the aims of this thesis.

1.1 Applications of particles at fluid interfaces

Important applications include the stabilisation of soft and porous materials such as gels, emulsions and foams [2, 3, 4, 5] (section 1.1.1), new synthetic approaches using self-assembly [6] (section 1.1.2), and applications in fundamental research (section 1.1.3), including advances in thermodynamics [7], statistical physics [8] and colloid and interface science [9, 10, 11].

1.1.1 Pickering emulsions

Emulsions are mixtures of two or more immiscible liquids in which one is distributed in the other in the form of microscopic droplets. They have numerous applications in industry, as well as occuring naturally in many food items and elsewhere. Typically, artificial emulsions de-emulsify (separate into the component phases) over time if they are not stabilised — stabilisation can be achieved using materials that form films at the interfaces between the liquids, preventing coalescence.

Traditionally, this has been achieved using small-molecule and sometimes macromolecular surfactants, but in pharmaceutical applications these can cause allergy-like reactions and be carcinogenic. Particle-stabilised emulsions (Pickering emulsions, see Fig. 1.1a) offer a more stable, biocompatible and environmentally friendly alternative [12].

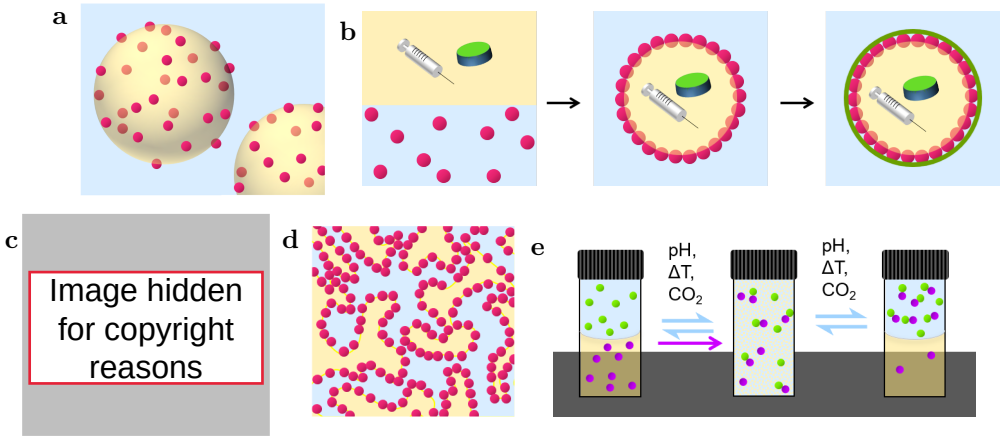


Figure 1.1: Pickering emulsions and applications. a) Oil droplets (yellow) in water (blue) can be stabilised against coalescence by particles (pink) at the oil-water interface. Hydrophilic particles favour oil-in-water emulsions, hydrophobic ones water-in-oil emulsions. b)-d) Emulsion templating can be used to fabricate nano- and microstructured materials such as colloidosomes (b) with tunable shell permeability and porous materials (c, SEM image of a porous surface modified from *Macromolecules* 2009, *42*, *23*, 9289) and d) bijels. e) Emulsification can be made reversible by adding functional groups to particles that alter their wetting properties in different conditions (e.g. pH, temperature and CO_2 concentration). If they are very hydrophilic or very hydrophobic, they will become unstable at the interface, leading to phase separation. In this example, a reaction between reactants with different solubilities is effected by emulsification, and the product is separated from the emulsifier (at the interface; not shown) by triggering demulsification.

They have been widely used for many decades in the oil, food and cosmetics industries, and have more recently found use in high-tech applications. This includes the fabrication of structures such as microcapsules (see Fig. 1.1b) [4] and porous scaffolds for tissue engineering [13] (Fig. 1.1c). This method could be used to circumvent issues with current methods in the produc-

tion of synthetic bone scaffolds [14], such as toxicity from metal catalyst residues. Other applications include pharmacy and biomedicine [12], where Pickering emulsions have shown improved drug release behaviour [15, 16] over emulsions stabilised by (commonly used) synthetic surfactants, which can be toxic and have unfavourable mass transport properties. New and interesting structures such as bijels [17, 5] — bicontinuous morphologies of two immiscible fluids (Fig. 1.1d) — can be fabricated using particles, furnishing powerful materials and reaction media (see e.g. Refs. [18] and [19]). More generally, emulsions are a very promising environment for catalytic reactions, but this is currently limited by the difficulty of separating products from catalysts and surfactants. The use of stimuli-responsive Pickering emulsions is a method that could overcome this challenge [3] (Fig. 1.1e) by providing precise control over mesoscopic properties of the system.

1.1.2 Chemical synthesis

Particles at fluid interfaces can undergo self-assembly. This has been explored as a viable bottom-up approach in chemical synthesis that enables the facile production of complex two-dimensional structures that would otherwise be difficult, resource- and time-intensive and expensive, or impossible

to achieve [6, 20] (see Fig. 1.2).

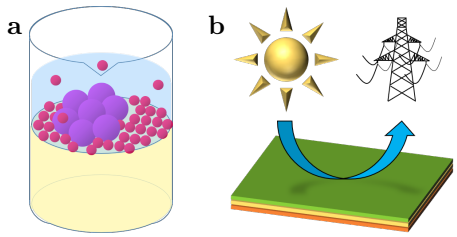


Figure 1.2: The dynamics of particles at fluid-fluid interfaces underlie self-assembly processes. a) Control over particle dynamics at liquid-liquid interfaces affords powerful and simple new synthesis routes based on self-assembly. This enables the fabrication of b) nanostructured materials such as thin films, with applications in energy, sensing, filtration and more.

Thin films have important applications for example in microelectronics and photonics [21] and solar energy technology. Interfaces can act as highly reproducible and defect-free templates for two-dimensional particle structures, and the use of nanoparticles (1-100 nm) rather than larger particles opens up new synthesis mechanisms due to size-dependent effects [22]. The resulting nanomaterials are expected to exhibit significantly different behaviours from larger-scale matter, with improved mechanical [23], electrical [24, 25] and other properties, as well as quantum effects that are of both fundamental and practical interest (see e.g. Ref. [26]). Precise control over the self-assembly processes of nanoparticles is a current goal [20, 3] for technological reasons: Smaller structures have a higher surface to volume ratio,

increasing chemical activity. Additionally, size effects become relevant at this scale, which can give rise to tunable optical and electromagnetic properties (see e.g. Ref. [25]).

1.1.3 Basic science

Particles at fluid interfaces can serve as model systems for a wide range of structures and processes that are difficult to investigate experimentally, but for which more knowledge is desirable [27, 9, 28] (see Fig. 1.3).

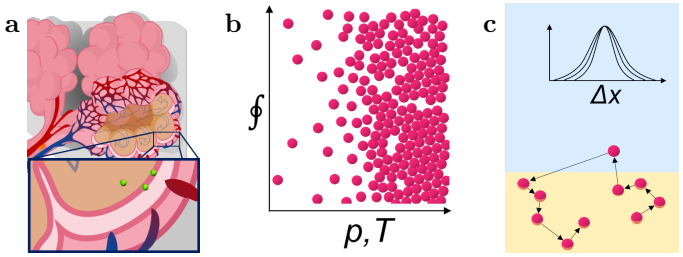


Figure 1.3: The dynamics of particles at fluid-fluid interfaces can be used to model other phenomena. a) Particles at liquid-air interfaces can serve as a model system for interactions between particulate matter and lung tissue, as well as other transport phenomena involving interfaces. Image modified from https://en.wikipedia.org/wiki/Pulmonary˙alveolus, accessed 12/04/2020. b) Particles undergo phase transitions in two dimensions, governed by properties of as well as paths undergone by the system. c) Diffusion gives insight into stochastic processes.

For example, the interaction between small particles and pulmonary surfactant (the layer coating the alveoli in the lungs, see Fig. 1.3a) can be modeled

with particles at liquid-air interfaces [28]. This is a very topical issue, with both long-established and recent evidence [29, 30, 31] for a link between particulate air pollution and lung disease as well as other health issues, but little understanding of the detailed mechanism that leads to structural and functional changes in the airways [32]. A better understanding could guide decision-making, for example by providing information on the risks from different particle types. More generally, interactions between particles and interfaces are important to the fundamental understanding of transport phenomena, especially in living organisms, as they contain vast interfacial areas. An example that has been gaining in importance is the distribution of nanoscopic materials released into the environment, which is not well understood [33, 34]. Analogies also exist with particle-membrane interactions [27] or the nano-bio interface [11], in which there has been a strong interest for both practical (see e.g. Ref. [35]) and fundamental reasons for some time.

Finally, investigations into the dynamics of nanoparticles at liquid-liquid interfaces can help answer more general questions in physics. Examples include probing length scale-dependent minimum-energy configurations on curved surfaces [36] and phase transitions in two-dimensional systems [7, 5, 37] (Fig. 1.3b) — for example, out-of-equilibrium systems and glass formation are important, but poorly explained. More generally, diffusion

analysis (Fig. 1.3c) can be used to study the relationship between structure, properties and dynamics: Microrheology studies work best with particles [10], enabling the characterisation of soft matter on the microscopic scale relevant to biological and other processes. Recent results from statistical physics [8] include findings on Brownian first-passage times, which are relevant to reaction rates, and the question of whether the motion of a single particle converges to an ensemble-averaged motion and how long observation times need to be for measurements to provide the same result. Furthermore, interpretations of anomalous (non-Gaussian) diffusion are being developed (see section 1.2.2), with experiments from the last few years [38] observing these unexpected dynamics.

1.2 Behaviour of particles at liquid-liquid interfaces

This section gives an overview of the forces that govern the dynamics of particles at liquid-liquid interfaces. There are many open questions that are directly relevant to both established and potential applications. The dynamics of adsorption and desorption of particles to and from the interface are interesting in themselves, relevant to motion within the interface, and could be used to probe the potential energy landscape of the interface (see

section 1.2.1). Inter-particle interactions both within the interface and between particles at the interface and particles in the bulk liquid are directly relevant to self-assembly processes. Systems with mixtures of different particles, as well as particle-and-surfactant mixtures, are relevant in practical applications. These dynamics and forces, as well as the role of interfacial rheology in the dynamics and the relationship between the structure of the system and its properties, are all poorly understood [1, 20, 39, 40]. Recent findings illustrate that particles at interfaces exhibit rich behaviours that are only just being discovered, some of which will be discussed in the following sections.

Below, I will introduce the energy considerations that lead particles to adsorb to the interface (section 1.2.1) and the single-particle dynamics at the interface (section 1.2.2). Particle-particle interactions mediated by the interface are briefly discussed in section 1.2.3, and section 1.2.4 examines the effects of adding a surfactant to the system. Finally, section 1.2.5 gives an overview of the time scales associated with the particle dynamics. In this work, I will only consider oil-water interfaces; however, many principles also apply to other liquid-liquid interfaces.

1.2.1 Stability

The strong interaction between particles and interfaces underlying the stability of Pickering emulsions was discovered in the early 20^{th} century [41], [42], explained theoretically in 1980 [43] and confirmed experimentally in 2003 [22]. It is driven by the reduction of interfacial energy, which can be understood in immiscible fluids to arise from less energetically favourable interactions between different species of molecules compared to interactions within a species. The interfacial energy is related to the interfacial area A via $E_{\text{i}} = \gamma_{\text{i}} A$, where γ_{i} is the interfacial tension. Analogously, the contact line between the three phases (particle and two liquids) gives rise to a contact line energy $E_{\text{cl}} = \tau L$, where τ is the line tension and L the length of the contact line. The energy difference between the adsorbed state with contact angle θ (defined in Fig. 1.4c) and the state in which the particle is completely surrounded by one phase (see Fig. 1.4) can thus be estimated by the difference in the sum of interfacial energy terms of the system and a contribution from the contact line:

$$\Delta E = \gamma_{1\text{p}} \Delta A_{1\text{p}} + \gamma_{2\text{p}} \Delta A_{2\text{p}} + \gamma_{12} \Delta A_{12} + \tau L. \tag{1}$$

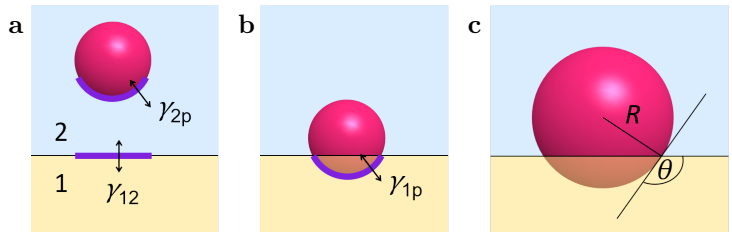


Figure 1.4: Schematic of a spherical particle adsorbing to an interface, with associated interfacial energy terms, and definition of the contact angle. a) Before and b) after adsorption. Interfacial areas that are eliminated (a) or formed (b) during the adsorption process are highlighted in purple and labeled with their interfacial tensions (see Eqn. (1)). c) Particle with radius R adsorbed at a liquid-liquid interface with contact angle θ, related to the immersion depth z via $z = R(1 + \cos(\theta))$.

The equilibrium state is determined by minimising the energy in Eqn. (1). The interfacial energy terms scale with R^2 and the line tension term with R, where R is the particle radius. Therefore, for sufficiently large particles ($R \gg \tau/\gamma_{12}$ [9]), the line tension can be neglected. In this case, the equilibrium contact angle θ_0 is given by $\cos(\theta_0) = (\gamma_{2p} - \gamma_{1p})/\gamma_{12}$, known as Young's equation. For a particle adsorbing to the interface from phase 2, this yields (see section 7.1 appendix) an equilibrium interfacial stabilisation energy [43]

$$\Delta E = -\pi R^2 \gamma_{12} (1 + \cos\theta_0)^2, \tag{2}$$

The adsorption energies of nanoparticles, on the order of $\Delta E \lesssim 10\ k_B T$ (see

Fig. 1.5), are often small enough to allow desorption at room temperature [22, 44]. Low interfacial tensions and equilibrium contact angles far from 90° favour desorption; for a typical interfacial tension between silicone oil and water [45, 46] and an equilibrium contact angle of 170°, a particle as large as 100 nm in diameter has a stabilisation energy of only 17 $k_{\mathrm{B}}T$, whereas a 1 μm particle with an equilibrium contact angle of 150° has a stabilisation energy of over 10^5 $k_{\mathrm{B}}T$. Very large contact angles lead to low binding energies even for large particles.

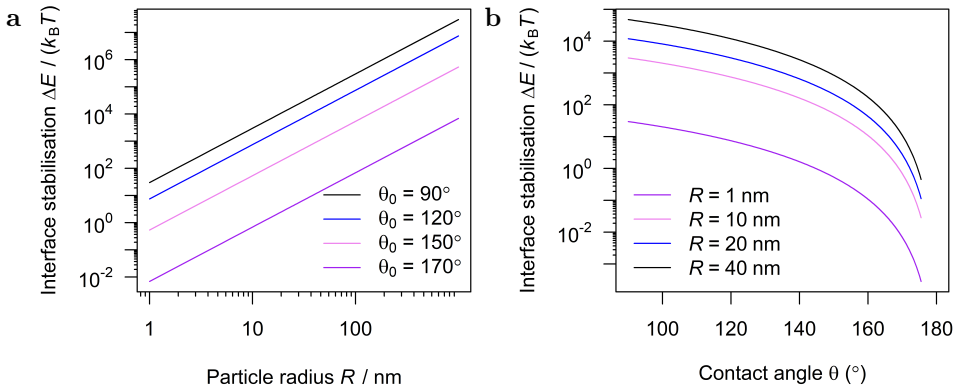


Figure 1.5: Predicted interface stabilisation energy according to equation (2), where $\gamma_{12} = 39$ mNm^{-1}. a) As a function of particle radius. b) As a function of three-phase (see Fig. 1.4c) contact angle between 0 and 175°.

The effect of the line tension on the equilibrium contact angle can be derived using the same principles as Eqn. (2). The adsorption energy scales with R^2 on the basis of the interfacial area and with R on the basis of the contact

line. The stability of small particles is therefore more likely to be affected by the contact line than that of larger particles [9]. The contact line is also likely to affect the interfacial diffusion of small particles disproportionately [47] (see section 1.2.2). However, the line tension is experimentally difficult to measure, and a wide range of values, between 1 and over 10^6 $k_\mathrm{B}T$, both positive and negative, have been reported for various systems [9]. It is omitted here as determining it in this work would require access to both γ_{12} and the equilibrium contact angle of particles at the interface, as well as the requirement to account for slower diffusion due to interfacial fluctuations [48] (see section 1.2.2).

1.2.2 Dynamics of single particles

Once adsorbed to the interface, particles within the micrometer (1-100 μm) size range that has so far been typical for the applications above undergo two-dimensional Brownian motion within the interfacial plane, with little motion perpendicular to the interface [49]. Brownian motion is characterised using a diffusion coefficient that relates the spread of the particle's probability distribution function with time (see section 3.1 for details). In the bulk, the diffusion coefficient is given by the Stokes-Einstein equation

$$D = \frac{k_\mathrm{B}T}{6\pi R_\mathrm{h}\eta}, \tag{3}$$

where k_B is the Boltzmann constant, T is the temperature, R_h is the hydrodynamic radius of the particle and η is the viscosity of the surrounding medium. For a particle adsorbed at an interface between two liquids with different viscosities η_1 and η_2 with a contact angle θ as defined in Fig. 1.4c, Eqn. (3) can be modified to yield [44]

$$D = \frac{k_\mathrm{B}T}{6\pi R_\mathrm{h}} \frac{2}{\eta 1 + \eta 2 + (\eta 1 - \eta 2)\cos\theta}, \tag{4}$$

which expresses an overall viscosity as a linear combination of the two viscosities where the contributions of the two phases are proportional to the particle's respective immersion depth in them.

However, experimental studies have shown that — while the Stokes-Einstein law holds in the bulk [50, 51] — particles have been found to diffuse more slowly at interfaces than they would in the bulk phase with the higher viscosity [52, 48]. One study proposed a quantitative model of fluctuations of the interface at the contact line [48] (see Fig. 1.6), with either a hopping

contact line (Fig. 1.6a) moving between favourable areas of the particle surface (determined by shape or surface chemistry), or a fluctuating interface slope along a pinned contact line (Fig. 1.6b) proposed to explain anomalously slow diffusion at a water-air interface. However, this unexpectedly slow diffusion at the interface does not always occur, as shown in Ref. [44]. More sensitive experiments are required to understand this phenomenon.

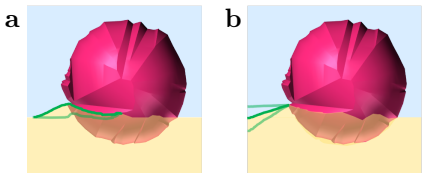


Figure 1.6: Models for slower diffusion due to surface inhomogeneities. Fluctuations at the three-phase contact line suggested in Ref. [48]. Green lines indicate alternative contact line and interface positions. a) Hopping contact line. b) Pinned contact line with fluctuation in interfacial slope.

Another diffusive behaviour that contains information on the interaction between the particle and the interface is the particle's displacement distribution. According to the central limit theorem, the displacement distribution of Brownian motion is expected to be Gaussian in the long-term limit, but experiments have found that the distribution often deviates from this form [38]. This deviation is often a result of different diffusive processes [53], which could be expected to disappear with longer observation times, but

it can also arise from confinement [54] and fundamentally different diffusive dynamics, such as in the case of an imperfect ensemble [55] or different metastable immersion states. The underlying statistics and mechanisms are currently under investigation (see e.g. Ref. [55]), and are of fundamental interest as well as relevant to understanding event cascades for example in biological signalling and pathway-dependent processes in materials science [38]. Previously suggested models (see Fig. 1.7) include exponential tails caused by rare hopping events (e.g. Ref. [53]) and the sampling of several different diffusion states, as well as power-law tails and other forms [55].

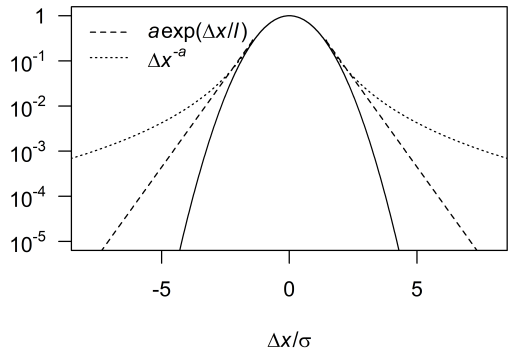


Figure 1.7: Gaussian displacement distribution (solid line), normalised by the standard deviation of the sample to facilitate comparisons between different samples and shown on a semilogarithmic scale, with exponential and power-law tails.

Adsorption dynamics are similarly believed to be affected by kinetic barriers, and non-equilibrium dynamics are thought to be common. Unexpectedly

slow relaxation to the equilibrium contact angle was observed after micron-sized particles breached an oil-water interface [56]. The authors proposed a model in which the contact line undergoes thermally activated hops towards the equilibrium state, with pinning on microscopic surface heterogeneities between the hops [56, 57] (see Fig. 1.6a). Recently, systems were observed in which particles adsorb reversibly to the interface without breaching it [49] (see Fig. 1.8). Breaching and binding of particles to the interface was found to vary qualitatively with the salt concentration (see Fig. 1.8a): From low to high salt concentrations, particles i) experienced a repulsive interaction with the interface, ii) bound to the interface but did not breach it, iii) breached without binding first and iv) bound and subsequently breached. The authors propose an electrostatic model specific to liquid-liquid interfaces that explains the local energy minimum close to the interface, indicating that complex electrostatic interactions govern the dynamics perpendicular to the interface. In nanoparticles, where the potential well at the interface is not as deep, in-plane diffusion [44] provided evidence for rapid transitions between different immersion states.

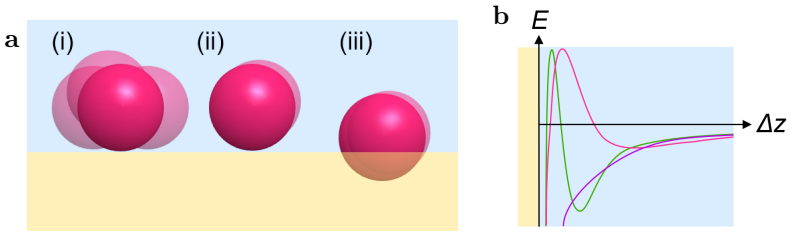


Figure 1.8: Probing the potential energy landscape at the interface. Interface-normal dynamics are governed by complex interactions between particles and interfaces, as well as between particles. Ref. [49] found a) three different behaviours in different experimental conditions: i) non-binding, ii) binding but not breaching, iii) breaching. b) Schematic potentials corresponding to the three cases in a) (i) pink, ii) green, iii) purple) as a function of separation of the particle from the interface, where $\Delta z = 0$ corresponds to the point of the particle that is closest to the interface being at the height of the interface.

1.2.3 Inter-particle interactions

Interfaces can both modify interactions between particles that are present in bulk liquids as well as give rise to interactions that are specific to interfaces [58] (see Fig. 1.9). There is a strong interest in the dynamics associated with these interactions as they govern self-assembly processes and can be used to test hypotheses in statistical physics and other fields.

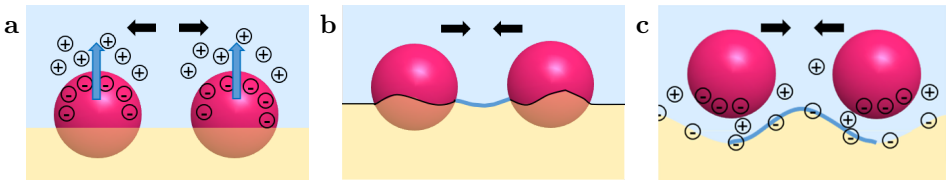


Figure 1.9: Inter-particle forces. a) Dipole-dipole interaction as an example of forces arising from an interaction with the interface. b) Interface-mediated (capillary) forces: Contact line deformations caused by non-spherical particle shapes, pinned interfaces or interface curvatures (for example in droplets) leads to typically attractive forces between particles. c) Electrostatic interactions with the interface can lead to capillary interactions by deforming the interface.

As an example of interactions that are modified by the presence of the interface, different liquids can favour different charges on particle surfaces [9], creating dipoles that repel each other (Fig. 1.9a). Anisotropic particle shapes as well as electrostatic interactions can deform the interface, giving rise to attractive capillary interactions (Fig. 1.9b): Deformations in the interface lead to lateral forces as minimisation of the interface area is energetically favoured [59]. This can result in counterintuitive observations such as attraction between like-charged particles [60]. There is a complex interplay between different forces (Fig. 1.9c), and interactions between particles at the interface and other particles as well as the interface itself are a subject of ongoing investigation [59, 49, 61]. For example, it was recently found that inter-particle interactions change qualitatively when particles

breach the interface as opposed to binding to it without breaching [49]. Interactions between nano-sized particles are expected to be weaker than for micron-sized particles, and more sensitive to thermal fluctuations, but are still poorly understood [61, 62].

In this work, we ensure low particle concentrations to avoid these effects, as they would make the analysis of single-particle dynamics too complex for the scope of our study.

1.2.4 Surfactants

The addition of a surfactant is expected to affect the particle dynamics significantly, and is currently not well understood despite being common in technological applications [1]: Effects on interfacial rheology [63, 39], alteration of the particle in terms of hydrodynamic radius and wetting properties through attachment of surfactant molecules, and lowering of the interfacial tension term of the adsorption energy (see Eqn. (2)) through competition with the particle for space at the interface are all expected to affect the dynamics of the system.

For the adsorption of a particle to an interface that is completely covered

with surfactant molecules (see Fig. 1.10), this leads to an altered adsorption energy of

$$\Delta E = -\pi R^2 \gamma_{\mathrm{SF}} (1 + \cos\theta)^2 + \gamma_{\mathrm{SF},2} A_{\mathrm{SF},2} \tag{5}$$

where γ_{SF} and $\gamma_{\mathrm{SF},2}$ are the interfacial tension of the surfactant-laden oil-water interface and the surfactant-water interface, respectively, and $A_{\mathrm{SF},2}$ is the area formed between the surfactant molecules and the phase into which they are released.

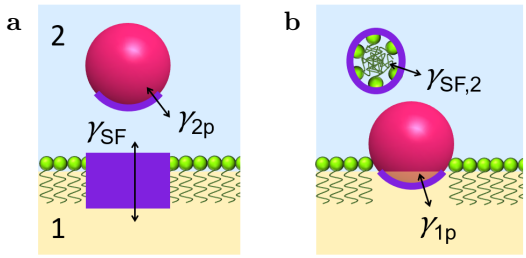


Figure 1.10: Schematic of a particle adsorbing to a surfactant-laden interface, with disappearing or forming interfacial areas highlighted in purple. a) Before adsorption, b) after adsorption, with displaced surfactant molecules dispersing (not shown) or forming (part of) a micelle.

Eqn. (5) yields an estimated maximal adsorption energy (90° contact angle) of 10 $k_{\mathrm{B}}T$ for an 80 nm particle at an interface with DDM added as a surfactant (see section 2.2.3). This assumes an interfacial tension value

γ_{SF} of 0.01 mNm^{-1} for 0.2 mM DDM solution as approximated using a linear regression to the values in Ref. [64], and neglecting the second term. The corresponding value for a 20 nm particle is $\lesssim 1\ k_B T$.

The equilibrium contact angle is expected to be farther away from 90° with a surfactant, as $\gamma_{SF} < \gamma_{12}$ must be fulfilled for the surfactant molecules to cover the interface. For a particle initially immersed in the phase favoured by its wetting properties, the magnitude of the first, dominant term in Eqn. (5) is therefore smaller than in Eqn. (2). The second term is positive, if likely small compared to the first. In reality it is difficult to establish the area $A_{SF,2}$, as the surfactant molecules may form micelles or disperse, but it is likely to scale linearly with the interfacial area removed by the particle, i.e. roughly with R^2.

A third, entropic term [65] may be relevant for large particles that displace many surfactant molecules from the interface. Each adsorption of a particle to the interface contributes a negative change in entropy (and therefore a positive change in energy). This is likely to be negligible for a single hard particle, but possibly significant for many small molecules or a soft micelle-like structure released from a surfactant-laden interface in the course of the adsorption of a particle. The net entropy gain would make

an adsorption more favourable for large particles, which is in keeping with observations of larger particles displacing smaller ones [22], although in this reference, the authors ascribe the displacement of smaller particles to the irreversible/reversible adsorption of the larger/smaller particles.

Interactions in a system with particles and surfactants at interfaces (see Fig. 1.11) include adsorption of surfactants to the particles (Figs. 1.11a and 1.11b), resulting in a particle wettability that depends on the surfactant concentration [66], and was found to affect the number of adsorptions in studies with high particle densities. Where particles and surfactants are soluble in the same phase, competition for space at the interface is observed [67] (Fig. 1.11c). By dissolving particles and surfactants in different phases, surfactants have also been shown to stabilise Pickering emulsions [68] (Fig. 1.11d). Given that gold particles adsorb to bare oil-water interfaces, in this work, we expect the former mechanism to be more likely to affect the interfacial stabilisation.

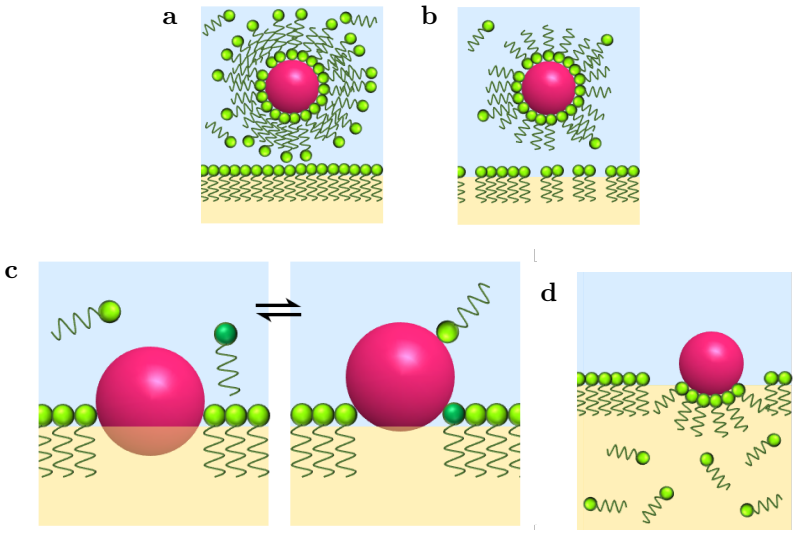


Figure 1.11: Scenarios of different interactions following the addition of surfactants to the particle-interface system. Surfactant molecules are depicted with a light green hydrophilic head and a dark green hydrophobic tail. a)-b) Surfactant-particle intractions can alter the wettability of the particle, making it a) hydrophobic or b) hydrophilic. c) Competition with the particle for space at the interface can lead to much easier desorption compared to the surfactant-free case: Here, the dark green surfactant molecule partially replaces the particle. d) Co-operative binding, where particles are in one phase and surfactants in the other.

1.2.5 Expected time scales for nanoparticle dynamics

The time scales of particle and interfacial dynamics have a wide range, and the faster ones are very difficult to capture. A wide range of different sampling rates is necessary to observe the dynamics that are relevant to out-of-plane motion, diffusion, inter-particle interactions, and interactions

with the surrounding liquids as well as with the interface. The time scales of the dynamics we aim to probe — diffusion within the interfacial plane, and perpendicular to it — are summarised in Fig. 1.12, with estimates of their values.

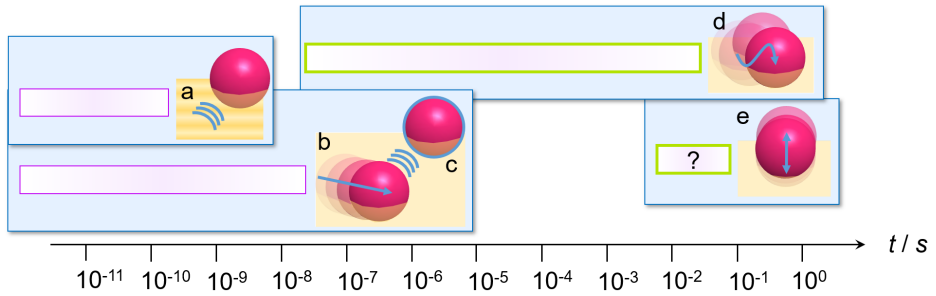


Figure 1.12: Approximate time scales associated with the dynamics of particles with diameters ranging from 1 to 100 nm, with processes highlighted in blue. The time scales of the dynamics that will be investigated in this work are outlined in green. a) Time scale of fluid density fluctuations τ_s. b) Transition between the ballistic regime and non-ballistic particle motion τ_p. c) Time scale τ_h on which hydrodynamic interactions between particles take place. d) Diffusive time scale τ_d, corresponding to a displacement of the particle by its radius. e) Time scale τ_v of out-of-plane motion. See text for more information.

At a very short time scale τ_s (see Fig. 1.12; currently far from experimentally accessible), liquids are expected to be compressible and a description of the system dynamics would include the motions of the particle and the interactions between it and the surrounding liquid molecules as a moving particle generates density flutuations in the liquid. The characteristic time

for this is $\tau_{\mathrm{s}} = R/c_{\mathrm{s}}$, where R is the particle radius and c_{s} is the speed of sound in the fluid.

At longer time scales τ_{p}, the dynamics of the liquid are averaged out. The particle can be described as inertial, i.e. it retains its momentum until a sufficient number of collisions with liquid molecules changes it. This regime is difficult to probe experimentally, but it has recently been achieved in liquids [69]. At much longer time scales, this description breaks down, and particle dynamics are treated in a probabilistic model. The transition between the two regimes occurs around the so-called momentum relaxation time τ_p. In the simplest model for damping, a Stokes force of $F_{\mathrm{S}} = -\gamma v$ is assumed, where v is the particle velocity and γ is the Stokes drag coefficient, yielding $\tau_p = m/\gamma = m/(6\pi\eta R)$, where m is the particle mass and η is the dynamic viscosity of the fluid [70].

The motion of particles affect the motion of other particles via hydrodynamic interactions, which decay inversely with the inter-particle separation, on a time scale of $\tau_{\mathrm{h}} = R^2\rho_{\mathrm{f}}/\eta$, where ρ_{f} is the fluid density and η the dynamic fluid viscosity. τ_{h} is the time it takes for the particle-induced fluid motion to travel a distance of R. τ_{h} is related to τ_p via $\tau_{\mathrm{h}}/\tau_p = 9\rho_{\mathrm{f}}/2\rho_{\mathrm{p}}$, where ρ_{p} is the particle density, and is therefore usually of a similar order of magnitude

[69].

Finally, the characteristic time scale for diffusive motion is given by Einstein's diffusion equation $\langle \Delta x^2 \rangle = 4Dt$ (see also section 3.1), where Δx is the particle displacement in the time interval t, the brackets denote an ensemble average, and D is the diffusion coefficient. For particles with diameters of 10 and 100 nm, using diffusion coefficients calculated from Eqn. (4) with a hydrodynamic diameter of twice the particle diameter, this yields times τ_{d} of 25 μs and 25 ms, respectively, for a displacement by the particle diameter.

Out-of-plane dynamics have experimentally been found to have a breaching step that is faster than the experimental time resolution of 20-40 Hz [56, 44] and recently 5 kHz [49], followed by a long relaxation time τ_{v} towards equilibrium immersion depth. τ_{v} is expected to be longer than typical experimental time scales; on the order of months in microparticles [56]. Nanoparticles are more susceptible to thermal fluctuations because of their smaller size, and therefore likely to transition between different immersion states on a faster time scale.

1.3 Scope of this thesis

To the best of our knowledge, the out-of-plane dynamics of nanoparticles have not been characterised in detail. The high time resolution (μs) required to resolve out-of-plane dynamics and their effects on the in-plane motion is experimentally difficult to achieve for particles as small as this in combination with the high spatial precision required to resolve the thermal motion of a particle as large as this. In this work, we will characterise the diffusion of nanoparticles at interfaces at much higher spatiotemporal resolution (1 nm localisation precision at a time step of 20 μs) than has previously been possible, resolving out-of-plane motion to measure its time scales and better understand the interplay between it and the in-plane dynamics. The effects of particle size variation and addition of a surfactant are investigated.

Chapter 2 presents the experimental methods, discussing the custom-built total-internal-reflection dark-field microscope used and the interface sample preparation protocol developed in this work. Chapter 3 introduces experimental observables characterising diffusive behaviour, and describes the particle tracking algorithm used to obtain this information from the raw image data. Chapter 4 presents the results obtained about the ensemble-averaged

diffusive behaviour of particles adsorbed to the interface, contrasting different particle sizes and interface types. Chapter 5 discusses out-of-plane dynamics, presenting time-resolved adsorption events and how they vary between the different sample types, as well as qualitatively new behaviours. Chapter 6 gives a brief summary of the methods, findings and implications, and suggestions for future measurements.

2 Experimental

I carried out the sample protocol development presented in section 2.2 and built the microscope described in section 2.3. Adar Sonn-Segev built a similar setup on which I acquired the data presented in Fig. 5.4, and Xuanhui Meng built the first setup of this kind in the group with the help of Daniel Cole and Gavin Young. I performed the analysis.

The most reliable way to study the dynamics of nanoparticles at interfaces is to observe them directly. A relatively non-invasive way to achieve this is to probe with electromagnetic radiation in the visible spectrum, i.e. with an optical microscope. The selection of a particle-tracking method is discussed in section 2.1. The interface preparation protocol and its development are described in section 2.2. The microscope and its components are described in section 2.3.

2.1 Selecting a particle-tracking method

Typical methods for single-particle tracking include TIRF microscopy [71], which yields high signal-to-noise ratios by suppressing background signals

resulting from scattering, allowing small particles to be tracked accurately. However, fluorescence methods [72] are limited in localisation precision and time resolution by bleaching and photoblinking. In addition, single quantum emitters have a limited photon emission rate due to the finite lifetime of the excited state. Assuming a 1 MHz excitation rate and photon losses typical for state-of-the-art optics, a rough rule of single emitter localisation and speed is given by [73] $\sigma(\text{time, space}) = 1$ nm $\text{Hz}^{-1/2}$. This means that at 100 kHz, the localisation precision is 300 nm, with only about 1 photon detected per image. 300 nm is considerably larger than the expected displacement of a nanoparticle in water at room temperature: To estimate how much a particle will be displaced in this time interval at an interface, we use Einstein's relation $\langle(\Delta x)^2\rangle = 4Dt$, where Δx is the displacement of the particle over the course of the time interval t and D is the diffusion coefficient. The angular brackets denote an ensemble average. Using Eqn. (4), assuming that both phases have a dynamic viscosity of 10^{-3} Pa·s, similar to that of water ($0.89{\cdot}10^{-4}$ Pa·s), a spherical particle with a hydrodynamic diameter of 50 nm would be expected to exhibit a diffusion coefficient of about 8.6 $\mu\text{m}^2\text{s}^{-1}$, which corresponds to a displacement of $\Delta x = \sqrt{4Dt} = 18$ nm in 10 μs. This means that the detailed dynamics of particles of this size cannot be resolved at high speeds using current fluorescence microscopy methods,

even if multiple emitters are used.

A different approach is needed to access faster timescales. Rather than suppressing the background by using fluorescence and detecting a wavelength other than the excitation wavelength, we decided to collect scattered light, which in suitable geometries is limited by photon input rather than the fluorescence process. For a plane wave incident on a spherical particle, Mie theory gives an exact expression [73] for the scattering amplitude as a function of the wavelength of the light, under the assumption that the particle is spherical:

$$s(\lambda) = \alpha(\lambda) = \eta\epsilon_{\mathrm{m}}(\lambda)\pi\frac{d^3}{2}\frac{\epsilon_{\mathrm{p}}(\lambda) - \epsilon_{\mathrm{m}}(\lambda)}{\epsilon_{\mathrm{p}}(\lambda) + 2\epsilon_{\mathrm{m}}(\lambda)}, \tag{6}$$

where α is the polarisability of the particle, ϵ_{m} and ϵ_{p} are the complex permittivities of the medium and particle, respectively and d is the particle diameter. The scattered light can be collected and focused onto a camera to obtain an image (see Fig. 2.1).

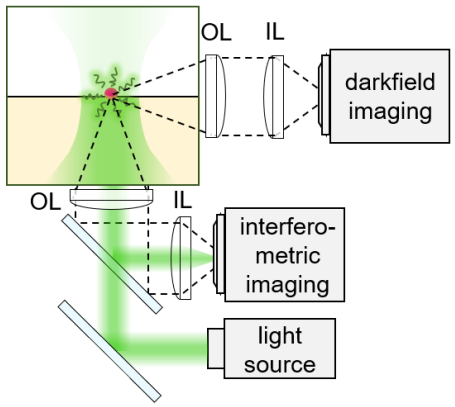


Figure 2.1: Imaging the scattering signal of a particle at a reflecting interface using the purely scattered and interferometric signals (see text). The illumination path is drawn in green and the path of the scattered light in dashed black lines. Objective lenses are marked with OL, imaging lenses with IL.

The two different geometries shown here — interferometric scattering and dark-field microscopy — are contrasted in section 2.1.1. Dark-field microscopy is found to be more suited to our experiments, and adjustments to conventional dark-field microscopy are discussed in section 2.1.2.

2.1.1 Interferometric scattering vs. dark-field microscopy

In both the interferometric and the dark-field imaging methods (shown in Fig. 2.1), the scattering signal is collected along with a background term arising from spurious reflections in the sample and the optical path and

ambient light. In the interferometric geometry, the background term additionally contains the reflected illumination beam. The detected signal is given by

$$I_{\mathrm{det}} = |E_{\mathrm{b}} + E_{\mathrm{s}}|^2 = |E_{\mathrm{i}}|^2 \left(b^2 - b\,|s| \sin(\phi) + |s|^2\right) \tag{7}$$

where b is the background signal amplitude and ϕ is the scattering phase. The pure scattering component, $|E_{\mathrm{i}}|^2 |s|^2$, scales with d^6. This means that if the size of the particle is halved, the signal drops by a factor of 64. The mixed term scales with d^3 (making the scattering term negligible for small particles), and over the last fifteen years, microscopy methods using this signal have been developed and applied with great success. Interferometric scattering microscopy (iSCAT) is a powerful and experimentally simple method of tracking small scatterers [74], with 2 nm localisation precision achieved at 2 μs temporal resolution for 20 nm gold particles [75]. However, state-of-the-art iSCAT has not achieved wide-field illumination at imaging rates of several tens of kHz or higher [74]. Besides, iSCAT is highly sensitive to fluctuations in sample backgrounds and the optical path.

Meanwhile, experimental advances in dark-field microscopy [76, 77], in which

the pure scattering term is used, have also led to combinations of high localisation precision and temporal resolution, hinting at the possibility of achieving the same spatiotemporal resolution with less sensitivity to background noise, which becomes important as the scattering intensity decreases with particle size and illumination. Because of the limited speed of iSCAT in wide-field applications and its higher sensitivity to background noise compared to dark-field geometries that suppress background noise [76], we use dark-field microscopy in this work.

Using Eqn. (7), the intensity detected in a dark-field geometry for a strongly scattering particle and efficient background rejection, i.e. if $b \ll s$, can be approximately divided into a signal and a background term:

$$\begin{aligned} I_{\mathrm{DF}} &= |E_{\mathrm{b}} + E_{\mathrm{s}}|^2 = |E_{\mathrm{i}}|^2 \left(b^2 - b\,|s| \sin(\phi) + |s|^2\right) \\ &\approx |E_{\mathrm{i}}|^2 \, |s|^2 + I_{\mathrm{b}}. \end{aligned} \tag{8}$$

2.1.2 High-performance dark-field microscopy

To maximise performance in terms of the combination of localisation and speed using small scatterers, the scattered signal must be maximised and the background signal minimised. An important step in maximising the scattered signal has been the use of high-NA objectives, yielding a high collection efficiency [77] (the collection angle defined by the objective lens in Fig. 2.1). In addition, it is useful to select a strong scatterer. Gold nanoparticles are well suited to many imaging applications owing to their optical properties as well as biocompatibility and relatively easy synthesis [78]. They exhibit a strong surface plasmon resonance in the visible spectrum: At the resonance, the term $\epsilon_{\mathrm{p}}(\lambda) + 2\epsilon_{\mathrm{m}}(\lambda)$ in Eqn. (6) approaches zero, which strongly enhances their polarisability. This circumvents the limitations of fluorescence microscopy, enabling wide-field imaging at high speeds. For this reason, we use gold nanoparticles, and the main laser wavelength used, 520 nm, is close to the surface plasmon resonance maximum, which is between 520 and 550 nm in water for particles with diameters between 20 and 80 nm.

Minimising the background signal arising within the sample is achieved by changing the geometry of the illumination and detection. When illuminating

the sample with a beam normal to the interface, any particles above and below the interface contribute a background signal, even if they are not in focus (see Fig. 2.2b). An elegant way to minimise contributions from parts of the sample other than the interface and thereby achieve an extremely low background signal is by making use of total internal reflection (TIR) [76], the phenomenon of light being reflected at interfaces between phases with different refractive indices if the angle between the propagation direction of the light and the interface is sufficiently shallow.

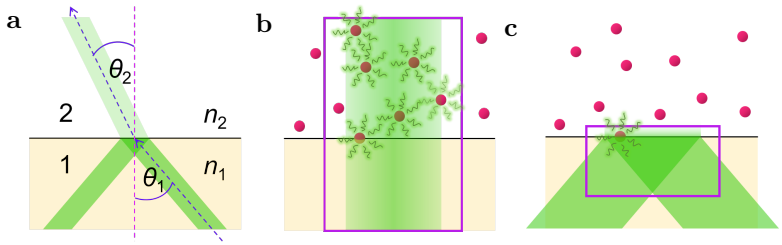


Figure 2.2: Beam paths at an interface. a) Total internal reflection (TIR) vs. refraction of a beam of light at an interface between phases 1 and 2. If θ_1 is sufficiently large (see Eqn. (10)), the incoming beam is reflected with the same angle by the interface. b) Epi-illumination, commonly used in other imaging geometries: The incident light is tramsmitted through the phase boundary, and objects both above and below the interface as well as at the interface are illuminated. c) TIR illumination: The incident light is reflected at the phase boundary. Above the boundary, the intensity of the electromagnetic field decays exponentially, creating an evanescent field (see Eqn. (11)). Only objects at or near the interface are imaged.

At small incidence angles θ_1, the incoming beam is refracted with angle θ_2 (see Fig. 2.2), given by the refractive indices n_1 and n_2 of the two phases in

what is known as Snell's law

$$n_1 \sin(\theta_1) = n_2 \sin(\theta_2). \tag{9}$$

The largest incident angle at which refraction occurs is obtained when $\theta_2 = \pi/2$, resulting in the critical angle that is just large enough for refraction to take place,

$$\theta_c = \arcsin\left(\frac{n_2}{n_1}\right). \tag{10}$$

For larger angles, total internal reflection occurs and only the interface and a small volume above and below are illuminated. The intensity of the evanescent field is typically assumed to decay exponentially [79], with the penetration depth, the distance within the sample from the reflecting interface at which the intensity decays to 1/e of its value at the interface $|E_i|^2$, given by [79]

$$d = \frac{\lambda_0}{4\pi n_1} \frac{1}{\sqrt{\sin^2(\theta_1) - \sin^2(\theta_c)}}, \tag{11}$$

where λ_0 is the vacuum wavelength of the incident light. For a critical angle of 63°, the relevant value for this work, incident angles of 65 and 70° lead to penetration depths of 155 and 90 nm, respectively. This means that the signal in TIR-DF arises almost exclusively from scattering caused by refractive index mismatches in this limited volume, whereas in epi-illumination (see Fig. 2.2b), the signal includes background contributions from above and below the interface. I_b in Eqn. (8) is limited to spurious reflections from components of the microscope and any contaminants such as dust, light from the surroundings and small contributions from poorly illuminated, out-of-focus particles above and possibly below the interface, as well as noise from the camera.

Making use of the surface plasmon resonance in gold and minimising the background via an optimised experimental geometry result in a high signal-to-noise ratio. TIR-DF is highly suited to this experiment, with a localisation precision of 1 nm achieved at a shutter speed of 40 μs for particles with a diameter of 40 nm at a power density of 20 $\mu\mathrm{W}\mu\mathrm{m}^{-2}$, and 3 nm achieved at the same speed and a power density of 30 $\mu\mathrm{W}\mu\mathrm{m}^{-2}$ with 20 nm particles. Power densities of up to 250 $\mu\mathrm{W}\mu\mathrm{m}^{-2}$ were used to image particles at interfaces.

2.2 Preparation of liquid-liquid interfaces

To decide how to attempt to prepare the interface, several measures of success can be identified.

The interface must be stable for a sufficiently long time period to allow observation, and possibly equilibration, as one would expect there to be flows immediately after the interface is established. To visualise the interface with a TIR-DF (or iSCAT) microscope, the interface must be brought within the working distance of the objective, which is typically less than 300 μm for oil-immersion objectives. The spatial extent of the lower phase perpendicular to the interface must be smaller than this. The refractive index of the lower phase must be matched to that of the coverslip to enable TIR illumination.

Background scattering must be minimal. Contaminants are undesirable both in terms of making the experiment more difficult due to their scattering, and in that contaminants could have a wide range of effects [80] on the experiment that would alter the results in unpredictable and adverse ways: Not only could they interact directly with the particle of interest through electrostatic forces, but also indirectly, mediated by the interface (see e.g. Ref. [61] for a brief overview). These indirect interactions include

typically attractive forces generated by the deformation of the interface by particles, and electrostatic forces between particles arise from or are altered by the interface. There is a complex interplay between these forces; electrostatic forces can cause deformations of the interface [40], and the shape of the interface can affect electrostatic interactions.

The interfacial tension between the liquids must be such that the adsorbed state is favoured thermodynamically for it to be possible to observe particles diffusing at the interface, which must be considered when choosing the liquids (see equation (2)). Planarity is desired to avoid effects characteristic to the curvature of the interface [59], which would be hard to characterise experimentally because the exact curvature would be difficult to reproduce. Small isotropic curvatures, however, are likely to be negligible. A study [47] found that curvatures of droplets where the radius of curvature was at least an order of magnitude larger than the radius of curvature of the particle had no effect on the diffusion coefficient of particles at the interface between the droplets and the surrounding fluid. Both phases having a low viscosity makes it possible to observe particle motion in the underdamped regime. Finally, it is desirable for particles to not be too strongly bound (see section 1.2.1) to allow the observation of dynamics perpendicular to the interface.

The remainder of this chapter is divided into the process of finding a suitable protocol in section 2.2.1 and the final protocol in section 2.2.2, with more details in the materials section, 2.2.3.

2.2.1 Development of a suitable protocol

An initial idea that fulfilled the basic requirements was taken from Refs. [81] and [82], and is shown in Fig. 2.3. In Ref. [81], several small (205 μm$\times$205 μm) interfaces were prepared to study the dynamics of protein aggregation at an interface between silicone oil and water. The upper phase was added to the oil-filled grid. In Ref. [82], the same type of TEM grid is used to study phospholipid diffusion at interfaces between water and silicone oil with different visosities. The authors, citing their previous work in Ref. [83], describe placing the TEM grid onto the oil droplet with tweezers, followed by the addition of the phospholipid and finally the upper phase. The illuminating laser beam is directed at the interface at a shallow angle with the interfacial plane so that it is reflected back into the objective rather than refracted into the upper phase. The light scattered by the particles is collected by a high-numerical aperture objective from below.

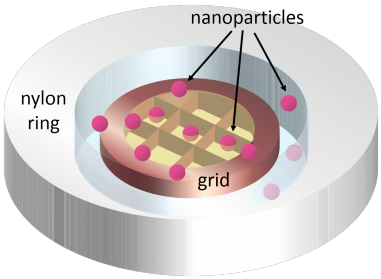


Figure 2.3: Initial idea for making a liquid-liquid interface, based on Ref. [81]; not drawn to scale. A TEM grid with a height of about 20 μm is placed on a coverslip to contain the lower phase (in yellow) in 200 μm square wells; the upper phase (pale blue) is bordered by a wider nylon ring.

In this type of interface preparation protocol, the border of the interface is held in place by a solid edge for stability. A TEM grid is placed on a microscope coverslip, the lower phase is placed inside, a containment ring is placed around this and the upper phase, containing the particles, is added from above. This was considered a promising approach because of the microscopic nature and high degree of planarity of the resulting interfaces, and the wide previous application of similar protocols. [81, 84, 82] Using this type of grid would also allow the resulting interface to be lowered close enough to the objective to be imaged, while at the same time, the effects of the coverslip and the water-air interface above the sample were not expected to have a significant effect on the dynamics of the particles. [85] For our ex-

periments, we required larger interfaces than the ones in Refs. [81], [84] and [82] to minimise contributions from wall effects, which led to the choice of aperture grids that would yield an interface with an area of at least 3 mm^2, which is thought to make the effect of the grid on the dynamics negligible (see e.g. Ref. [86]). Water was chosen as an upper phase and silicone-based microscope immersion oil as a lower phase. The refractive index of immersion oil matches that of glass to enable TIR-DF imaging and operation. Microscope immersion oil is index-matched with glass, and available in various viscosities. Its hydrophobic nature makes it suitably immiscible with water and favours the adsorption of particles (see Eqn. (2)).

Within this general approach, the parameters that were adjusted to find a suitable protocol were the exact geometry in terms of the structure and dimensions of the grid, the diameter of the aperture in the container, the methods and timings of transferring substances and the functionalisation of the surface of the coverslip.

2.2.1.1 Producing a planar oil-air interface contained by a grid

The first step towards a viable interface of this geometry was producing a stable, planar oil-air interface within a container. As this had previously

been achieved using TEM grids, we followed the same approach, the aims being to i) establish a method of determining whether we had produced a suitable oil-air interface and ii) choose the more suitable addition order of the grid and the oil. In Ref. [82], grids were placed onto oil that had been added to the coverslip, whereas in Ref. [84], the grid was added before the liquid.

The first attempts were made using TEM grids with an outer diameter of 3.05 mm, a height of about 23 μm and hole and bar widths of 205 and 45 μm, respectively, filled with either glycerol or a high-viscosity immersion oil. Liquids with different viscosities produced different results. When a liquid-air interface in a grid was left to stand for a few minutes, the liquid would wet the coverslip around the edges of the grid, indicating that it was seeping underneath the grid. This added to the difficulty in controlling the height of the interface within the grid, and thereby the resulting shape and its stability over time. It was also undesirable because it could provide an additional pathway for contaminants originating from the container for the upper phase if it came into contact with the container. The spreading process was fastest with the low-viscosity oil, making it easier to use high-viscosity oil for the initial trials.

To assess the quality of the oil-air interface, we tested several observation methods, including i) using a stereomicroscope with the interface plane perpendicular to it, ii) using a stereomicroscope with the interface plane tilted using a wedge, iii) using a stereomicroscope and a mirror to visualise the interface at an angle (see Fig. 2.4 for this and method iv)), iv) examining a magnified side view of the sample using a lens or magnifying glass, and v) visual inspection at an angle such that the interface reflected light from the ceiling into the eye of the experimenter (see Fig. 2.5).

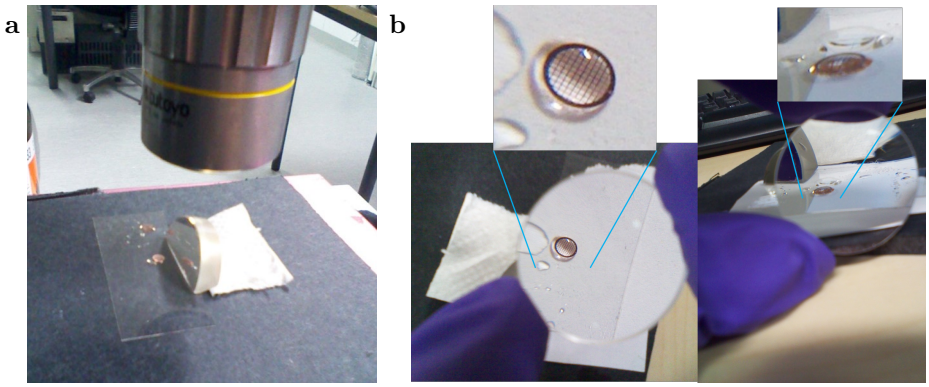


Figure 2.4: Visualising a liquid-air interface contained by a TEM grid. a) At an angle using a stereomicroscope. A mirror is used to view the sample from the side. b) Using a lens to magnify the lower phase and its container.

The three approaches using the stereomicroscope proved unsuitable because the stereomicroscope lacked the required depth of field; only about half a grid spacing was in focus, depending on the viewing angle. Additionally,

and more importantly, the liquid line was not visible. The magnifying glass made the sample slightly easier to see than with the naked eye, and it was possible to determine whether the liquid-air interface was approximately flat. This proved easier to do with aperture grids than with TEM grids, and it was at this stage that we switched to aperture grids with an inner diameter of 1.5 mm. However, the use of the magnifying glass lengthened the time between the addition of the lower and upper phases, which appeared to be disadvantageous during the addition of the water phase, resulting in a higher collapse rate of the interface. For this reason, simple visual inspection at an angle became the preferred method.

Having found a way to determine the state of the oil-air interface, it was found that the shape of this interface was easier to control when adding the oil after placing the grid, especially with the aperture grids. This also reduced the chances of spills of oil around the grid. In addition, we found that using tweezers to handle the grid as in Ref. [82] easily bent the grids, so to prevent this and avoid contamination, we gently dropped them from their container onto the microscope coverslip instead.

2.2.1.2 Producing a stable oil-water interface

The second step was to add water to this sample in a way that would not immediately lead to a collapse of the resulting oil-water interface.

With the aperture grid, the one factor that was found to be critical to producing a stable interface was the shape of the interface between the oil and the air before the addition of the upper phase. Flat oil-air interfaces resulted in slightly underfilled, usually unstable oil-water interfaces. In addition, underfilled oil-water interfaces were often so close to the microscope coverslip that any contaminants at the glass-oil interface contributed a large scattering signal. Slightly overfilled aperture grids were most likely to result in a stable, approximately planar oil-water interface. A series of oil-air interfaces is shown in Fig. 2.5.

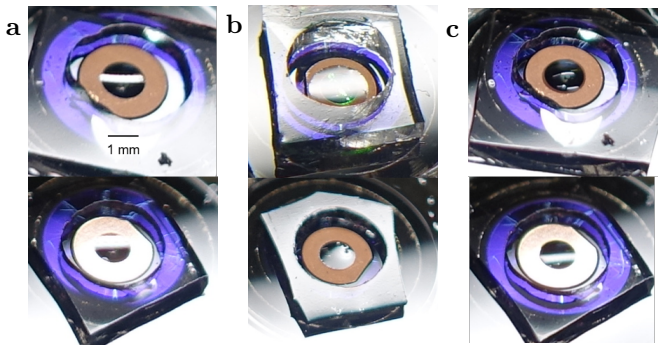


Figure 2.5: Photographs of interface sample during preparation; at the step before the water is added. a) Underfilled, b) planar oil surface, c) overfilled. The reflection of objects can be used to determine whether the oil-air interface is planar and, if not, whether it is under- or overfilled. In b), where the interface is planar, the light is reflected by the entire interface (upper image), unless only a part of the interface is planar, for example if one side of the interface is pinched by the aperture grid (lower image). In a) and c), the image of the light source is made to appear smaller by a lensing effect, which, in addition, makes the ends of the rectangular ceiling light appear to turn slightly downwards when the interface is underfilled (a) and slightly upwards when the interface is overfilled (c).

The time between the addition of the oil and the addition of the water was kept to a minimum to avoid allowing the oil to spread beneath the grid. Not all apparently suitable oil-air interfaces resulted in stable oil-water interfaces. Typically, unstable interfaces could be identified within about 15 minutes by observing the distance of the interface to the objective: A decreasing oil level after a brief equilibration period indicates a pathway for the oil to escape the grid, which typically did not stabilise over time.

Another parameter was the outer container. It was possible to produce an

interface with a droplet (approximately 6 μL) of water on a TEM or aperture grid without a container, however, these interfaces were not very long-lived, likely due to evaporation. Adding an outer container extended the lifetime of interfaces to sometimes more than ten hours. The inner diameter of this container had to be large enough to not disturb the interface, and was typically chosen to be larger than the outer diameter of the grid, but small enough so that the weight of the water would not be distributed too anisotropically over the oil – very large container diameters (larger than about 4.5 mm) typically did not result in observable oil-water interfaces.

Coverglass treatments tested were a simple rinsing and sonication protocol described in section 2.2.3, plasma-etching, which makes the surface more hydrophilic by thoroughly removing organic residues and exposing the hydroxy groups of the glass, and application of a commercial car windshield rain repellant, Rain-X, to make the surface hydrophobic. This was found to affect the surface tension between the glass and the oil and between the glass and the water. A glass-oil interaction that was too favourable resulted in the oil spreading beneath the grid; in cases where it was too unfavourable and the glass-water interaction too favourable, it is thought that this increased the risk of the water breaking through the oil as the droplet was being placed. The final coverglass treatment was a simple washing protocol

described in section 2.2.3.

2.2.1.3 Planarity

With a basic protocol for a stable oil-water interface that could be expected to be planar established, we assessed the resulting interface in terms of planarity and absence of observable contaminants to refine the procedure.

The method of estimating the curvature is shown in Fig. 2.6. The laser beam that is reflected by the interface is used to determine at which distance between the sample stage and the objective the interface is in focus. The sample is moved with respect to the laser beam using two translation stages actuated with micrometers (see section 2.3), and the positions of the micrometers are noted at the highest point of the interface and at a laterally displaced point that is as far away from the highest point as possible but can still be imaged. The height difference and distance within the horizontal plane are used to estimate the curvature of the interface assuming that the interface has the shape of a section of a sphere (see figure caption). In flat interfaces, the radius of curvature is in excess of 25 cm ($a = 2$ μm, b=1 mm).

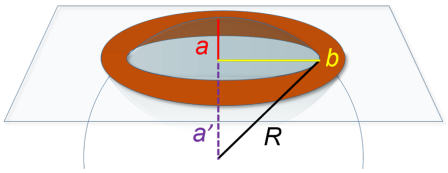


Figure 2.6: Assessing the curvature of an interface. Schematic interface section (blue, surrounded by a brown copper ring) as part of an imaginary sphere. The radius R, shown in black, is given by $R = a + a'$; $R^2 = a'^2 + b^2$. Inserting the first equation into the second one yields $R = (a^2 + b^2)/(2a)$. a and b can be measured using the translation stages of the microscope and the reflected beam (see section 2.3.1).

2.2.1.4 Contaminants

To ensure absence of contaminants, a sample with no added particles was prepared, i.e. pure Milli-Q water on oil. This showed that contamination was minimal when care was taken to not introduce unnecessary contamination during any step: The oil was centrifuged at a relative centrifugal force of at least 12300×g for 30 minutes to remove particles with a higher density than the oil, and coverslips were cleaned to minimise the number of contaminants travelling to the interface through the oil. The purification methods are described in detail in section 2.2.3. Images of the interface without added particles are shown in Fig. 2.7.

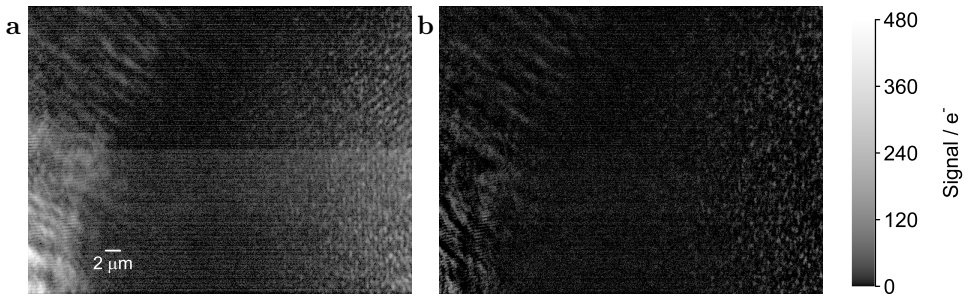


Figure 2.7: Checking for contaminants using a water-on-oil interfaces with no added particles. Particles appear bright against the dark background (see later figures). Beneath the interface, i.e. in the oil phase, many particles were found in a narrow layer close to the coverslip, but not near the interface. a) Raw image. b) After a background subtraction (see section 3.2.2), there are still no contaminants visible. The signal visible here is stationary and attributed to scattering in the optical paths. For the meaning of the units, see section 2.3.2.

2.2.2 Preparation of water-on-silicone oil interfaces

The interface used in the experiments for this thesis is shown schematically in Fig. 2.8.

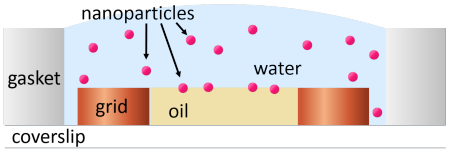


Figure 2.8: Schematic of the interface sample, not drawn to scale: A copper grid contains an oil phase and a silicone gasket contains a water phase that surrounds the copper grid. The four materials are supported from below by a microscope coverslip. Nanoparticles are initially in the water phase and adsorb to the oil-water interface. The outer and inner diameter of the copper grid are 3 and 1.5 mm, respectively, and the height is approximately 44 μm. The inner diameter of the gasket is approximately 3.5 to 4 mm and the height approximately 1 mm.

A copper aperture is placed on a coverslip. A fine pipette tip attached to the tip of a Pasteur pipette is used to transfer a small amount of centrifuged oil to the centre of the copper grid. A silicone gasket with a circular hole is placed over the copper ring, and finally, the water phase containing the nanoparticles is carefully added on top of the oil with a pipette (approximately 20 μL). It can either be added as a droplet or more gradually, but should be placed above the centre of the copper ring rather than on one side, otherwise the copper ring is more likely to move towards the other side.

We aim for a slightly overfilled grid, which results in a stable, flat or slightly overfilled oil-water interface. The interface is not, in fact, required to be pinned by the corner formed by the grid – often, interfaces where the oil

spilled onto the grid before the water is added turn out to be stable and flat. Fig. 2.9 shows two samples before the addition of the aqueous phase.

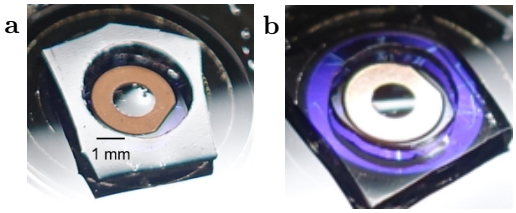


Figure 2.9: Photographs of interface samples just before the water phase is added. a) Flat oil surface, as is visible from the way light is reflected from it. The resulting oil-water interface is likely to be slightly underfilled and often unstable. b) Slightly overfilled. The rectangular shape of the overhead light is visible and slightly distorted. This kind of sample is likely to result in an approximately flat oil-water interface.

A cover is placed on the sample during data acquisition to minimise the background signal from ambient light as well as evaporation and the influence of air currents. Particles may start adsorbing to the interface within 20 minutes after adding the aqueous phase, especially for particles in DDM solution, but depending on the interface sample it may take more than an hour for the first particles to be observed. As a rule, smaller particles were observed to land sooner after the preparation of the interface, and sooner in DDM-oil interfaces than in Milli-Q-oil interfaces (see Fig. 7.1). This could be due to different kinetic barriers to adsorption: Small particles are likely to have smaller surface heterogeneities, and particles in DDM solution may have altered wetting properties. Alternatively, the difference could be due

to different diffusion properties in the water phase. Small particles are expected to diffuse faster (see Eqn. (4)), and the adsorption of DDM molecules to the particles could alter their hydrodynamic radius.

2.2.3 Materials

Glass coverslips (Menzel, 24x50 mm, thickness 1.5) are rinsed alternatingly with Milli-Q water and ethanol (Sigma-Aldrich, GC grade); five times in total, then sonicated for 15 minutes in a 1:1 mixture of Milli-Q water and isopropanol (Sigma-Aldrich, GC grade), and before use rinsed again with Milli-Q water and dried with a jet of nitrogen gas. If they were stored between sonication and use, they were left in the solution they were sonicated in for no longer than 12 hours.

Gold nanoparticles with PVP functionalisation were purchased from nanoComposix (gold nanospheres, PVP, NanoXact, 0.05 mg/mL) and diluted with motility buffer (see below for details), Milli-Q water or a DDM solution in ratios of typically 1:50 for 80 nm particles (lot number ECP1384), 1:200 for 40 nm particles (lot number ECP1036) and 1:1500 for 20 nm particles (lot number ECP1386). The different dilutions resulted in similar concentrations for 20 and 40 nm particles; the concentration of 80 nm par-

ticles was lower by a factor of 2.

Table 1: Specifications of stock solutions of PVP-functionalised gold nanoparticles (from nanoComposix): Diameter d (TEM), concentration c in particles per milliliter, hydrodynamic diameter d_{H}, zeta potential ζ.

Particle type	d / nm	c	d_{H} / nm	ζ / mV
20 nm Au	19.1±2.4	$7.4{\cdot}10^{11}$	44	-28
40 nm Au	40.8±4.5	$7.5{\cdot}10^{10}$	68.7	-31
80 nm Au	83±10	$9.0{\cdot}10^{9}$	105	-17

Solutions of particles at surfactant-free (MQ) interfaces are diluted in 18.2 MΩ cm Milli-Q water; solutions of particles intended **for observation on glass** are diluted with a buffer (MB) as particles in water do not attach to the glass surface. MB is prepared by mixing solutions of 80 mMMOPS, 20 mM$MgCl_2$ and 0.4 mMEGTA, where the MOPS and EGTA solutions are brought to pH 7.3 by adding HCl. MOPS (ultra high purity grade), $MgCl_2$ (anhydrous, high purity grade) and EGTA (ultra high purity grade) were purchased from Amresco. **Solutions of particles at surfactant-laden (ddm) interfaces** are prepared by adding n-dodecyl-β-D-maltoside (DDM): The stock solution is diluted with a 1 mg/mL solution of DDM in Milli-Q (typically 0.2 mM; the critical micelle concentration is 0.17 mM). Solutions of DDM must be replaced regularly; contaminants appear to accumulate in them within days or weeks. The DDM was purchased from Anatrace (sol-grade).

Immersion oil for the lower phase of interface samples was purchased from Cargille (refractive index 1.5230±0.005 at 589.3 nm and 25 °C, code 1160, lot number 012490). The density was 1.076 g cm^{-3}, the kinematic viscosity 41 cSt and the surface tension 35 dynes/cm; all at 25 °C. It was centrifuged at a relative centrifugal force of 17200×g for 30 minutes to remove contaminants. High-viscosity immersion oil used for developing the interface protocol was purchased from Olympus (IMMOIL-F30CC). The density was 0.9169 g cm^{-3} (at 15 °C); the kinematic viscosity was 1.73 cSt (at 40 °C).

Aperture grids made of copper were obtained from Gilder Grids (GA1500-C3, aperture width 1500 μm). The manufacturer states that the thickness of the grids increases with aperture size, varying between 25±3 μm for the 75 μm aperture and 50±5 μm for the 2000 μm aperture, leading to an estimate of 44±5 μm for the 1500 μm aperture. Previously, similar EMS 1500-CU grids have been used. TEM grids were also purchased from Gilder Grids (G100), with an outer diameter of 3.05 mm and hole and bar widths of 205 and 45 μm, respectively. The thickness of the grids varied with the mesh repeat as for the aperture grids, with an estimated thickness of 23±5 μm for the grids we used.

PDMS gaskets were prepared using the Sylgard 184 silicone elastomer kit.

The base and curing agent were mixed at a ratio of 10:1 and centrifuged at 2500 rpm for 15 minutes to remove air bubbles. The mixture was poured into a Petri dish and placed in an oven at 60°C for several hours. The desired height of the resulting sheets was approximately 1 mm. A custom-built hole puncher was used to remove cylindrical portions and a scalpel was used to cut around them, leaving pieces of silicone with a circular aperture. The finished gaskets were sonicated using the same mixture of solvents as the coverslips, then rinsed with Milli-Q water, dried with nitrogen and stored in a Petri dish with a lid until use.

2.3 Total-internal-reflection dark-field microscopy

For the work presented in this thesis, experiments were performed on a home-built TIR-DF microscope [76, 87] combined with a high-speed camera. The microscope is described in detail in section 2.3.1. A characterisation of the camera is given in section 2.3.2, the signal-to-noise ratio is characterised in section 2.3.3 and the spatial precision of the microscope is assessed in section 2.3.4.

2.3.1 Detailed description of the experimental setup

The TIR-DF microscope that we built to collect most of the data presented in this thesis is illustrated in Fig. 2.10. It is designed to allow the use of three different lasers as in Ref. [87]. The 445 nm laser was used to image silver nanoparticles, as their surface plasmon resonance is at a shorter wavelength than that of gold particles of a similar size. For the experiments presented in this thesis, the 520 nm laser was used.

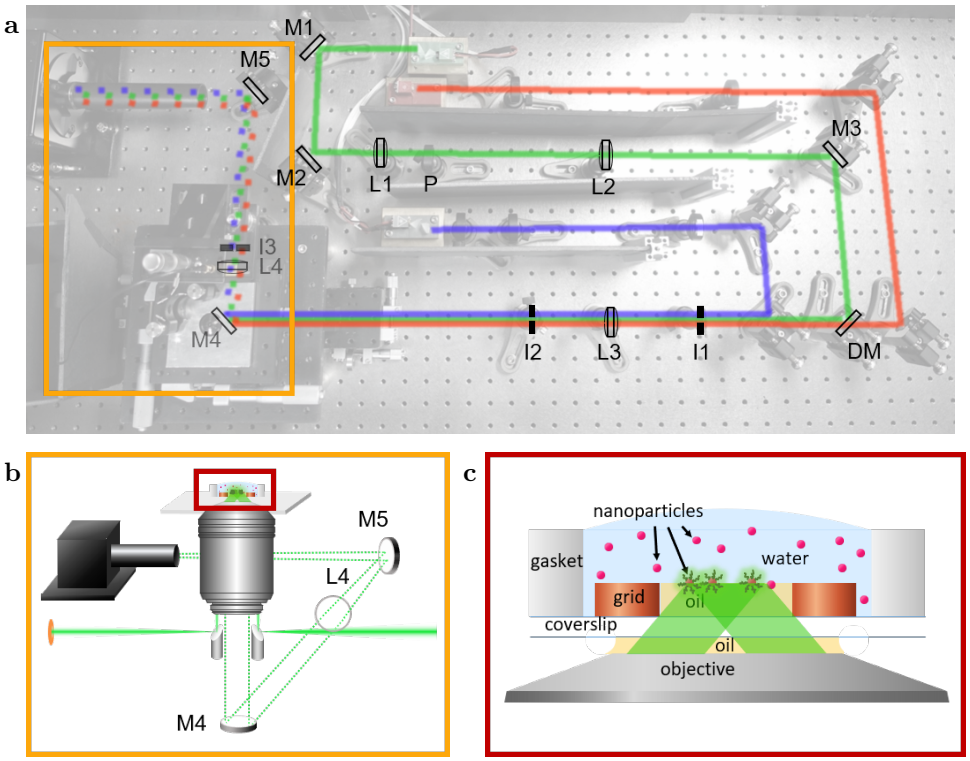


Figure 2.10: Total-internal-reflection dark-field (tir-df) microscopy setup. a) The beam paths are indicated by lines; solid before the sample and dotted where the light scattered by the sample is collected and focused onto the sensor of the camera. b) Schematic close-up view of the sample area; marked in orange in a). For clarity, only the 520 nm beam is shown and the iris I3 is omitted. c) Schematic close-up view of an interface on a coverslip above the objective; marked in b) in dark red. The totally internally reflected beam is reflected by the oil-water interface and a small fraction of the incident light is scattered anisotropically by particles in the illuminated area.

The beam from a 1 W 520 nm diode laser (*Lasertack LDM-520-1000-C*) is directed through a lens L1 (f = 50 mm) followed by a 100 μm pinhole P in the focal plane of the lens. A 50 μm pinhole achieved an approximately

Gaussian beam profile, however, this caused a power loss of almost 90%. The 100 μm pinhole easily allowed 180 mW to pass, which is likely to be at the limit of what the objective can tolerate based on past experience in the group. The beam profile is not as close to Gaussian as with the smaller pinhole, however, and this is visible in that when a particle attached to glass is moved across the field of view, there are several intensity maxima with the change in lateral position. For many of the earlier experiments, a single-mode optical fibre was used instead, replacing the beam path between L1 and L2 in Fig. 2.10a. The beam is re-collimated using another lens L2 ($f = 200$ mm), and the beam is reflected by a mirror and a long-pass dichroic mirror DM that allows the beam from the 635 nm laser (*Lasertack LDM-635-200*) to pass but reflects the 520 nm beam. It then passes through another long-pass dichroic mirror included to allow coupling in of a 445 nm laser (*Lasertack LDM-445-2000-CC*), and is focused by a 400 mm achromatic lens L3 and optionally adjusted with two irises I1 and I2 before being reflected into the *Olympus Plapon 60XO* objective with NA 1.42 and working distance 150 μm by a micromirror. The beam is collimated by the objective and directed at the interface at an angle achieved by lateral displacement of the micromirror from the centre of the objective, leading to total internal reflection (see Fig. 2.10). A second rod mirror is used to remove the reflected

beam (shown in Fig. 2.10b, but not a), and the position of this beam can be used to infer the distance between the interface and the objective. The light scattered by the sample is collected by the objective, transmitted through an iris (not shown) to remove stray reflections, focused by a 400 mm achromatic lens L4 and directed through an iris I3 onto the camera chip of the *Photron FASTCAM Mini UX100 type 800KM - 16GB* camera (pixel size 10 μm). One pixel in the resulting image corresponds to 75 nm in this setup, chosen in relation to the expected spatial extent of the signal in the image to optimise localisation precision [88]. A typical field of view was 640 pixels wide, i.e. 48 μm; the other dimension varied with the imaging speed and desired movie length. An image is shown in Fig. 2.11.

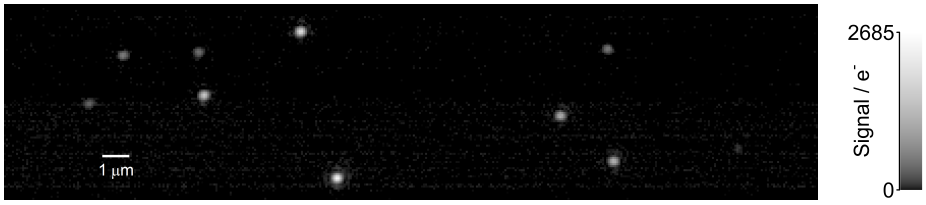


Figure 2.11: Photron UX100 image of 40 nm gold particles on glass; power density 17 μW/μm^2, exposure time 40 μs. The field of view is 30 μm wide (400×96 pixels).

2.3.2 Camera characterisation: Quantifiying the signal

To quantify the measured signal, the relationship between the digital numbers read from the camera and the number of photons arriving or the number of photoelectrons generated at the detector must be determined. The data on the specifications sheet provided by camera manufacturers may be an optimal or average value, so for quantitative measurements, it is often better to characterise the camera using the method of the photon transfer curve. [89] A more in-depth theoretical background can be found in Ref. [90].

The stochastic nature of the process of photons arriving at the detector makes it possible to convert the digital number displayed by the camera to the number of photoelectrons detected. The number of photoelectrons generated over the integration time of the camera chip (exposure time) follows a Poisson distribution, meaning that the expectation values for the signal and the variance of the signal are the same:

$$\sigma_{\text{shot}}{}^2 = S, \tag{12}$$

where S is the signal arising purely from electrons generated by arriving pho-

tons and σ_{shot} is its standard deviation. σ_{shot} is called shot noise. Because the above equation holds in units of photoelectrons, the digital number to electron conversion factor can be obtained by dividing the signal in digital units by the squared shot noise in digital units:

$$C' = \frac{S_{\text{DN}}}{{\sigma_{\text{shot,DN}}}^2}, \tag{13}$$

resulting in the digital number to photon conversion factor

$$C = \Phi_\lambda \frac{S_{\text{DN}}}{{\sigma_{\text{shot,DN}}}^2}, \tag{14}$$

where Φ_λ is the quantum efficiency (photoelectron to photon ratio) at photon wavelength λ.

With an ideal, noise-free camera, shot noise would be the only contribution to the noise, and the conversion factor could be determined by measuring the standard deviation of the digital signal as a function of the digital signal. In practice, there are sources of noise related to the experimental setup that must be taken into account. For signals that do not saturate the detector, the total noise of a low-light camera can be approximated by [89]

$$\sigma_{\text{total}}{}^2 = \sigma_{\text{read}}{}^2 + \sigma_{\text{shot}}{}^2 + \sigma_{\text{FP}}{}^2, \tag{15}$$

where the individual contributions are from read noise, shot noise and fixed-pattern noise. The read noise is the minimum operating noise of the camera and does not change with the signal. Fixed-pattern noise is due to differences between pixels. In CMOS cameras, the latter is a large contribution to noise measured over an image; however, it can be eliminated by treating individual pixels rather than the entire camera chip, which is what is done here to avoid overestimating the shot noise. When assessing individual pixels, the read noise is given by the standard deviation of the signal at temporally constant illumination [89], and the noise is dominated by shot noise when the read noise is subtracted or becomes negligibly small in relation to the other noise contributions, and before the sensor approaches saturation.

The photon transfer curve is a log-log plot of the noise, measured as the standard deviation of the signal, versus the signal. The region in which the total noise is dominated by shot noise scales linearly with the square root of the signal, and can be used to determine the proportionality constant between the squared shot noise (variance of the signal) and the signal, yielding the conversion factor between digital numbers and photoelectrons

(see Eqn. (13)). To obtain data pairs of signal and variance, time series of pixels are acquired at an ideally time-constant illumination. Here, a white screen (IPS LED) of a laptop plugged into the mains was used to illuminate the camera sensor, with a piece of paper inserted between the screen and the sensor to achieve different levels of illumination. For the dark image, the camera's dust cap was screwed onto the camera. Time series of 10000 frames were used. The resulting time-variance vs. time-mean values of each pixel at the various illumination intensities were collectively binned by mean value, yielding a data point for each movie file used, but correcting for spatial inhomogeneities in the illumination. The resulting photon transfer curve is shown in Fig. 2.12.

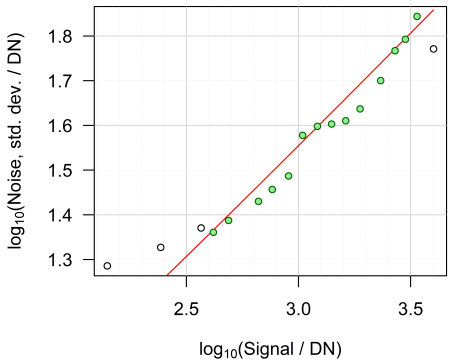


Figure 2.12: Photon transfer curve measured by binning the camera characterisation data (see text, below). From Eqn. (12), $\log_{10}(\sigma_{\mathrm{shot}}) = 0.5 \log_{10}(S)$, i.e., in the shot-noise limited region, the logarithm of the noise is expected to scale linearly with the logarithm of the signal, with a gradient of 0.5. The data points in this region, marked in green, were fitted with a linear model, yielding a gradient of 0.51. The intercept yields an expected gain of 0.96 DN/e^-. The data point with the lowest signal amplitude is omitted from the graph.

To obtain a spatial map of the conversion factor, the pixels were also assessed individually (see Ref. [91]). To calculate the gain, the offset, the dark mean pixel value, is subtracted from the rest of the data set. Offset and read noise (dark noise) and gain maps are shown in Figs. 2.13a and b, respectively, and a gain map is shown in Fig. 2.13c, using only the datasets in the shot noise-limited region of the photon transfer curve as identified in Fig. 2.12. Spatially averaged values can be found in Tab. 2. The spatially averaged gain value is used for the entire camera chip since the distribution is quite narrow.

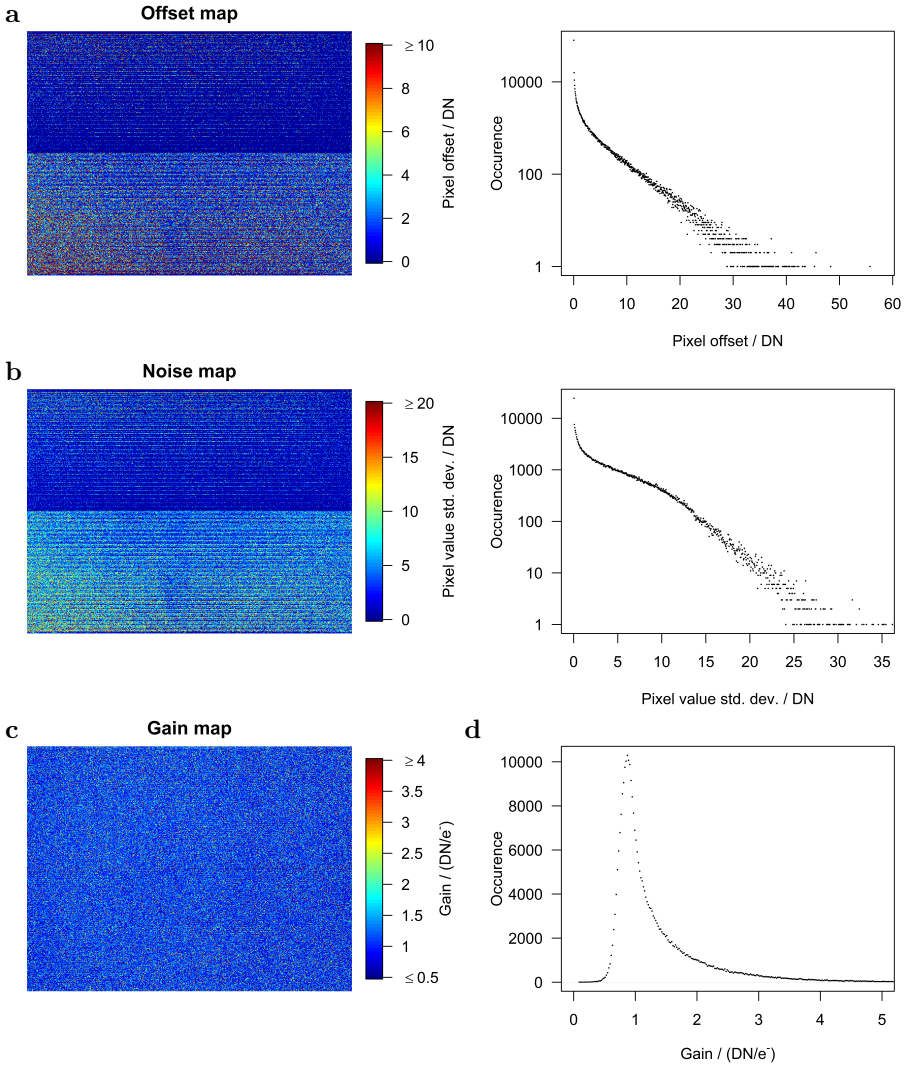


Figure 2.13: Maps of the 640x480 pixel area in the centre of the camera chip used for the measurements. a) Dark offset, b) dark noise, c) gain; pixel maps (left) and corresponding histograms (right). The width of the gain distribution is likely to be overestimated because inhomogeneities in the illumination profile are likely to have an effect given the small signal window of the photon transfer curve (PTC) used, i.e. not every pixel is evaluated in the same region of the PTC. In the setup shown in Fig. 2.10, this area of the camera chip corresponds to a 48 μm×36 μm field of view.

Table 2: Spatially averaged (median) values of the camera characterisation data.

	Digital number	Photoelectrons
Offset	0.59	0.57
Noise (std. dev.)	2.51	2.41
Gain	1.04	1
Conversion factor C	1	0.96

The noise measured experimentally overestimates the camera noise, with temporal fluctuations of the illumination intensity and possibly other factors contributing to the measured noise. The laptop screen brightness fluctuates measurably, however, the amplitude is small (<1%) relative to the amplitude of the signal.

2.3.3 Signal-to-background and signal-to-noise ratios

The signal-to-background ratio (SBR) is calculated as

$$\mathrm{SBR} = \frac{I_\mathrm{s}}{I_\mathrm{b}}, \tag{16}$$

and the signal-to-noise ratio (SNR) as

$$\mathrm{SNR} = \frac{I_\mathrm{s} - I_\mathrm{b}}{\sqrt{{\sigma_\mathrm{s}}^2 + {\sigma_\mathrm{b}}^2}}, \tag{17}$$

where I_s and I_b are the signal and background intensities (mean over 100 frames), and σ_s and σ_b the signal and background noises (standard deviation over 100 frames), respectively. A 16x16-pixel field of view including a particle is used for the signal and an adjacent area of the same size that does not contain a particle for the background (see Ref. [76]). The results are shown in Fig. 2.14.

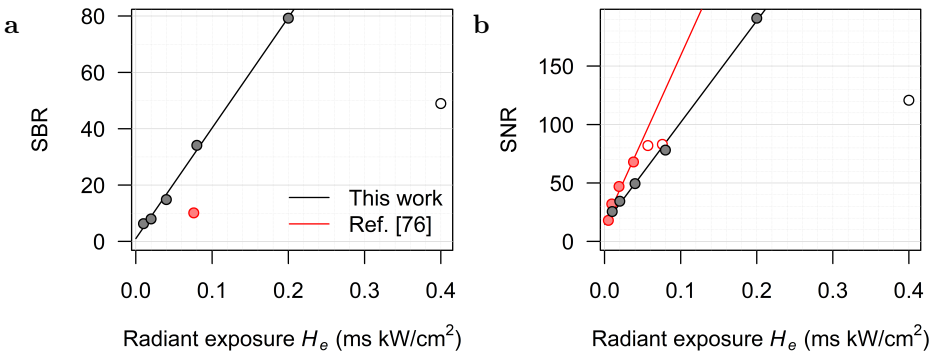


Figure 2.14: Signal-to-background (SBR) and signal-to-noise ratio (SNR) vs. radiant exposure. a) SBR, b) SNR. The data was obtained using 40 nm gold particles; the laser power was 14 mW and the FWHM of the illumination spot is estimated to be at least 30 μm, yielding a power density of 2 kW/cm^2. Solid points are used to fit a linear model, with slopes of 390 SBR and 870 SNR/(ms kW/cm^2), respectively.

We achieve a similar SNR to radiant exposure (laser power density multiplied by exposure time) ratio as the state of the art [76], and an SBR that

additionally enables us to push the limit of detection towards smaller particles. In Ref. [76], the curve of SNR vs. radiant exposure flattens off at high radiant exposures because the signal becomes saturated at the detector. In this work, the background noise as well as the variance of both signal and background increase disproportionately, causing the SNR to not only plateau but even drop when the signal becomes saturated at the detector.

Fig. 2.15 illustrates the very low background with a line cut through a 20 nm particle. In addition, the Gaussian fit (see chapter 3) is very close to the experimental data.

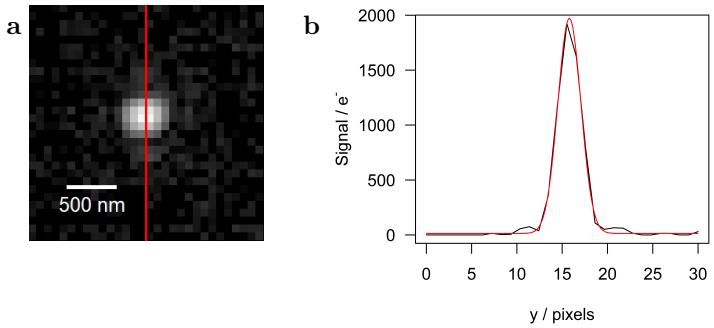


Figure 2.15: 20 nm gold particle at an oil-water interface; illumination wavelength 520 nm, power density 4500 kW/cm^2, exposure time 100 μs. a) Raw image. b) Amplitude as a function of position (black). Red: Gaussian fit. One pixel corresponds to 75 nm.

2.3.4 Localisation precision

An approximate value for the expected localisation precision is given by [88]

$$\langle \Delta x \rangle_{\text{predicted}} = \sqrt{\frac{s^2 + a^2/12}{\Phi N'} + \frac{8\pi s^4 (\Phi b')^2}{a^2 (\Phi N')^2}}, \tag{18}$$

where N' is the number of photons collected, Φ is the quantum efficiency of the detector, s is the standard deviation of the point spread function (the signal produced by the particle on the camera, see section 3.1.1 for details), a is the pixel size in the image and b' is the background signal in units of photons. Substituting photons with the number of photoelectrons N yields

$$\langle \Delta x \rangle_{\text{predicted}} = \sqrt{\frac{s^2 + a^2/12}{N} + \frac{8\pi s^4 b^2}{a^2 N^2}}, \tag{19}$$

where b is the background signal in units of photoelectrons. These equations underestimate the localisation error by about 10% in the transition region between the two limiting cases of shot noise-dominated ($\sim 1/\sqrt{N}$) and background noise-dominated ($\sim 1/N$) behaviour.

In principle, the experimental localisation precision is given by the standard deviation of the position of a stationary particle. Any mechanical drift or external perturbations, i.e. movements of the sample and other components of the imaging system with respect to the camera, will lead to an overes-

timate of the localisation error. To avoid this, several stationary particles were imaged in one movie file and the standard deviation of the distance between particles was used, resulting in an experimental localisation precision of

$$\langle \Delta x \rangle_{\mathrm{exp}} = \left\langle \frac{1}{\sqrt{2}} \sigma \left(\mid \Delta r_{ij} \mid \right) \right\rangle_{ij}, \tag{20}$$

where r_{ij} is the distance between two particles i and j, σ is a standard deviation operator and the brackets denote a mean value over all the particle pairs in the movie.

The characterisation experiments for the experimental setup were done by adding a solution of 40 nm gold particles in motility buffer to a glass flow cell. Gold particles supposedly stuck to the surface of the glass have been observed to move laterally, so the actual localisation precision may be higher than the results presented below.

The localisation precision of our TIR-DF microscope is shown in Fig. 2.16.

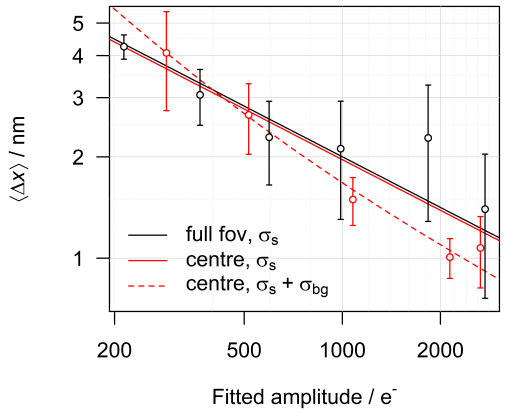


Figure 2.16: Localisation precision vs. number of photoelectrons; the data for the full field of view is shown in black and the data for the centre of the field of view in red. The conversion factor of 0.96 e^-/DN between digital numbers and photoelectrons is based on the data in Fig. 2.13. Solid lines represent fits taking only shot noise into account (see text for model), the dashed line represents a fit using Eqn. (19), i.e. including a shot noise and a background term.

Fits to a shot noise-only model $\langle \Delta x \rangle = \sqrt{b_1/N}$ yield an expected standard deviation of the point spread function of $s = 60$ nm for both data sets, using $b_1 = s + a_2/12$ for the first term of equation (19), with $a = 75$ nm. A fit to the data from the centre of the field of view taking background noise into account, $\langle \Delta x \rangle = \sqrt{b_1/N + b_2/N^2}$, where $b_2 = (8\pi s^4 b^4)/a^2$, gave an expected standard deviation of the point spread function of $s = 40$ nm and a background signal in electrons $b = 4$. The same fit is not included for the full-chip data because the fitting algorithm did not produce a meaningful result. The standard deviation of the point spread function of 60 nm expected

from the localisation precision (Eqn. (19)) is significantly smaller than the experimental value of > 100 nm. This is likely due to the fundamental limitation of optical systems (see section 3.1.1).

3 Analysis Methods

I wrote the analysis programs described in this chapter and produced and analysed all data presented, with the exception of the simulated trajectories discussed in Fig. 3.2, which were produced by Adar Sonn-Segev.

This chapter explains how the experimental data was processed to yield information on particle dynamics in a form that enables the observation of trends and comparisons between different data sets. To obtain quantitative information from movies of particles diffusing at an interface, the particles are detected and linked into trajectories using a program that was home-written in LabVIEW 2011. The program also enables visualisation and further processing of the results. An additional program for analysis and visualisation was written in R as the quality of graphs was higher and the non image-based analysis was made significantly faster and simpler by text-based programming.

Section 3.1 introduces the quantities used to characterise the particle dynamics at the interface. Section 3.2 describes the LabVIEW program, including the algorithm used to track the particles to yield an array of properties for each tracked particle and the analysis of this data (section 3.2.2).

3.1 Observables

The signal produced by a particle on the camera contains information on the particle and the imaging system. Particle trajectories contain information on the diffusive behaviour, and possibly dynamics within the observation time. Ensembles of trajectories can be used to characterise averaged behaviours, which are expected to vary with particle size and interface type.

Section 3.1.1 describes the relationship between the immediate results from the tracking algorithm and the particle and imaging system. Section 3.1.2 introduces diffusion, expected in-plane dynamics for a particle adsorbed at an interface with a fixed contact angle, how the experimental data can be interpreted within this model and how anomalies present themselves in the data. Section 3.1.3 introduces observables quantifying deviations from the predominant dynamics, both within trajectories and within ensembles.

3.1.1 Observables obtained directly from the tracking algorithm

In optical imaging systems, particles that are significantly smaller than the spatial resolution of the detection system produce a signal on the detector that can be approximated by the response of a point source. The funda-

mental limit to optical resolution approximated by Ernst Karl Abbe is

$$d = \frac{\lambda}{2n\sin(\theta)} = \frac{\lambda}{2\mathrm{NA}}, \tag{21}$$

where d is the smallest distance at which two point sources of light can be resolved as separate scatterers, λ is the wavelength of the scattered light, n is the refractive index of the medium and θ is the half-angle of the cone from which light is collected from the scatterer. NA is the numerical aperture of the imaging system, in this work the objective. d is approximately 180 nm for our TIR-DF microscope with $\lambda = 520$ nm. The image of a gold particle in this work (with diameter $\leq 80\ nm$) is therefore well described by a point spread function, which is the image produced by a point source.

The point spread function has the shape of an Airy function (see Fig. 3.1), which features a high-amplitude central disk surrounded by concentric circles that rapidly decrease in amplitude.

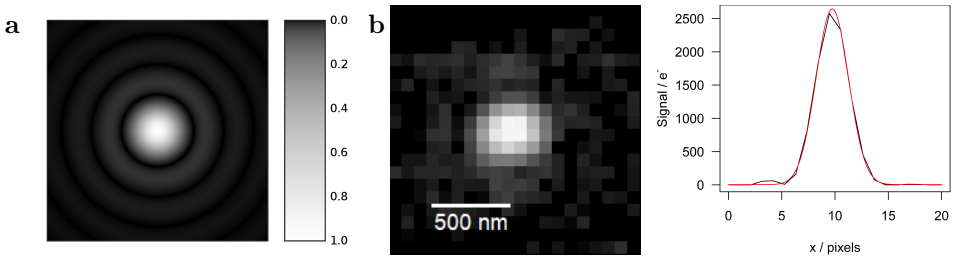


Figure 3.1: Theoretical, experimental and fitted point spread function. a) Airy function (theoretical), from https://commons.wikimedia.org/wiki/File:Airy-pattern.svg, accessed 08/06/2020. b) Experimental signal. c) Gaussian fit of the particle in b) (includes another 15 pixels on each side).

The Airy function has a complicated form, but is well approximated with a Gaussian [71] (see Fig. 3.1c). In the tracking algorithm, the point spread function of each particle is fitted with a model Gaussian,

$$S(x,y) = A\exp\left(-\frac{(x-x_0)^2}{2{\sigma_x}^2}\right)\exp\left(-\frac{(y-y_0)^2}{2{\sigma_y}^2}\right) + b, \tag{22}$$

where A is the fitted scattering amplitude, x and y are the in-plane spatial coordinates, with the centre of the particle given by (x_0, y_0), σ_x and σ_y are the standard deviations of the Gaussian in x and y, respectively, and b is a scattering amplitude offset.

Amplitude

The scattering amplitude, or simply amplitude, is the maximum value of the fitted Gaussian in photoelectrons, obtained from the camera readout via Eqn. (14) (see Fig. 2.12). The amplitude increases with the particle size d via $A \propto d^6$ (see Eqns. (6) and (8)) under the same imaging conditions. It also varies with the position of the particle within the profile of the illumination beam, which limits the accuracy of this quantity when the position within the horizontal plane changes significantly, i.e. over the course of longer observation times, and makes it difficult to compare different trajectories with each other. Quantitative comparisons between different trajectories in this work are also made difficult by changing laser powers used. Within individual trajectories, the amplitude can give an indication of the immersion depth of the particle within the interface, as particles that are more immersed in the oil phase are expected to have a higher scattering amplitude than particles that are more immersed in the water phase since the illumination intensity decreases rapidly above the interface (see Eqn. (11)). This makes the amplitude a valuable tool in characterising the dynamics of individual particles.

Intensity

The intensity is used to estimate the total number of photoelectrons produced by a single particle. It is calculated as an integral over the Gaussian fit of the point spread function,

$$I = 2\pi(A - b)\sigma_x\sigma_y, \tag{23}$$

where the variables are the fitting parameters from Eqn. (22). Compared to simply using the sum of the signal over a small field of view around the particle, this is expected to be less sensitive to background noise.

The intensity can be used in a similar way to the amplitude, the difference being that it takes into account the changing distribution of the scattering signal in the image plane if the particle moves a short way perpendicular to the interface and focal plane. For this reason, it generally appears less noisy. For poor signal-to-noise ratios, however, the width of the point spread function often varies significantly more than what would be expected at higher signal-to-noise ratios, and the intensity can fluctuate sharply, which is believed to be an artefact due to the Gaussian model describing the scattering response less well when the particle is not in the focal plane.

In this work, as with the amplitude, the intensity is used with care when comparing different trajectories as it depends heavily on experimental conditions.

Lateral position

The position vector $\vec{r}_i$ of particle i is obtained from the fitted in-plane position (x_i, y_i) in pixel units on the camera using the magnification of the microscope:

$$\vec{r}_{\mathrm{i}} = \frac{M\ f\ \text{pixel size}}{\text{tube length}} \begin{pmatrix} x_{\mathrm{i}} \\ \\ y_{\mathrm{i}} \end{pmatrix}, \tag{24}$$

where M is the magnification of the objective, f is the focal length of the imaging lens, the pixel size refers to the the camera (see section 2.3 for the numbers for the main setup) and x_{i} and y_{i} are the pixel values obtained from the tracking algorithm, corresponding to x_0 and y_0 in the fitting model described by Eqn. (22).

For most of the data in this work, the conversion factor from pixels to spatial distances is 75 nm/pixel; for the setup used for some of the experiments described in chapter 4, it is 80 nm/pixel.

Standard deviation of the Gaussian fit

When the particle is not exactly in the focal plane, its image is distorted, and its standard deviation (width) increases rapidly with the distance from the focal plane. The fitted widths σ_x and σ_y of the point spread function in the two in-plane dimensions x and y are therefore an indicator of the distance of the particle from the focal plane. However, it is not as reliable a measure as the intensity or amplitude and instantaneous diffusion coefficient (see below), as the shape of the point spread function deviates from Gaussian significantly when the particle is not in the focal plane, resulting in strongly fluctuating values for the standard deviation. It is primarily used to calculate the intensity of a scatterer.

3.1.2 Diffusive behaviour

At sampling rates that are not significantly shorter than the momentum relaxation time (see section 1.2.5), it is not possible to measure the instantaneous velocity of a particle. Rather than describing the dynamics in an inertial way, where the velocity and forces at one sampling point can be used to predict these quantities at the next sampling point, the particle motion is described by a random walk, with rapid fluctuations of the liquid

molecules around it giving rise to a force that appears random on the experimental timescale. In this description (Brownian motion), the localisation probability density distribution function of a particle is given by

$$P(\vec{r},t) = \frac{1}{(4\pi Dt)^{n/2}} \exp\left(-\frac{\vec{r}^2}{4Dt}\right), \tag{25}$$

where $\vec{r}$ is the spatial position vector of the particle, t is the time elapsed since the beginning of observation, D is the diffusion coefficient (see below) and n is the dimensionality of the diffusive motion (see e.g. Ref. [8]). Deviations from Brownian motion occur in this work, and are treated below.

Time-averaged mean squared displacement (msd) and diffusion exponent α

The mean squared displacement, defined as the ensemble-averaged squared spatial displacement MSD $\equiv \langle \Delta\vec{r}^2 \rangle$ over the time interval τ, is an indicator of whether the system is truly Brownian, i.e. fulfills Eqn. (25), and, if not, how its behaviour deviates from it. The time dependence of the MSD may vary depending on physical processes underlying the dynamics, for example interfacial rheology, and is therefore an important tool in characterising the diffusive behaviour.

Given that in a real system of nanoparticles at an interface, particles are not perfectly identical, and that studies such as this one have limited statistics, it is practicable to use a time-averaged MSD instead of an ensemble-averaged one. In this work, the MSD of a trajectory is therefore defined as the displacement of a particle over a time interval τ:

$$\text{MSD} = \overline{\Delta\vec{r}(\tau)^2} = \overline{(\vec{r}(t+\tau) - \vec{r}(t))^2} \tag{26}$$

The bar denotes an average over the time variable t.

From Eqn. (25), with t replaced by τ as the ensemble average is replaced with a time average, the MSD of a particle moving in two dimensions is expected to follow

$$\text{MSD} = 2nD\tau = 4D\tau. \tag{27}$$

Where the MSD is not linear with respect to τ, i.e.

$$\text{MSD} = 2nD'\tau^{\alpha} = 4D'\tau^{\alpha}, \tag{28}$$

the motion is referred to as anomalous. Motion is termed subdiffusive for $0 < \alpha < 1$, Brownian for $\alpha = 1$, superdiffusive for $1 < \alpha < 2$, ballistic for $\alpha = 2$ and hyperdiffusive for $\alpha > 2$. D' is a constant, and equal to the diffusion coefficient if $\alpha = 1$.

The diffusion exponent α is calculated from a fit of the experimental MSD as a function of the time interval to Eqn. (28). It may be systematically underestimated at poor localisation precisions as displacements over short time intervals are disproportionately affected by the error (see section 7.3 for a brief discussion of the effect on our data).

Diffusion coefficient

The diffusion coefficient D is a measure of the area sampled by the particle in a given time. It is defined in Eqn. (25) and is experimentally determined from a linear fit to Eqn. (27). In addition, it is related to the viscosity of the surrounding medium via the Stokes-Einstein relation $D = \frac{k_B T}{6\pi R\eta}$, where k_B is the Boltzmann constant, T is the temperature, R is the particle radius and η is the dynamic viscosity of the surrounding medium. This yields a three-phase contact angle of the particle at the interface based on the area fraction of the particle in each liquid via Eqn. (4).

In this work, the diffusion coefficient is systematically overestimated when the localisation precision decreases (see Fig. 3.2).

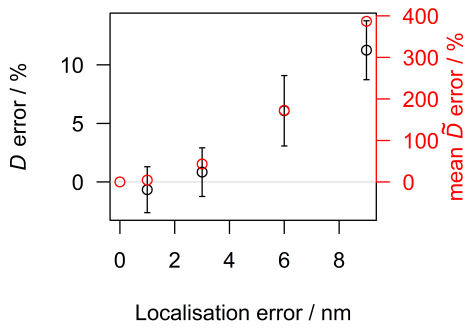


Figure 3.2: Relative difference between diffusion coefficients D and trajectory-averaged instantaneous diffusion coefficients $\tilde{D}$ of simulated trajectories with non-zero localisation error and a simulation with no localisation error. Error bars correspond to standard deviations over the ensemble of trajectories. Five trajectories of 100000 frames were used for each simulation.

This is likely a result of systematically overestimated displacements at short time intervals, as supported by a much larger trajectory-averaged instantaneous diffusion coefficient (see below) for larger localisation errors.

Instantaneous diffusion coefficient

To characterise changes in diffusion that occur within the experimental observation time interval, it is useful to define an instantaneous diffusion coefficient $\tilde{D}$. It is defined in analogy to the diffusion coefficient based on a trajectory (see Eqn. (27)), applied to a single frame:

$$\tilde{D}(t) = \frac{\Delta\vec{r}(t)^2}{4\tau} = \frac{(\vec{r}(t+\tau) - \vec{r}(t))^2}{4\tau}, \tag{29}$$

where t is a point in time, $\vec{r}$ is the position vector of the particle and τ is the time difference between measurements.

In this work, the instantaneous diffusion coefficient is systematically and dramatically overestimated when the localisation error increases (see Fig. 3.2).

3.1.3 Deviations from averaged behaviour

The description in section 3.1.2 assumes Brownian motion at a constant diffusion coefficient, which is not always the case in our observations. The character and magnitude of the deviation from Brownian and other uniform behaviour can be probed both within trajectories and across an ensemble of trajectories.

Non-Gaussian parameter (NGP)

Eqn. (25) leads to a Gaussian displacement distribution. Deviation from the Gaussian form of distributions can be quantified using the NGP [92]. It is defined as

$$\text{NGP} = \frac{\langle \Delta x(\tau)^4 \rangle}{3\langle \Delta x(\tau)^2 \rangle^2} - 1, \tag{30}$$

where x is a time-dependent observable such as the lateral position and Δx is the difference between two values that are adjacent in time. An NGP that is greater than zero represents a deviation from Gaussian behaviour. For example, for the step size distribution in the lateral position (see Fig. 3.3), a Gaussian distribution is contrasted with a distribution that deviates from this.

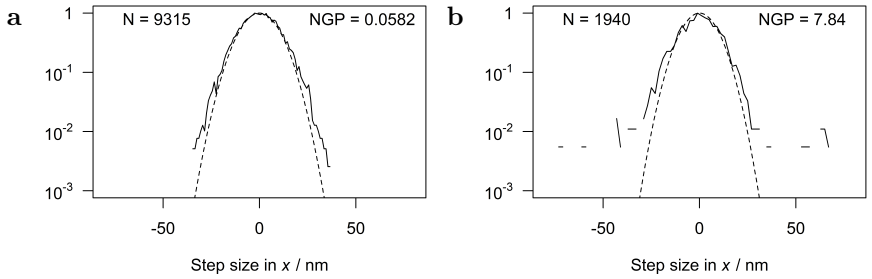


Figure 3.3: One-dimensional step-size density distributions of 40 nm gold particles. a) A trajectory with a non-Gaussian parameter of 0.06, with no apparent motion perpendicular to the interface. The diffusion coefficient is 0.32 $\mu\text{m}^2\text{s}^{-1}$; the mean step size in x 8.4 nm. b) A trajectory with a non-Gaussian parameter of 7.8, with an adsorption event near the beginning of the trajectory (note the small fractions of large step sizes). The diffusion coefficient is 0.39 $\mu\text{m}^2\text{s}^{-1}$; the mean step size in x 8.7 nm.

A small number of fast diffusive steps within an otherwise near-Brownian

trajectory leads to a large NGP (see Fig. 3.3b), making it easy to identify such trajectories. Different anomalous behaviours however, such as several similar and similarly represented diffusive states or a series of slow diffusive steps within a near-Brownian fast-diffusing trajectory, do not lead to a large NGP, limiting its usefulness for single trajectories in this work to specific behaviours. Ensemble step-size distributions can also be compared with each other using the NGP.

In this work, we separate distributions in x and y as they are slightly different for reasons related to the camera function.

Ergodicity breaking parameter (EBP)

In an ergodic system, time-averaged properties approach ensemble-averaged values in the limit of long observation times and large ensembles. This is expected for Brownian motion. Deviation from this behaviour, for example when particles are temporarily trapped or undergo a sudden change in diffusive behaviour, can be expressed with the ergodicity breaking parameter [8]

$$\text{EBP} = \langle \xi^2 \rangle - 1, \tag{31}$$

where the brackets denote an ensemble average and $\xi = \overline{\Delta\vec{r}^2(t)}/\langle\overline{\Delta\vec{r}^2(t)}\rangle$, where $\Delta\vec{r}(t)$ is the displacement at time t and the bar denotes a time average. The ξ value of a trajectory represents the extent to which it is different from the ensemble average — different processes have different distributions $\phi(\xi)$.

Correlation coefficient

Correlation between different observables can be used to determine the source of changes and fluctuations in a particular variable. For example, the intensity is expected to decrease with an increasing instantaneous diffusion coefficient if there is out-of-plane motion (see section 5.1 for details), and this can be made visible using the correlation coefficient. Correlations can also be assessed on an ensemble level, for example to determine whether confinement (measured by the diffusion exponent) coincides with diffusivity.

Correlations between different observables along the time axis were measured by calculating the Pearson correlation coefficient:

$$r_{\mathrm{P}} = \frac{\mathrm{cov}(X,Y)}{\sigma_X \sigma_Y} = \frac{\langle (X(t)-\mu_X)(Y(t)-\mu_Y)\rangle}{\sigma_X \sigma_Y}, \tag{32}$$

where cov(x,y) is the covariance of two variables x and y, X and Y are

the variables in question, μ_x and σ_x are the respective mean and standard deviation of the dataset x and angular brackets denote time averages. The correlation coefficient is equal to 1 when the two observables are perfectly correlated, -1 when they are perfectly anti-correlated and 0 when they are uncorrelated. An example is illustrated in Fig. 3.4.

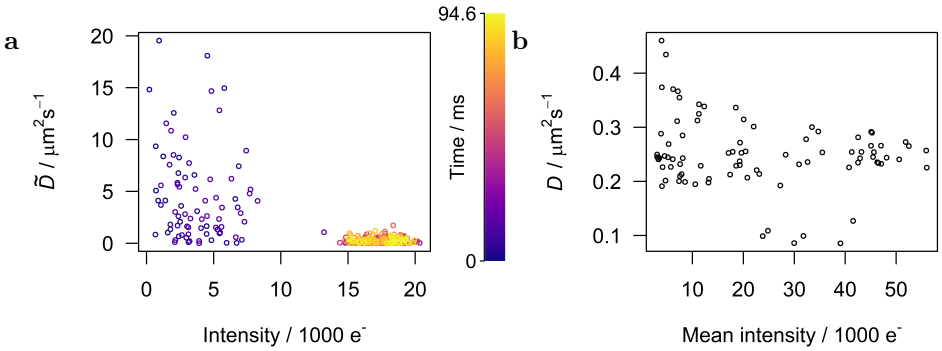


Figure 3.4: Correlation analysis between scattering intensity and diffusive behaviour within a trajectory and within an ensemble of trajectories. a) Instantaneous diffusion coefficient $\tilde{D}$ vs. intensity for a 40 nm gold particle adsorbing to a surfactant-free interface, with colour representing time (472 data points, sampling rate 5 kHz). The Pearson correlation coefficient is -0.66. b) Diffusion coefficient vs. trajectory-averaged intensity for trajectories of 40 nm gold particles diffusing at a surfactant-free interface (86 trajectories, sampling rate 12.5 kHz). The Pearson correlation coefficient is -0.20.

In this work, the correlation coefficient between properties that are defined for every frame in a trajectory, such as the intensity, and properties that are based on differences between frames, such as the instantaneous diffusion coefficient, contains all data points in the first property except the last one.

3.2 Data analysis

Our analysis software had to fulfill three main functions: visualising the data, tracking particles and calculating relevant properties from the tracking results. The combination of these functions was not readily available, especially with the need for highly adjustable tracking parameters to enable the tracking of particles at the detection limit and particles in different environments — experimental conditions included a wide range of different particle densities and diffusive regimes, as well as different levels of background scattering relative to the particle signal. As requirements evolved with the development of the sample and a changing imaging system, we considered writing custom software to be the easiest way to obtain the specialised and adaptable toolkit we needed.

Firstly, to efficiently work with the data, it is useful to be able to view the movies before tracking particles, for example to determine whether a file is likely to be usable, to decide where to set the amplitude threshold for particle detection and, initially, for developing the assay and building and characterising the microscope. The visualisation part of the program is described in section 3.2.1. Secondly, a tracking algorithm was written

to yield Gaussian fit parameters for each particle and frame, linked into trajectories for different particles. This is described in section 3.2.2. Finally, the trajectory array can be used to visualise observables as a function of time, compare different trajectories and calculate the properties discussed in section 3.1.

3.2.1 Visualisation

The movies can be viewed with a slider to select a frame of interest. The brightness scale can be adjusted if there are particles of different intensities in the frame or different background amplitudes. Movies can be cropped to select a field of view and a time window, which can also be applied when tracking to save time when data volumes are high.

Fitted trajectories can be overlaid onto the original movie to assess the quality of the fit and identify which trajectories belong to which particle. This is especially important in situations in which the tracking algorithm does not perform as well, e.g. for dim particles, during adsorption and desorption events, and while developing the analysis program. The tracking results in terms of the parameters of the Gaussian fit (see section 3.2.2) for the selected particle and frame are visible next to the image, as is a residual

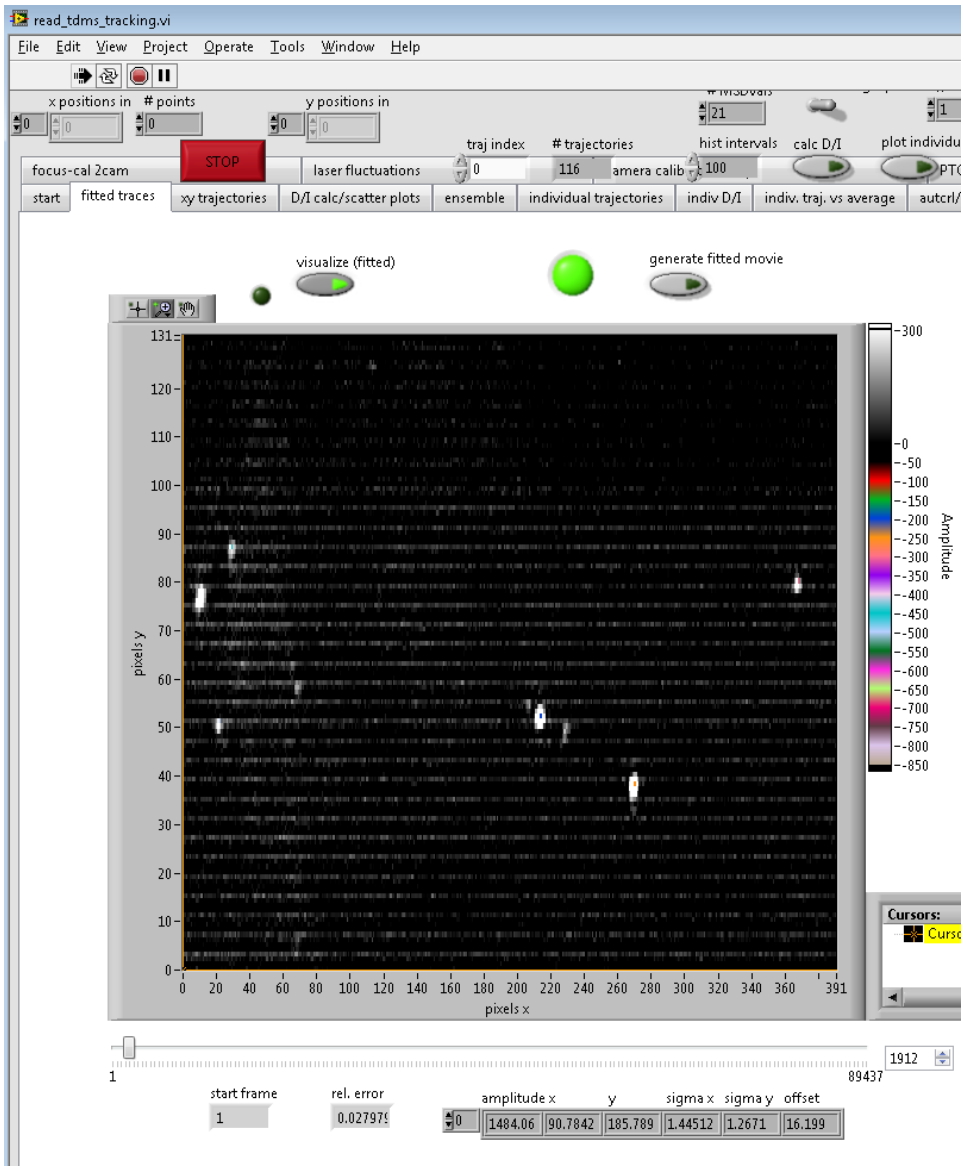


Figure 3.5: Screenshot of the part of the program that visualises tracking results. The movie frame shows 20 nm gold particles at an interface. Tracked particles are marked by differently coloured pixels. Below this, there is a slider for the selection of frames within the movie. Trajectories are selected using a control (*traj index*) near the top of the screenshot. Fitting parameters for the selected trajectory, as well as the frame in which the trajectory starts and the relative error — given by residual of the fit divided by the fitted amplitude — are displayed beneath the slider for the given frame.

Other visualised results include observables of tracked particles as a function

of time within a trajectory, time and ensemble histograms, and scatter plots of two observables either over time or over an ensemble, using trajectory-averaged values.

When results were plotted as observables as a function of time, time-averaging was sometimes applied to aid visualisation: Values were replaced with a mean value of the data point and the n adjacent data points to either side, i.e.

$$\bar{x}_{i,n} = \frac{\sum_{j=i-n}^{i+n} x_j}{2n+1}, \tag{33}$$

where i is the index of the data point and $n' = 2n+1$ is the number of data points averaged.

3.2.2 Tracking algorithm

The algorithm used in this work to track the particles is illustrated in Fig. 3.6. Particles are detected and linked from one frame to the next to yield a trajectory array containing, for each particle at each point in time, a fitted amplitude, in-plane coordinates, widths in x and y and an amplitude

offset. The individual steps of the tracking algorithm are described below.

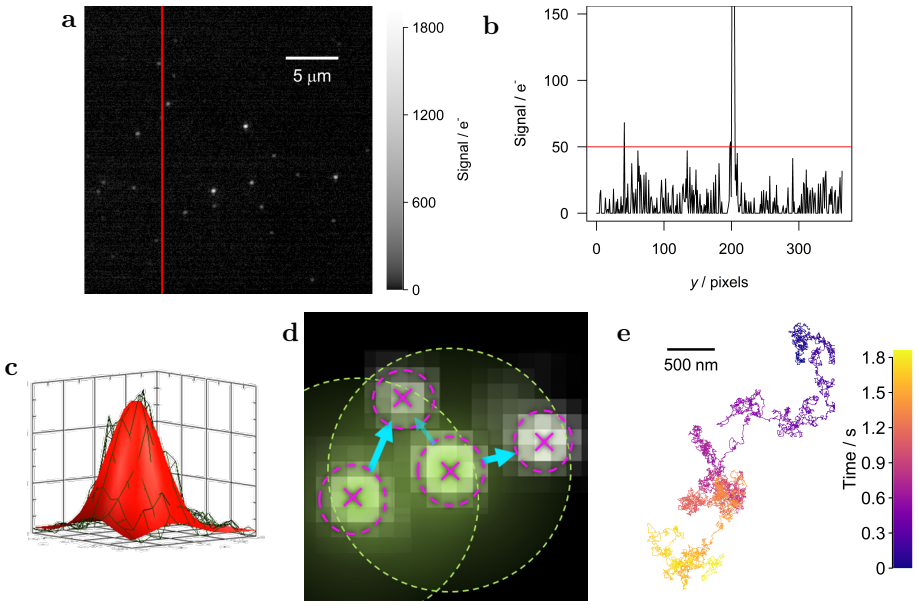


Figure 3.6: Illustration of particle tracking algorithm. a) Visualisation: One frame from a movie of 20 nm gold particles at an interface. b) Detection: Line cut from a) (marked in red in a)). Local maxima within groups of pixels with a signal above a variable threshold are automatically selected. c) Detection, continued: Two-dimensional Gaussian functions are fitted to the identified peaks for each frame, yielding a fitted amplitude, two-dimensional spatial coordinates, width of the point spread function (standard deviation of Gaussian) in two dimensions and an amplitude offset. d) Linking: Frames are connected to yield particle trajectories. Whether fitted Gaussians in adjacent frames are linked is based on proximity and brightness (see text). e) Visualisation of results: Two-dimensional particle trajectory obtained by linking in-plane spatial coordinates.

3.2.2.1 Detection

Detection occurs in two steps as described in detail below: First, a threshold is applied to the image (which is optionally median-filtered — see below) and within detected areas (i.e. the pixels with signal values above the threshold, see Fig. 3.6b) brightness maxima are selected. After this, a two-dimensional Gaussian function is fitted to the areas around the maxima.

Median filtering

Applying a median filter can significantly lower the detection limit by improving the SNR. A median filter is an image obtained by taking the median of each pixel value over the course of a movie or a section of it (see Fig. 3.7).

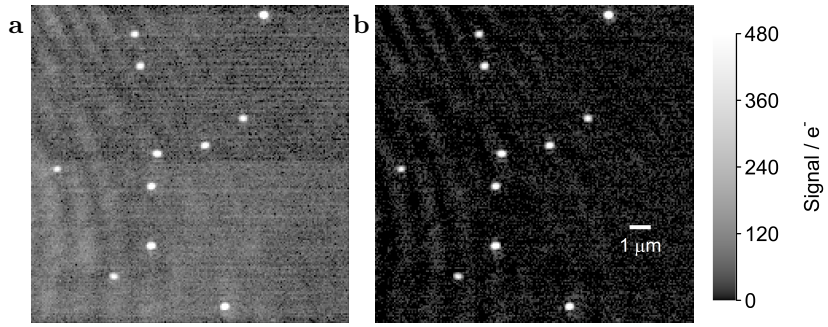


Figure 3.7: Illustration of median filtering using 20 nm gold particles at an interface. a) Before, b) after subtraction of a 2000-frame median filter. The frame rate was 500 Hz.

The median filter is subtracted from each raw image to improve the signal-to-background ratio. This can very effectively remove stationary background signals when the object of interest is in motion. The filter can be taken over the entire movie or parts of it. Deeper median filters, with more movie frames, are more appropriate when particles move slowly; shallower ones, with fewer frames, give better results when the background changes quickly. The main use for this was during the development of the microscope and interface sample, as sample quality was lower. Median filtering can adversely affect detection if the number of frames used is too small compared to the in-plane velocity of the particle. In this case, the particle is subtracted as part of the background and the background subtraction both reduces the SNR and distorts the shape of the detected point spread function, leading to artefacts in the detected scattering intensity and diffusive behaviour (see Fig. 3.8). For this reason, median filters were rarely used to process high-speed (> 1000 kHz) data.

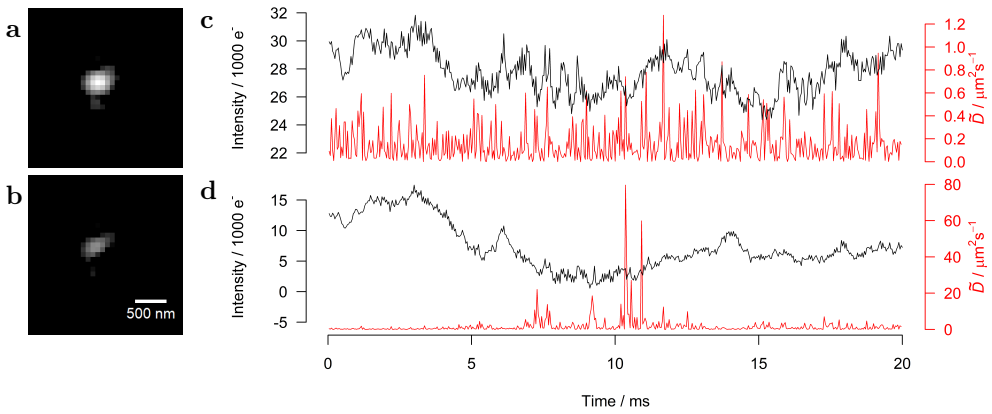


Figure 3.8: Artefacts arising from unsuitable median filters. a) Raw image of a 40 nm gold particle at an interface. b) The same image with subtracted median filter. c)-d) Intensity (black) and instantaneous diffusion coefficient (red) as a function of time, tracked using the raw data (c), and with a median filter applied (d). The sampling rate was 50 kHz and the median filter depth was 500 frames.

Applying the threshold

The threshold must be set low enough to allow detection of as many particles as possible in the movie, the signals of which may vary significantly, but high enough to allow high-speed data processing, given that movies may contain over 100,000 frames. The fact that a Gaussian fitting algorithm must converge places a lower limit on the signal collected from a particle — if the signal is too low, the point spread function is often too noisy to be fitted despite the particle being visible by eye. In a small-scale test using a particle on glass imaged with different exposure times, it was feasible to

track the particle with an SNR of 3.8 without using different thresholds for different sections of the trajectories. With an SNR of 1.8, this would have been difficult, and tracking particles with such a low SNR is only practicable for a very limited data volume, for example to link up higher-SNR trajectories with a lower-SNR section between them. At an SNR of 1.2, the particle could be visually distinguished against the background, but was virtually impossible to track using our algorithm. Besides signal intensity, detection is limited by distorted point spread functions (the fit does not converge for diagonally elongated peaks) and background noise near the particle (including unwanted experimental signals, e.g. from a passing particle in the water, or from spurious light reflections in the experimental setup).

The expected limit for the SNR [93] is 4, after which tracking performance tends to drop rapidly. This approximately reflects the findings in this work (see section 2.3.3 for the experimental SNR in this work).

Gaussian fitting

The model used to fit the particle point spread function (see section 3.1.1) is given by a Gaussian function

$$S(x,y) = A\exp\left(-\frac{(x-x_0)^2}{2{\sigma_x}^2}\right)\exp\left(-\frac{(y-y_0)^2}{2{\sigma_y}^2}\right) + b,$$

where A is the fitted scattering amplitude, x and y are spatial coordinates with the centre of the particle given by (x_0, y_0), σ_x and σ_y are the standard deviations of the Gaussian in x and y, respectively, and b is a scattering amplitude offset.

The size of the field of view for fitting each peak is a square of length 11–15 pixels, but can be adjusted, for example, smaller values can be useful to track particles near the edge of the camera field of view.

Where fits converge but do not represent the data well, the trajectories can optionally be filtered out at a later point in the algorithm.

The relative error is defined as the residual of the Gaussian fit divided by the fitted amplitude. Experimental values are given as a function of the fitted scattering amplitude in Fig. 3.9.

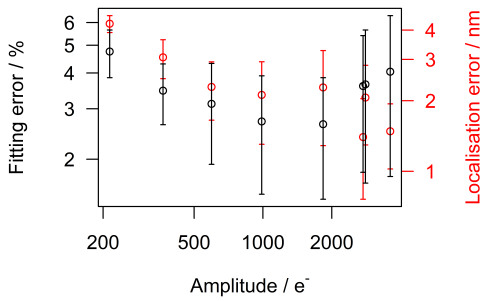


Figure 3.9: Relative fitting error vs. fitted amplitude. Each data point represents an average over the trajectories in one movie file, using particles on glass.

The fitting error decreases with increasing amplitudes in a similar way to the localisation error, but increases again near the saturation point of the camera chip (3931 e^-).

3.2.2.2 Linking frames into trajectories

Trajectories are obtained by linking Gaussian fits in consecutive frames. Linking is based on proximity (the distance d_{ij} between two particles i and j) and similarity in the fitted amplitude between the particles in the new and the preceding frames. New peaks are added to a trajectory array with an existing particle j and a minimum in-plane distance $d_{\min}$ for linking as follows:

i) If $d_{ij} \leq d_{\min}$, peak i is linked to particle j.

ii) If $d_{kj} \leq d_{\min}$, where k is after i in the loop over all new peaks, the peak for which $\Delta A_{xj} = |A_x - A_j|$ is smaller is linked to particle j, where x is either k or i.

iii) If $d_{ij} > d_{\min}$, a new trajectory is started for particle i.

Particles near the edge of the frame are not considered because the fit for them often converges to a result that can be seen to be far displaced from the point spread function when comparing the fit to the image data.

After each frame, discontinued trajectories that are shorter than a user-defined cutoff length are removed from the array to improve speed. Owing to the large amounts of data processed (the data from one interface sample can take up up to 500 GB of disk space, and movies can contain over 270,000 frames), speed is important to make the data analysis feasible, which also means that not all data can be reanalysed if trajectory linking is not successful the first time. Often, trajectories are fragmented, in which case they can be manually linked up, or otherwise treated as separate trajectories. In this work, manual linking was usually only performed in trajectories of

special interest, such as adsorption and desorption events.

If there are undesired particles in the image, such as aggregates or contaminants, but particle tracking is still desired (for example while developing the interface preparation protocol and the program, which was done in parallel), it is possible to selectively remove trajectories based on the shape of the point spread function. Many contaminants, which were present while developing the interface preparation protocol, were removed via this mechanism. Contaminants usually have a larger and often anisotropic point spread function, as the particles are larger than gold particles that scatter at a similar intensity. In addition, contaminants sometimes do not adsorb to the interface, instead undergoing motion perpendicular to the interface, as observed by point spread functions that fluctuate strongly in width. Particles that move too close to each other are also eliminated in this way, as point spread functions are distorted in the vicinity of other particles. For movies in which these issues arise, we included the option to remove trajectories in which the point spread function is significantly elongated in more than 40% of the frames at the end of the fitting algorithm. This was typically applied to movies where it was not an aim to track skimming gold particles or adsorption or desorption events. However, particles that move above the interface could contribute to the signal of adsorbed particles without

affecting the point spread function, and artefacts from this are not detected.

The completed array contains the fitting parameters for each particle and each frame.

3.2.3 Patterned noise from the camera

Another important measure of the quality of the data specific to particle tracking is the diffusive behaviour in terms of the time-averaged MSD (see Fig. 3.10). We found that the camera produces bands of increased noise in every other image (see the image in Fig. 3.5 for an example) or in all images, but with more consistency within odd and even frames, respectively, than across all frames. This noise pattern (alternating with odd and even frames) is expected to shift particle positions towards the bands with increased noise in every other image, leading to a zig-zag pattern in the MSD (see Fig. 3.10b). A simulation of noise bands in every other frame produced results that looked very similar to Fig. 3.10b (see Fig. 3.10a). Therefore, for most analysis purposes half of the frames in each movie were removed. Which half this was did not significantly affect the results. Movie files were inspected individually and the frames which appeared to have a more noticeable striped pattern were discarded.

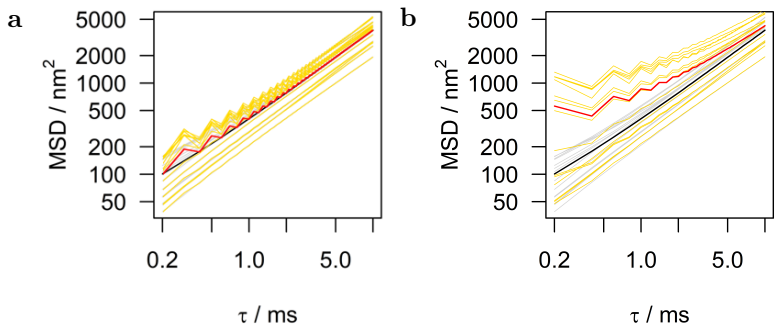


Figure 3.10: The effect of patterned noise in the image is removed by only considering odd frames in a movie of 20 nm gold particles imaged at 10 kHz. a) Time-averaged mean squared displacement (MSD) vs. time difference before (yellow, mean in red) removing half of all frames and after removing half of all frames (grey, mean in black). b) The same data after removing half of all frames (grey, mean in black) and a simulation (yellow, mean in red) in which particle positions were moved in every other frame. The number of pixels by which the y position of the particle was moved was inversely proportional to the trajectory-averaged amplitude, and ranged between 0.09 and 1.6.

The simulation only has half the number of frames as the original data, resulting in a different but qualitatively similar zig-zag pattern in the MSD. There is a significant variation in how strongly particles are affected by the noise, but it is present in virtually all trajectories. The particles most strongly affected by this noise are likely to be those with the lowest scattering amplitudes, as the displacement of the fitted position by the noise band will be larger in these cases.

4 High-speed dynamics of single nanoparticles at oil-water interfaces

The work described in this chapter was performed by me.

This chapter explores the size dependence and the effect of an added surfactant on the in-plane dynamics of gold nanoparticles observed with a TIR-DF microscope. Section 4.1 describes the experiments and outlines the expected results from the literature and from this work, and section 4.2 presents the results. Section 4.3 summarises and discusses the findings in this chapter.

4.1 Method and expected results

Water-on-oil interfaces with (DDM) and without surfactant (MQ) were prepared with particles of sizes (diameter) 20, 40 and 80 nm as described in section 2.2.3. The experimental observables are defined in section 3.1.

The diffusion coefficient is expected to decrease with the particle size as $D \sim 1/R_\mathrm{h}$ according to the Stokes-Einstein equation (4). Deviations from this can occur for various reasons (see section 1.2.2), including if particles within

an ensemble have different contact angles. Smaller contact angles (more immersion in the more viscous oil phase) should lead to slower diffusion, and larger contact angles to faster diffusion, as the drag force experienced by the particle varies with the contact angle. Out-of-plane motion can also lead to slower in-plane diffusion than what would be expected in a two-dimensional model, but could also result in brief flights through the less viscous water phase [94], leading to effectively faster (Brownian but not Gaussian) motion.

The data set used for this chapter and chapter 5 is presented in Tab. 3. Less data was obtained for some sample types because of low rates of adsorption to the interface.

Table 3: Overview of the dataset used for ensemble analyses. The number indicates the particle diameter in nm; MQ and DDM refer to the interface type (without and with added surfactant, respectively). Trajectories shorter than 1000 frames are not included.

Group	Interfaces	Trajectories	Data points	Sampling rates / kHz
20 MQ	5	416	4 678 579	2.5, 5, 12.5
DDM	4	641	5 452 645	2.5, 5, 12.5
40 MQ	5	652	10 646 135	2.5, 5, 12.5, 25, 50
DDM	3	208	1 903 460	2.5, 5, 12.5, 25
80 MQ	5	271	4 778 569	2.5, 5, 12.5, 25, 50
DDM	1	43	897 555	5, 12.5

4.2 Results

This section compares representative or ensemble-aggregated data for each set of particle size and interface type. The behaviour of representative trajectories is discussed in section 4.2.1, followed by ensemble-aggregated diffusive and scattering behaviour in sections 4.2.2 and 4.2.3, respectively. Section 4.2.4 discusses the correlation between these two properties. Section 4.2.5 explores the deviation from the expected Gaussianity and the assumption that particles are identical, and section 4.2.6 investigates deviations from Brownian motion in what appears to be confinement of some particle types.

4.2.1 Representative trajectories

Representative trajectories of 20, 40 and 80 nm particles at the two interface types are compared in Fig. 4.1, giving a visual impression of how particles from different sample types diffuse differently.

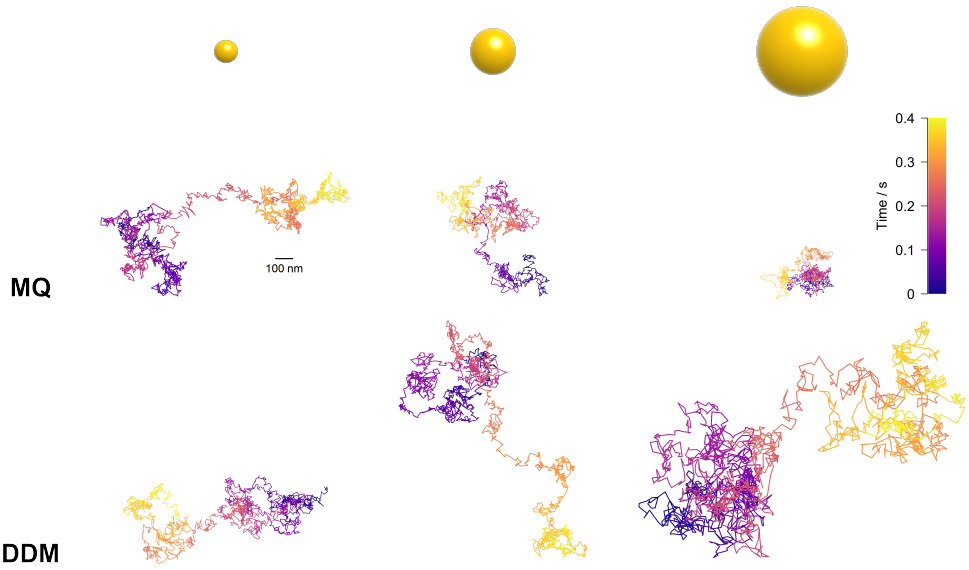


Figure 4.1: In-plane trajectories of particles with diameters of 20, 40 and 80 nm at surfactant-free (MQ) and DDM-laden interfaces (DDM): 2000 frames for each trajectory at 5 kHz. The scale bar in the first image applies to all trajectories in this figure. The diffusion coefficient of each trajectory section is typical of its interface type and particle size.

At MQ interfaces, the diffusion visibly slows down with particle size; at DDM interfaces, this trend is reversed, with 20 and 40 nm particles diffusing at a similar speed and 80 nm particles diffusing significantly faster. When comparing the 80 nm DDM trajectory to the 20 nm MQ or 40 nm DDM trajectories, it is also noteworthy that while the spatial extent covered is only slightly larger for the 80 nm DDM trajectory, the path length appears significantly larger. This small ratio of path length to spatial extent covered is a sign of subdiffusion (see section 3.1.2 for the definition).

Another notable observable is the scattering intensity. The time traces of the scattering intensity and instantaneous diffusion coefficient of the particles from Fig. 4.1 at MQ and DDM interfaces are shown in Fig.s 4.2 and 4.3, respectively.

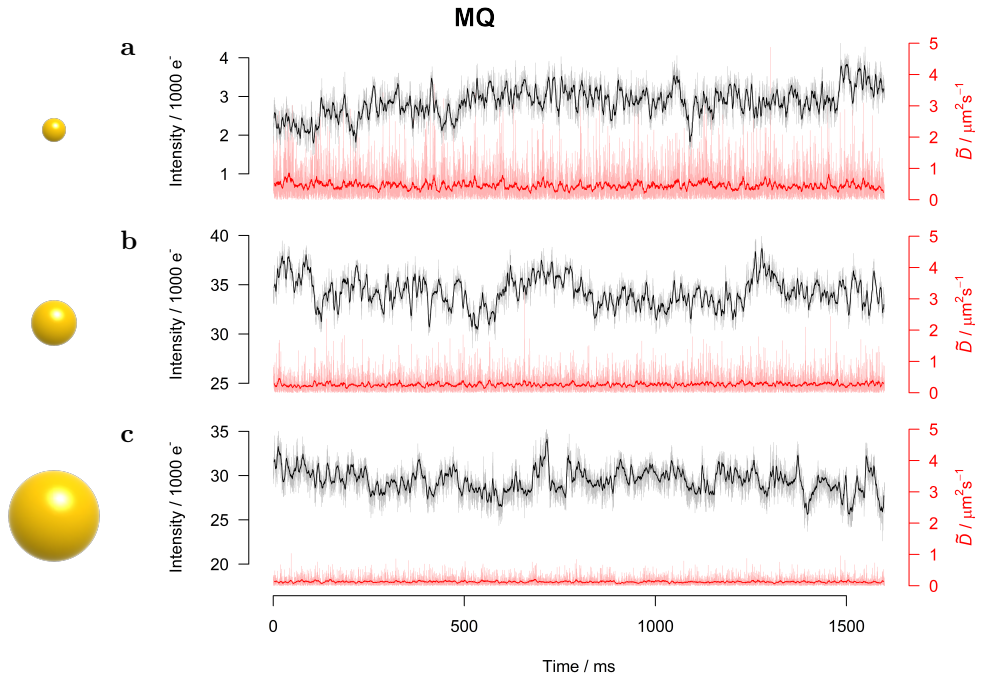


Figure 4.2: Intensity (black) and instantaneous diffusion coefficient (red) traces of 20, 40 and 80 nm particles at MQ interfaces; all at 5 kHz. Dark lines represent laterally averaged data; fainter lines represent the raw data. The scale for the instantaneous diffusion coefficient is the same for all three. Intensities are not directly comparable as the laser power density should be taken into account for this. The trajectories are the ones shown in Fig. 4.1, but include 8000 frames instead of 2000.

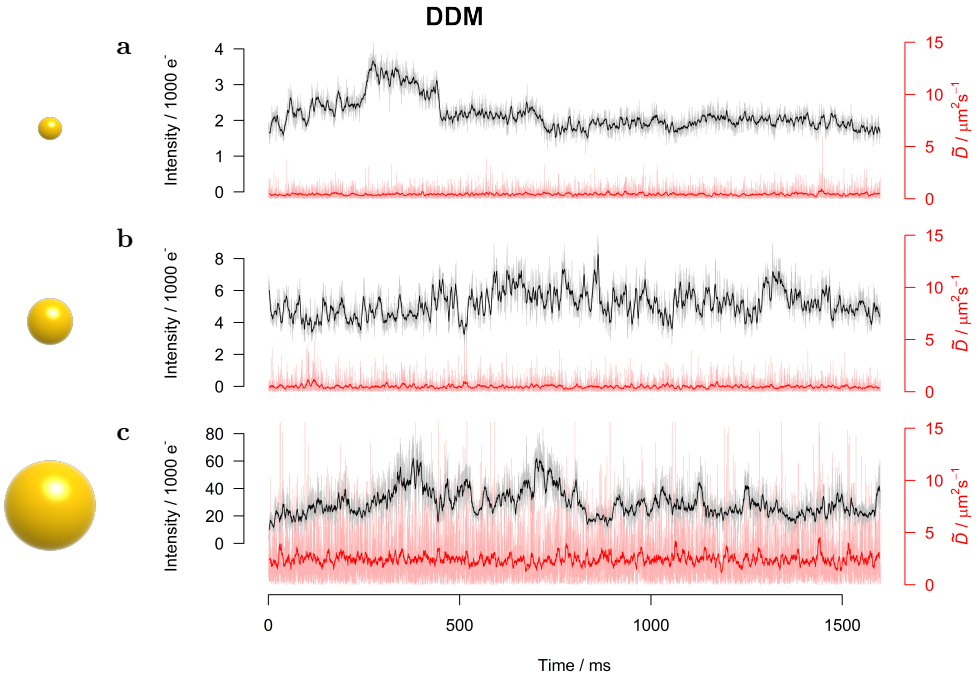


Figure 4.3: Intensity and instantaneous diffusion coefficient traces of 20, 40 and 80 nm particles at DDM interfaces; all at 5 kHz (compare to Fig. 4.2).

As was evident from the visualised in-plane trajectories (Fig. 4.1), the diffusion slows down as the particle size increases at MQ interfaces (Fig. 4.2) and is higher for larger particles at DDM interfaces (Fig. 4.3).

4.2.2 Ensemble diffusion analysis

The diffusion coefficient for each trajectory is expected to be related to the particle size R_h and contact angle θ via $D = a/(R_\mathrm{h}(b + c\cos\theta))$, where a,

b and c are constants (see Eqn. (4)). Fig. 4.4 shows distributions of the diffusion coefficient with and without size scaling for the data set in Tab. 3, with some anomalously slow trajectories removed (see below).

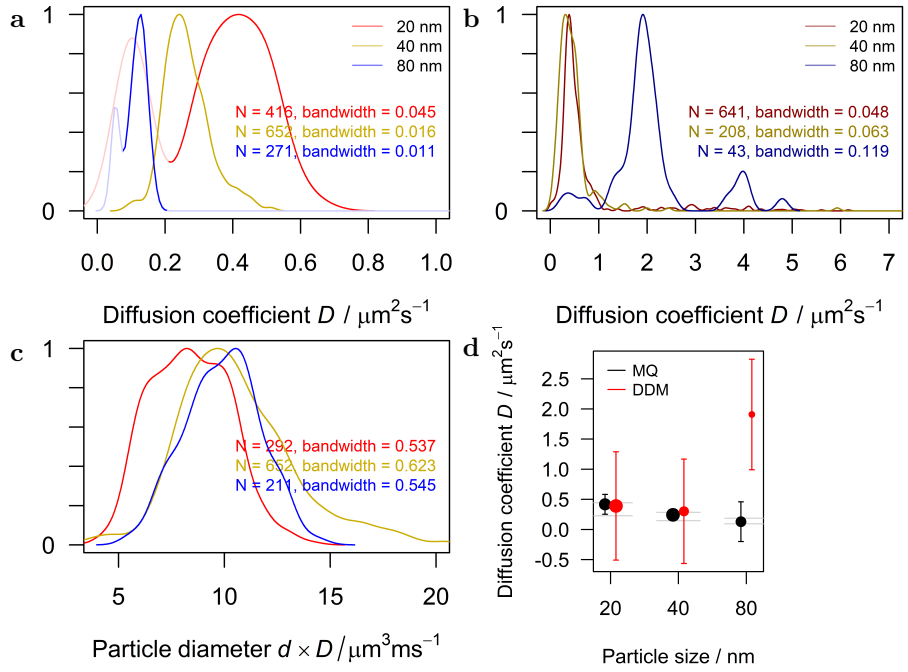


Figure 4.4: Diffusion coefficients of the trajectories detailed in Tab. 3. a)-b) Distributions at surfactant-free (MQ, a) and surfactant-laden (DDM, b) interfaces. Trajectories not used in c) are fainter. c) Distribution of size-scaled diffusion coefficients at MQ interfaces, with shoulders and outliers removed in the 20 and 80 nm distributions from a). d) Diffusion coefficient distribution maxima and standard deviations within each particle size and interface type. The size of the points in the graph a scales with the number of trajectories n as $a \propto n^{0.3}$. Grey lines represent diffusion coefficient values corresponding to theoretical contact angles of 0 (fully immersed in the oil) and 90°, respectively. The numbers given here assume the Stokes radius provided by the manufacturer (see section 2.2.3).

The distributions of 20 and 80 nm particles at MQ interfaces have visible shoulders at lower diffusion coefficients (see Fig. 4.5). Given the sharp divisions, this could be due to aggregation or contamination.

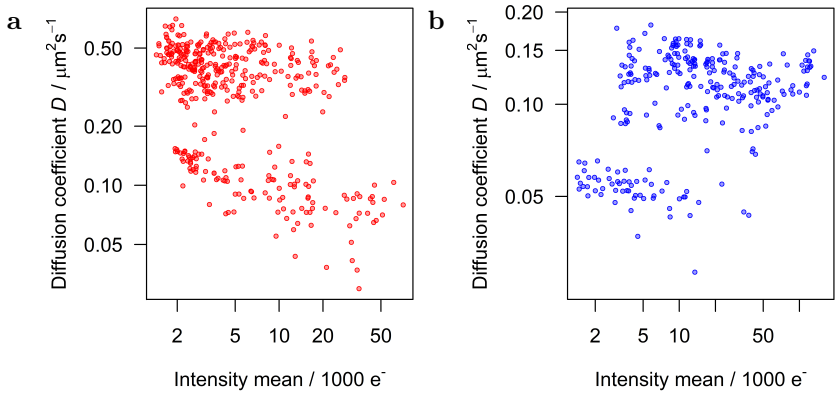


Figure 4.5: Diffusion coefficient vs. trajectory-averaged intensity for a) 20 nm particles and b) 80 nm particles at MQ interfaces. The data set is the same as in Fig. 4.4.

At MQ interfaces, the diffusion coefficient roughly follows the expected size trend. The contact angles are unexpectedly small, as the particles are expected to be predominantly hydrophilic — contact angles below 90° (diffusion coefficients lower than the upper of the grey lines in Fig. 4.4d) are not expected for hydrophilic particles. This may be explained by an increased drag caused by fluctuations in the interface at the contact line via the fluctuation-dissipation theorem [48], suggesting that the real contact angles are larger than what would be expected from the Stokes-Einstein

equation. Another possible reason for unexpectedly slow diffusion is out-of-plane motion, i.e. the measured diffusion coefficient does not include all the motion taking place. This will be explored in the following sections.

At DDM interfaces, the size-dependence of the diffusion coefficient for 20 and 40 nm particles can be qualitatively explained by the same arguments as at MQ interfaces, but surprisingly, 80 nm particles diffuse much faster than expected. The data set for this group is small, and it was difficult to produce interfaces of this type at which particles adsorbed to the interface and could be observed. This, in combination with the high diffusivity, suggests that larger particles experience a higher barrier to adsorption. Additionally, the large contact angle (equivalent to a large diffusion coefficient) and large variation within all size groups indicate one or both of a lower adsorption energy and kinetic barriers towards relaxation.

4.2.3 Scattering intensity

The scattering intensity scales both with the particle size ($I \propto d^6$, see Eqns. (6) and (8)) and with the immersion depth of the particle, with a lower scattering intensity intuitively expected for particles that are less immersed in the oil. A comparison of trajectory-averaged scattering intensity

values is shown in Fig. 4.6.

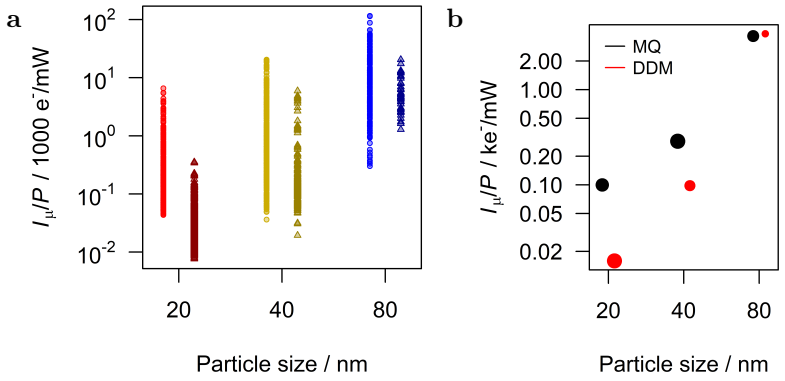


Figure 4.6: Laser power-adjusted scattering intensity. a) Trajectory-averaged data vs. sample type (MQ on the left and DDM on the right for each particle size). b) Maxima of the ensemble distributions.

Particles appear dimmer at DDM interfaces than at MQ interfaces, and the intensity increase with increasing particle size differs (Fig. 4.6b): The intensity gain factors for a doubling of the particle size vary widely at both types of interface, with larger factors for a change from 40 to 80 nm particles (39 and 13 for MQ and DDM interfaces, respectively) than for a change from 20 to 40 nm particles (3 and 6, respectively). A factor of 64 is expected for a purely size-dependent scaling. The consistently lower factors are likely due to experimental issues: Less bright 20 nm particles are difficult to track and therefore likely to be omitted from this aggregated data, and the 80 nm data may include saturated particles.

The lower intensity for particles at DDM interfaces suggests a more shallow immersion at the interface, which is expected to lead to a higher diffusion coefficient. Since the diffusion data (25% faster for 40 and 7% slower for 20 nm particles, respectively) does not explain the lower intensity, there are likely to be other factors at play in either the intensity or the diffusive behaviour: Altered interfacial rheology (higher effective viscosity) and out-of-plane motion (removing a part of the thermal motion into an unobserved dimension) could both lower the observed diffusion coefficient. Alternatively, increased interfacial roughness or similar factors related to the particle position within the interface (for example orientation in terms of the PVP ligand) could alter the scattering behaviour of particles.

The relative fluctuations in the scattering intensity are an indication of the z motion particles undergo within the observation time (see e.g. Fig. 4.3), and are shown in Fig. 4.7.

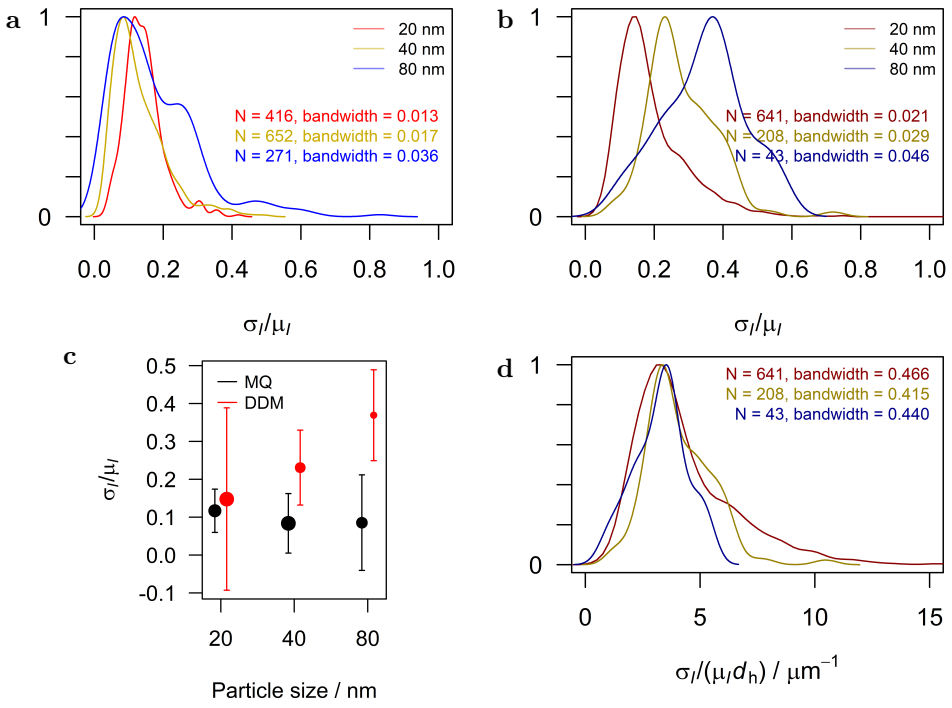


Figure 4.7: Comparison of fluctuations in scattering intensity between different samples. Standard deviation over a trajectory σ_I relative to trajectory mean μ_I, a) at MQ interfaces and b) at DDM interfaces. c) Ensemble values (distribution maxima) of σ_I/μ_I as a function of particle diameter at MQ (black) and DDM interfaces (red). d) σ_I/μ_I at DDM interfaces scaled with hydrodynamic radius d_h of the particle. The colours correspond to the ones in b).

At MQ interfaces, the relative intensity fluctuations are similar for different particle sizes. 20 nm particles undergo slightly larger fluctuations, suggesting that out-of-plane motion may indeed be responsible for the unexpectedly slow diffusion in this data set (Fig. 4.4a). At DDM interfaces, however, the fluctuations are significantly larger for larger particles, increasing approxi-

mately linearly with the hydrodynamic radius.

Thus, larger particles in DDM are not only unexpectedly fast in terms of their in-plane diffusion, but also in their out-of-plane motion.

4.2.4 Correlation between scattering intensity and diffusion

The correlation coefficient between the intensity and instantaneous diffusion coefficient over time is another possible indicator of motion perpendicular to the interface. Particles are expected to diffuse more slowly at smaller contact angles and, as the illumination intensity is higher (see section 2.1.2), have higher scattering intensities compared with larger contact angles. Immersion depth fluctuations on the experimental time scale therefore lead to anti-correlation between the instantaneous diffusion coefficient and the scattering intensity. The correlation data is shown in Fig. 4.8.

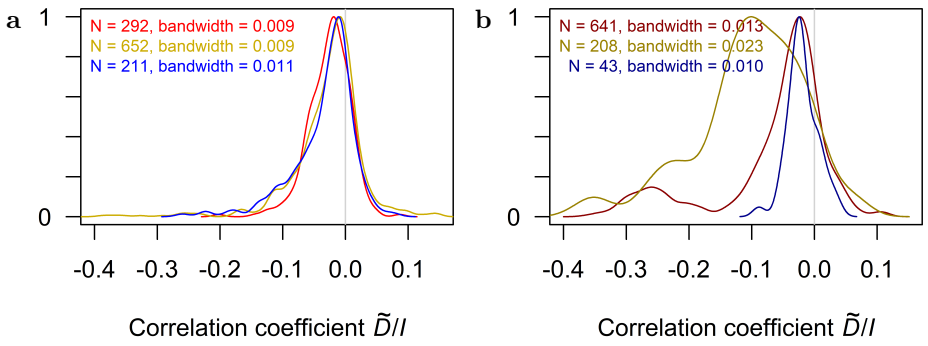


Figure 4.8: Correlation between intensity and instantaneous diffusion coefficients over the course of trajectories for the data in Tab. 3. a)-b) Distributions at surfactant-free (MQ, a) and surfactant-laden (DDM, b) interfaces. Colours correspond to particle sizes as in Fig. 4.4.

There is a small but clear negative correlation in all sample types. At MQ interfaces, all particle sizes behave very similarly. At DDM interfaces, overall there is a larger negative correlation, especially with 40 nm particles and a subgroup of 20 nm particles, indicating a higher mobility perpendicular to the interface, and the distributions are broader, suggesting more diversity within the sample types, in keeping with the findings above. Only 80 nm particles appear surprisingly stationary, suggesting qualitatively different behaviour from other sample types. However, the sample size for this group was much smaller than for the others, and it is likely that the anti-correlated behaviour is more prevalent in a subset of particles that is small relative to the ensemble and was therefore not observed here.

4.2.5 Displacement distributions

The in-plane step-size distribution can be an indicator of the occurrence of rare events such as brief flights through the less viscous phase or confinement due to periods of deeper immersion in the less viscous phase, with even very briefly faster diffusion giving rise to tails at large step sizes, and different immersion states expected to lead to a sum of several Gaussian distributions rather than the expected single Gaussian. This makes deviation from Gaussianity an additional indicator of out-of-plane motion within a trajectory. In addition, step sizes can be aggregated over an ensemble of trajectories, in which case non-Gaussianity can be a result of differences between the trajectories. These differences can arise from the limited observation time, or they can be inherent to the system. In the limit of long observation times, the non-Gaussianity can be attributed to either out-of-plane motion or inherent differences between particles (for example due to size, shape or history) by comparing quantitative measures of non-Gaussianity and non-ergodicity using the non-Gaussian parameter (NGP) and ergodicity-breaking parameter (EBP), defined in section 3.1.3.

The data was categorised into groups of the same particle size, interface

type and sampling rate, and the resulting shapes analysed as ensembles of trajectories within each group (Fig. 4.9).

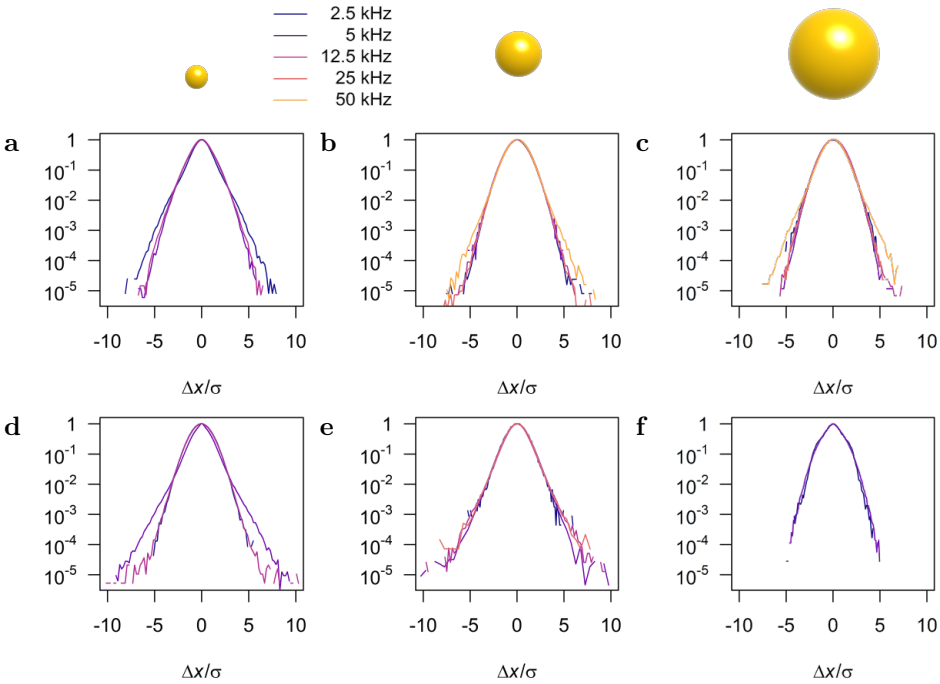


Figure 4.9: Step-size distributions for the size and interface groups in Tab. 3 as a function of the sampling rate. a-c) MQ interfaces, d-f) DDM interfaces; 20, 40 and 80 nm from left to right.

While many of the distributions in Fig. 4.9 appear approximately Gaussian, fitting reveals that the distribution is always better approximated by a central Gaussian and tails (see Fig. 1.7), sometimes with an intermediate region between the two and sometimes with outliers beyond the tails that appear to roughly follow a power-law distribution. At MQ interfaces, the shape of

the tail is most commonly best described by an exponential model (in cases where the tails are not very pronounced, exponential and Gaussian models appear similar). At DDM interfaces, many tails have a distinctive power-law shape, and the distribution for 80 nm particles (Fig. 4.9f) is clearly better described by multiple Gaussians than by exponential or power-law models.

The NGP is strongly affected by rare events involving anomalously large displacements (see section 3.1.3). The data is shown in Fig. 4.10.

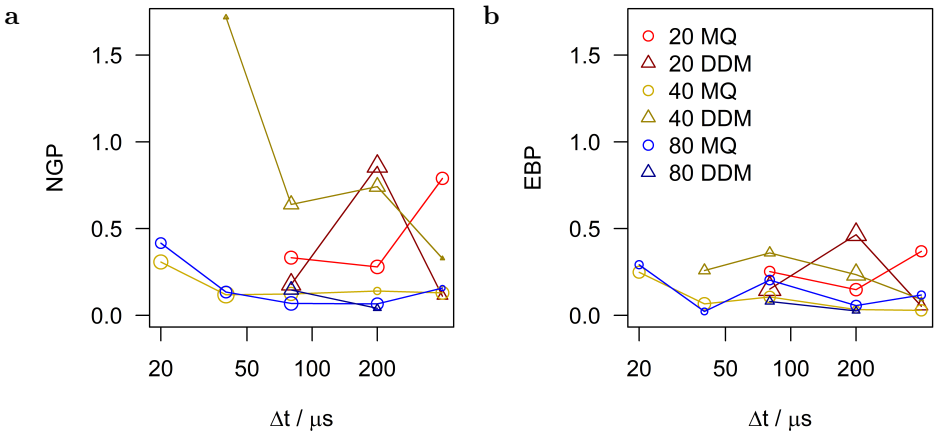


Figure 4.10: a) Non-Gaussian parameter (NGP) and b) ergodicity-breaking parameter (EBP) for all trajectories with a diffusion coefficient below 3 $\mu m^2 s^{-1}$. The point sizes in the graph are proportional to the logarithmic sample size.

While we do not have enough data for the number of rare events observed to be representative of the limit of large ensembles and sample sizes differ considerably (see Tab. 3), there are clear differences between the different

interface types, and to some extent particle sizes (see Fig. 4.10a). A comparison between NGP and EBP (see Fig. 4.10b) shows that ergodicity breaking is likely to be an important factor, as there is a strong correlation between the two (correlation coefficient 0.74). Fast trajectories were excluded to enable a more representative comparison between samples, as they often represent rare events.

20 and 40 nm particles at DDM interfaces have significantly larger NGP values at least for some sampling rates, as well as visibly larger tails in the displacement distributions. This is in keeping with the finding of increased out-of-plane motion in section 4.2.4, and additionally shows a higher heterogeneity between trajectories. With the 40 and 80 nm MQ step-size distributions, non-Gaussianity decreases with the time step. The 20 nm particles are believed to deviate from this rule because of the splitting of particles into two different diffusion groups (see Figs. 4.4a and 4.5). Higher-speed samples having higher NGP values with similar sample sizes could be a result of shorter effective observation times, giving particles less time to sample all their states.

We believe that in our experiments, the deviation from Gaussianity is an indicator of the out-of-plane motion. Information on the z position of the

particle and a higher quantity of data including out-of-plane motion (see chapter 5) might allow the characterisation of the interfacial properties that determine out-of-plane motion.

4.2.6 Confinement of larger particles

As mentioned in section 4.2.1, larger particles in DDM appear to sample a smaller interfacial area compared to the linear length of their trajectories. This behaviour can be quantified using the diffusion exponent α (subdiffusive motion results in $\alpha < 1$) and a smaller area sampled with a given duration and diffusion coefficient. The two quantities are shown in Fig. 4.11.

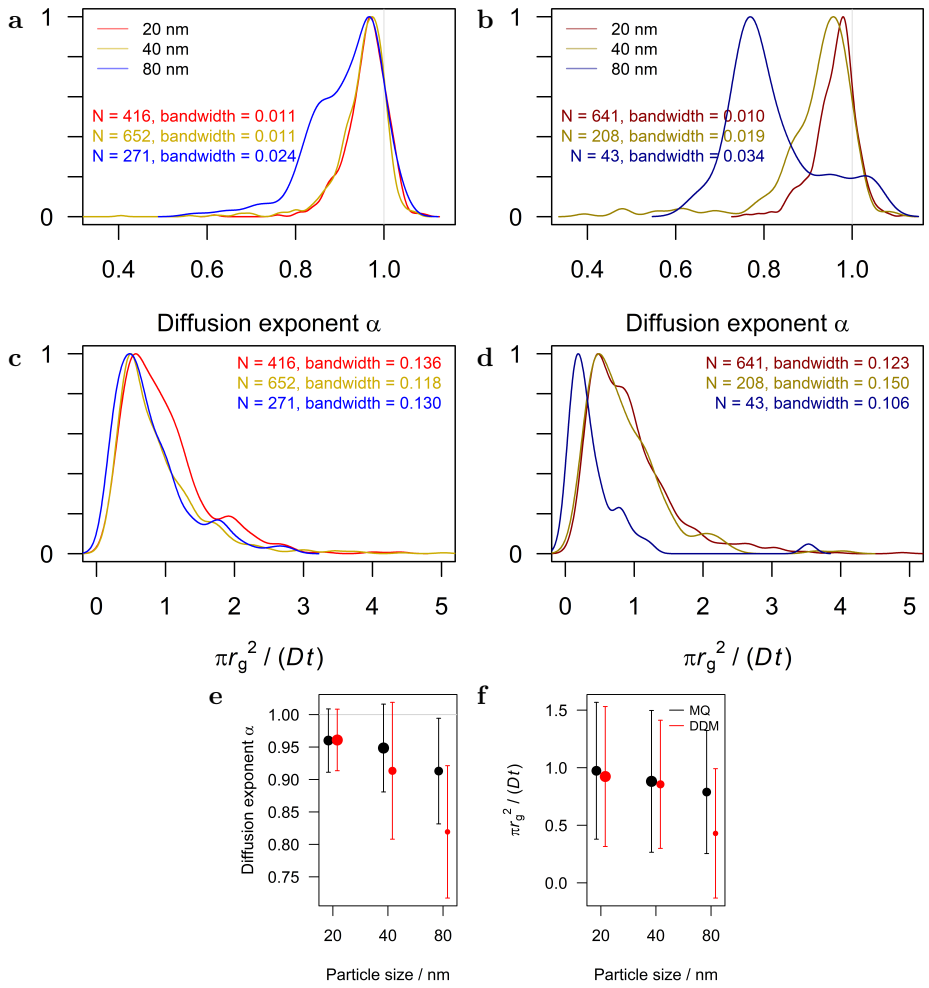


Figure 4.11: Visualising subdiffusive motion. a)-b) Distributions of α at MQ (a) and DDM (b) interfaces. c)-d) Distributions of area sampled (r_g is the radius of gyration) divided by diffusion coefficient and trajectory length in time, at MQ (c) and DDM (d) interfaces. e)-f) Mean values of the above quantities for each sample type.

All particles are somewhat subdiffusive (Figs. 4.11a, 4.11b and 4.11e), but 40 and 80 nm particles at DDM interfaces clearly more so than the others. With

the 80 nm particles at MQ interfaces, the mean is lowered by the shoulder in Fig. 4.11a, which corresponds to a group of low-diffusivity, low-intensity particles that may be contaminants (see section 4.2.2).

With the area given by the radius of gyration compared to the diffusive area (Figs. 4.11c, 4.11d and 4.11f), there is a gradual change between the particle sizes, with larger particles sampling smaller interfacial areas for a given diffusivity. 80 nm particles at DDM interfaces form an exception, with a sharp drop in the interfacial area sampled.

This clearly indicates confinement of 80 nm particles at DDM interfaces, and suggests that 40 nm particles at DDM interfaces are somewhat affected too. The confined behaviour coincides with differences in z motion as inferred from the changing variance in the intensity (section 4.2.3) and the increased NGP values (section 4.2.5), suggesting a link to increased out-of-plane motion. This is supported by a positive correlation between α and the relative intensity variance (see Fig. 4.12a).

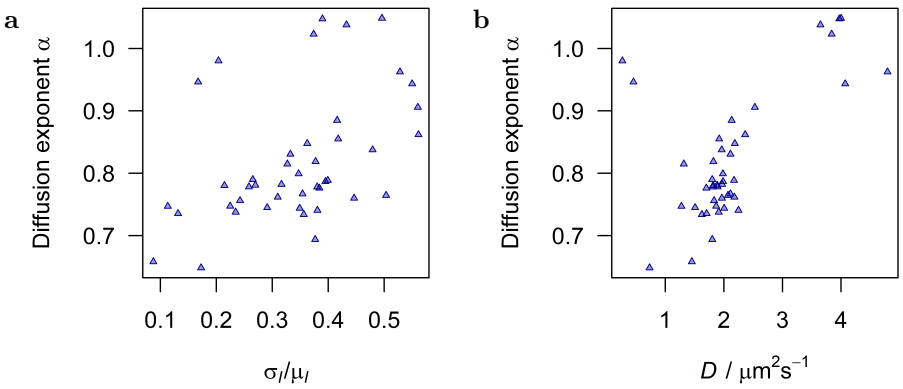


Figure 4.12: Properties associated with low α in 80 nm particles at ddm interfaces. Correlation between diffusion exponent and relative intensity variance (a) and between diffusion exponent and diffusion coefficient (b) for 80 nm particles at DDM interfaces. 97 trajectories; correlation coefficients 0.458 and 0.612, respectively.

In addition, low α values coincide with low diffusivities (Fig. 4.12b). This suggests that 80 nm particles at DDM interfaces are highly confined when in contact with the interface, while still undergoing fast diffusion because of their shallow immersion in the oil phase.

4.3 Summary and discussion

Particles at MQ interfaces diffuse more slowly than expected from the Stokes-Einstein equation for predominantly hydrophilic particles (possibly due to contact line fluctuations), but follow the predicted trend of decreased diffusivity with increased particle size. At DDM interfaces, on the other hand, 40

and 80 nm particles are, respectively, slightly and much faster than expected: The highest diffusivity was observed in 80 nm particles, and mutually similar values in 40 and 20 nm particles. Larger particles are also less likely to adsorb to DDM interfaces, and exhibit confined lateral motion when they do. Scattering analysis, correlation between diffusivity and scattering, and step-size distributions reveal that particles at DDM interfaces undergo more out-of-plane motion than at MQ interfaces, with scattering analysis suggesting that out-of-plane motion increases linearly with particle size.

The observations suggest that larger particles experience barriers to adsorption at DDM interfaces, possibly because of competition with surfactant molecules (see section 1.2.4). This would result in shallow immersion in the oil phase, and consequently faster diffusion, as well as the particle alternating between being drawn deeper into the oil phase and undergoing brief flights in more shallowly immersed states, explaining the observed increase in out-of-plane motion and altered form of the step-size distribution.

A possible reason for the unexpected rarity of adsorption events of larger particles to DDM interfaces is that the particles are less likely to fit into existing gaps in the surfactant layer (see Fig. 4.13), or, because of their lower curvature, displace enough surfactant molecules to accommodate them. The

competition for space also explains the increasing lateral confinement with particle size, as larger particles may face more resistance when moving laterally.

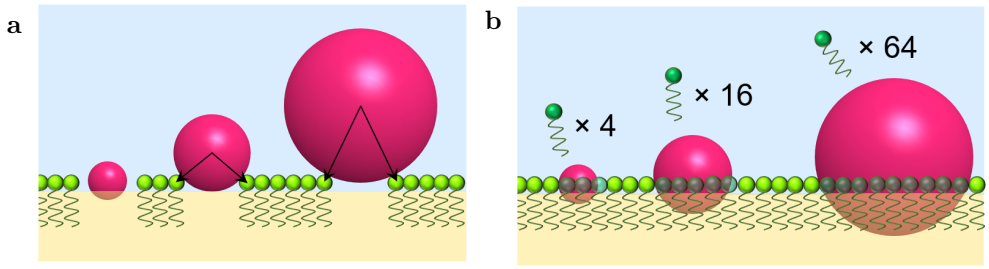


Figure 4.13: Illustrations of barriers to adsorption as proposed reasons for fewer observed particles and altered diffusive behaviour at DDM interfaces. a) 20, 40 and 80 nm particles approaching an identical gap in a monolayer of DDM molecules. The arrows indicate the direction of forces exerted by the particle on neighbouring surfactant molecules: They are less aligned with the interfacial plane for larger particles. b) Comparison of the number of surfactant molecules N that must be displaced for particle to adsorb with the same contact angle, analogous to an activation energy for the adsorption process. N was obtained from the image via $N = \pi R^2$, where R is the particle radius in surfactant diameters. Particles and surfactant molecules are not shown to scale; significantly more surfactant molecules are likely to be displaced.

5 Out-of-plane dynamics of nanoparticles at oil-water interfaces

All the work described in this chapter was performed by myself.

As outlined in section 1.2.2, understanding the mechanism of the adsorption and, if applicable, desorption processes of nanoparticles to liquid-liquid interfaces is important in understanding the dynamics of interfacial self-assembly: The out-of-plane dynamics affect lateral diffusion and inter-particle interactions, as well as the time scales at which different particles adsorb.

Adsorption and desorption events give an indication of the potential energy surface of the process. If desorption is observed at all, this indicates a small interfacial stabilisation energy (see section 1.2.1); on the order of a few $k_{\mathrm{B}}T$. If adsorption occurs quickly and irreversibly, this indicates a favourable adsorbed state with no significant kinetic barriers. If the adsorbed state is thermodynamically favoured but particles nonetheless often have encounters with the interface that do not lead to adsorption, this indicates kinetic barriers or local energy minima that do not coincide with a state in which the particle breaches the interface.

Kinetic barriers to adsorption have been observed in the past, occuring due to inter-particle interactions at relatively high particle concentrations [95], with adsorbed particles hindering the adsorption of non-adsorbed ones, as well as due to electrostatic interactions between the particle and the interface [49]. The experimental method used here cannot directly distinguish between breaching and non-breachingly bound particles, but different metastable immersion states can be inferred from lateral diffusive behaviour, as has been shown in the literature [44] and will be shown in this chapter.

Here, we study the apparently irreversible adsorption of nanoparticles to surfactant-free oil-water interfaces, brief encounters between particles and interfaces that do not lead to adsorption, and the adsorption and desorption dynamics of particles at interfaces with a surfactant added to the aqueous phase, using high-speed (down to 20 μs, or 50 kHz) and high-precision (nm) TIR-DF. To the best of our knowledge, this is the first time that the out-of-plane motion of nanoparticles at a liquid-liquid interface is observed for individual particles at high time resolution. This enables the characterisation of these events at a time resolution three orders of magnitude faster than previously possible [44], enabling a more detailed analysis of the process. Furthermore, we characterise intermediate states between the fully adsorbed and fully desorbed states that are common at surfactant-laden

interfaces but have not previously been described.

Section 5.1 briefly outlines the experiment and expected results. Section 5.2 describes how different immersion states and transition events between them are quantified. Observations of out-of-plane dynamics and other atypical diffusive states are presented in section 5.3, and the main results and conclusions are summarised in section 5.4.

5.1 Method and expected results

Adsorption and desorption events and brief contacts with the interface of gold particles of diameters 20, 40 and 80 nm were imaged at two types of interface; between oil and pure Milli-Q water (MQ interfaces) and between oil and a solution of the surfactant DDM in Milli-Q water (DDM interfaces). More details can be found in chapter 2; the experimental observables are defined in section 3.1.

Both the scattering intensity and the diffusive behaviour are expected to vary with the immersion depth and are therefore expected to change during transitions between different states. The lower phase, oil, is more viscous than the aquous phase by a factor of 50, leading particles to slow down

when they adsorb to the interface from the aqueous phase; more so the more deeply they are immersed in the oil phase. The scattering amplitude and intensity are expected to increase as the proportion of the particle in the oil phase increases as a result of more illumination photons reaching the particle in lower positions at the interface (see Fig. 2.10 and Eqn. (11)). Consequently, if the particle moves upwards within the interface, the diffusion will become faster and the intensity will decrease, and vice versa. This leads to an anti-correlation between scattering intensity and instantaneous diffusion coefficient.

Fluctuations in properties are likely to be smaller for particles in the fully adsorbed state than in more loosely bound states or in the bulk phase, as the fully adsorbed state has a well-defined immersion depth and therefore range of scattering intensity and instantaneous diffusion coefficient. At equilibrium, the particle — presumed to be hydrophilic — is expected to be more immersed in the water phase than in the oil phase. In a more loosely bound state, the proportion of the particle that is immersed in water is even higher, and the immersion depth and therefore the three-phase contact angle is more likely to fluctuate as the particle explores different metastable states or simply transitions from the bulk phase to the interface. The anti-correlation between the instantaneous diffusion coefficient and the intensity is expected

to be stronger for states that are farther from equilibrium. In addition, the shape of the step size distribution is expected to change during transitions between immersion states: When there is a change in the lateral diffusive dynamics, a Gaussian distribution, typical for Brownian motion, is expected to be replaced with a superposition of two or more Gaussian distributions with different widths. A combination of several distributions deviates from the typical Gaussian shape, which can be quantified with the non-Gaussian parameter (NGP).

5.2 Identification of partially adsorbed states and transitions between states

In chapter 4, the motion of particles described was largely confined to the horizontal plane. Here, we consider this the fully adsorbed state, and attempt to define more loosely bound states and events in which the degree of adsorption changes in relation to this. The different states are schematically illustrated in Fig. 5.1.

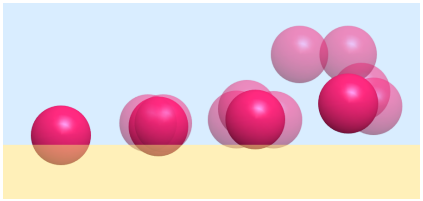


Figure 5.1: Schematic illustration of different immersion states of the particles at the oil-water interface. Left to right: Fully adsorbed, partially adsorbed, skimming, free. Due to the higher viscosity of the lower oil phase, particles are expected to diffuse faster when they are less immersed in the oil phase.

Automated detection of adsorption and desorption events is desirable; however, trajectories begin and end at times other than the beginning and end, respectively, of movies for reasons not related to such events. When the signal-to-noise ratio is poor, which was sometimes the case for the smallest particles, particles can gradually fade into a state in which they are trackable or out of it without an adsorption or desorption event occurring, disqualifying the most immediate strategy for automatic detection. Particles may also enter the field of view by diffusing into it from another part of the interface.

In addition to looking at the images, there are noticeable changes in the trajectory of the particle, as outlined in section 5.1. The fully adsorbed state of a particle of a given size at a given interface type is characterised by a diffusion coefficient in the horizontal plane, a scattering amplitude and a width of the point spread function in the image. In more loosely bound

states, they are expected to change. Some important differences between the two states are illustrated in Fig. 5.2.

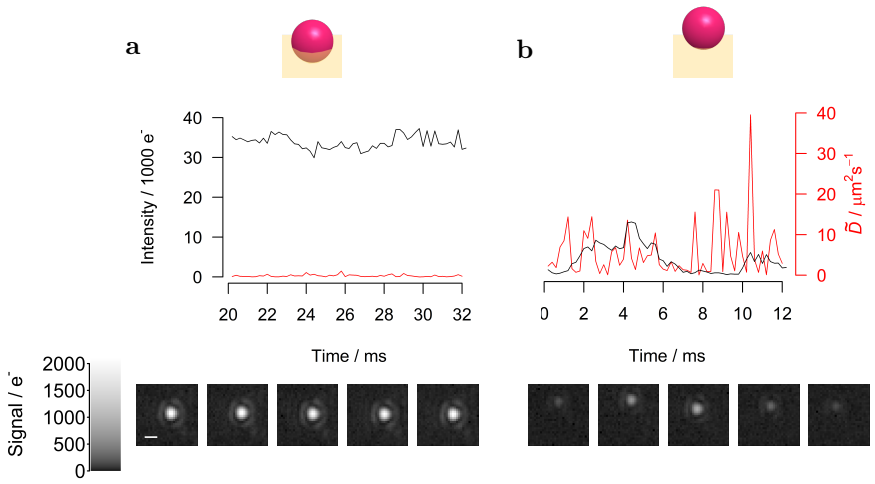


Figure 5.2: Intensity (black) and instantaneous diffusion coefficient (red) over 12 ms for a 40 nm gold particle at a MQ interface at a sampling rate of 5 kHz, with identical intensity and $\tilde{D}$ scales. a) Adsorbed state and b) a state in which the the particle is not fully adsorbed. Images of the same field of view with the same amplitude scaling are shown at intervals of 2 ms starting with the first frame of each trajectory segment; scale bar: 500 nm.

The transition is also evident in the correlation between the intensity and instantaneous diffusion coefficient and in the NGP. An adsorption event including these observables during the event are shown in Fig. 5.3.

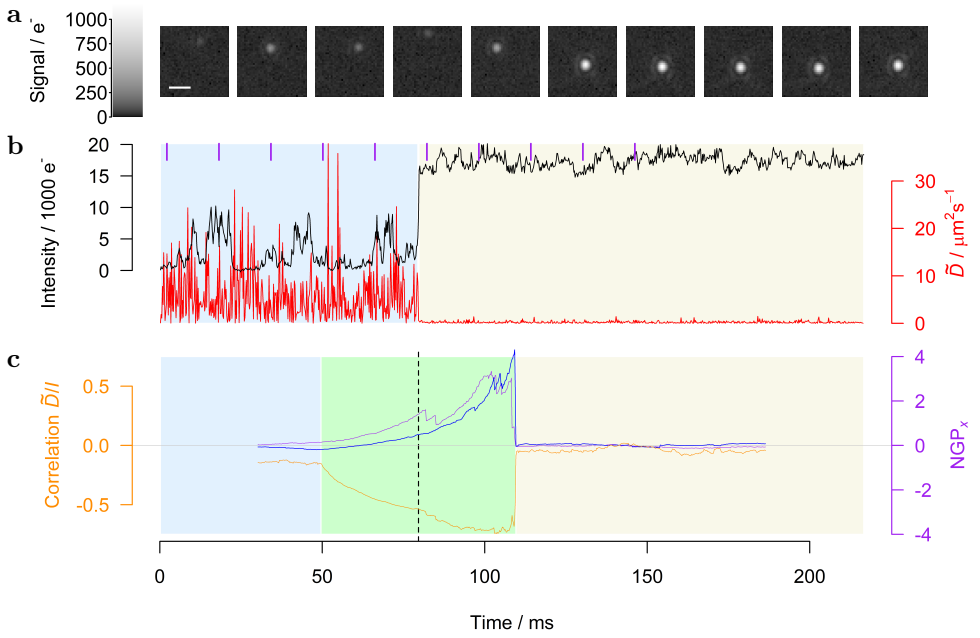


Figure 5.3: Adsorption of a 40 nm gold particle to a MQ interface sampled at 5 kHz. a) Sequence of images with identical field of view and a spacing of 16 ms, with times marked with purple vertical lines at the top of b). Scale bar: 1 μm. b) Intensity (black) and instantaneous diffusion coefficient (red). c) Correlation coefficient between intensity and instantaneous diffusion coefficient (orange) and non-Gaussian parameter in x (purple) and in y (blue) using a sliding time interval of 60 ms for both properties.

The behaviour of the correlation coefficient between intensity and instantaneous diffusion coefficient can be divided into three regimes: In the skimming state (shaded in blue in Fig. 5.3), it is approximately constant until half the width of the time interval before the adsorption. In the time interval around the adsorption (shaded in green), there is a strongly anti-correlated region.

Finally, at times at which the time interval does not include the adsorption event anymore (shaded in off-yellow), the correlation coefficient becomes approximately constant again, with a value that is closer to zero than in the skimming state.

The intensity and instantaneous diffusion coefficient naturally have the highest anti-correlation around the adsorption event, and in the skimming state, more different immersion states, and therefore intensity and diffusion states, are expected, resulting in a higher anti-correlation than in the adsorbed state, where fluctuations are small. Similarly, the NGP value is expected to be slightly higher in the skimming state, where the particle is more likely to transition rapidly between different immersion states, close to zero in the adsorbed state and much larger around the transition.

The data shown here represents a clearly defined adsorption; other transitions between immersion states are not as sharp. In the following, the term *adsorption event* refers to a particle changing from being difficult to observe and not trackable with a Gaussian fit algorithm to being clearly visible and entering a regime in which diffusion is typical for particles that are observed at the interface. In an adsorption to the *fully adsorbed* state, they additionally do not desorb or become less strongly adsorbed during the ob-

servation time as defined using the same observables, and the intensity does not have strong fluctuations. A *partially adsorbed* or *loosely bound* state is characterised by faster lateral diffusion, often accompanied by a strongly fluctuating intensity, with the intensity typically lower than in the fully adsorbed state. *Loosely bound* refers to the faster-moving of these particles. Partially adsorbed particles were observed to adsorb to the interface and go on to become untrackable or disappear from the image. If a particle becomes unobservable for a sufficient period of time to make it uncertain whether a reappearing particle is the same one, it is considered to have left the interface in a reversal of the adsorption process. Such an event is referred to as a *desorption*. A *skim* is an interaction between a particle and an interface that does not include adsorbed states as defined above.

5.3 Results

Adsorptions occur very quickly and the window of observation in time and space is small compared to the interfacial area. The issue can be overcome by specifically saving only movies in which adsorptions occur; however, if movies are saved to study diffusion of particles at the interface (see chapter 4), saving takes a long time compared to how long the interface can be

filmed with the limits given by the memory of the camera, especially at high frame rates. Skims were often difficult to track, and these trajectories are underrepresented in chapter 4 as a result. Adsorption was often preceded by a skim.

At MQ interfaces, we exclusively observed fully adsorbed diffusion at the interface, rare adsorption events and usually very brief (up to about 100 ms) skims. At DDM interfaces, clear adsorptions of the kind observed at MQ interfaces were not recorded. Instead, particles appeared at the interface and appeared to enter a skimming state, which, however, often did not lead to either desorption or a full adsorption within the experimental time frame. Additionally, we observed desorptions and diffusive and scattering behaviours that indicate states between full adsorption and the superficial skims observed at MQ interfaces, as well as transitions between immersion states. The different states and events are characterised in this section.

Section 5.3.1 details adsorption events of 40 nm particles at MQ interfaces (the one recorded adsorption event of a 20 nm particle appeared qualitatively the same), with events in 40 and 20 nm particles at DDM interfaces included for comparison. Section 5.3.2 shows desorption events of 40 and 20 nm particles from DDM interfaces. Section 5.3.3 compares skims of different-sized

particles at the two interface types. Section 5.3.4 presents other partially adsorbed states at DDM interfaces, and section 5.3.5 transitions between states other than adsorption and desorption events.

5.3.1 Adsorptions

A sample of adsorption events at MQ interfaces is shown in Fig. 5.4.

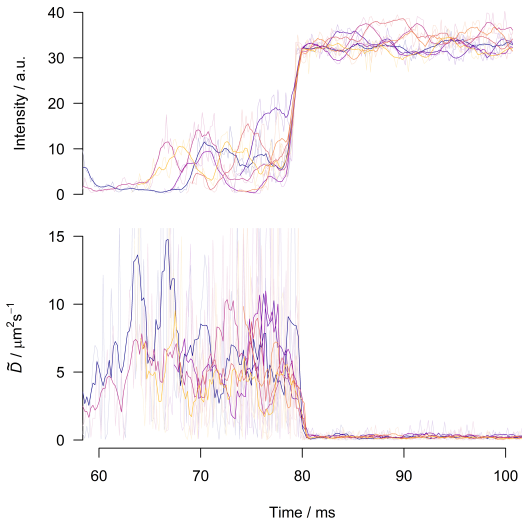


Figure 5.4: Intensity and instantaneous diffusion coefficient traces of seven different 40 nm gold particles, shown in different colours, during adsorption events at surfactant-free interfaces, sampled at 5 kHz. The thicker, darker lines correspond to smoothed values (see section 3.2.1); the thinner, fainter ones are the original data from the tracking algorithm. The trajectories are shifted in time and the intensities are scaled so that the first frame with an intensity within the adsorbed range and the intensity at this time are the same for all trajectories.

Adsorption events at MQ interfaces are usually very abrupt, with a sharply defined time of adsorption at this sampling rate: From one frame to the next, the particle reaches an intensity that is within the range of the adsorbed state, and the instantaneous diffusion coefficient drops starting from the same frame. No clear pattern is visible in the intensity or instantaneous diffusion coefficient immediately before or after the adsorption event (visible from the thin lines in Fig. 5.4).

The two trajectories for which there is a significant time interval during which the particle has not adsorbed but can be tracked appear to exhibit a pattern where the intensity increases and decreases, with the instantaneous diffusion coefficient having maxima where the intensity has minima. They are shown in Fig. 5.5.

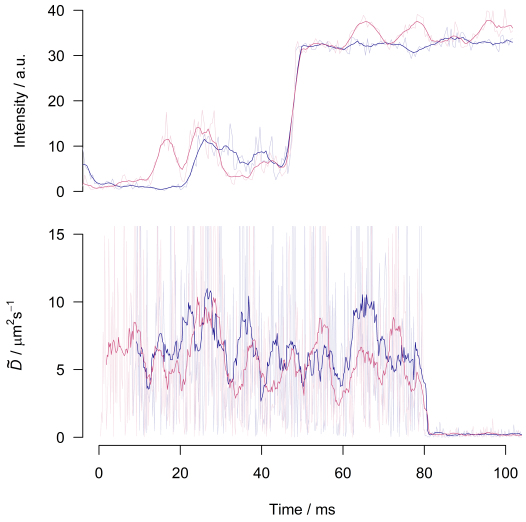


Figure 5.5: Intensity and instantaneous diffusion coefficient traces of 40 nm gold particles during adsorption events at surfactant-free interfaces: Two of the trajectories from Fig. 5.4.

This resembles observations of a hopping diffusion mechanism of particles at solid-liquid interfaces, where particles were found to leave the surface, diffuse in the bulk and readsorb. Several unproductive surface-encounters were typically required before a particle readsorbed to the surface [94]. The many encounters between particles and interfaces in this work that did not lead to adsorption (see also Figs. 5.10 and 5.11) are in agreement with the authors' and others' hypothesis that particles' interactions with the interface that do not, or not immediately, lead to adsorption affect the system.

The adsorption event is not resolved at this sampling rate. Adsorptions

at higher sampling rates were obtained and samples are contrasted with a trajectory from Fig. 5.4 in Fig. 5.6. Density distributions of sequential segments of the adsorbed sections of the trajectories (see Fig. 5.6) do not show a significant difference between the segments immediately after the adsorption and at later times either.

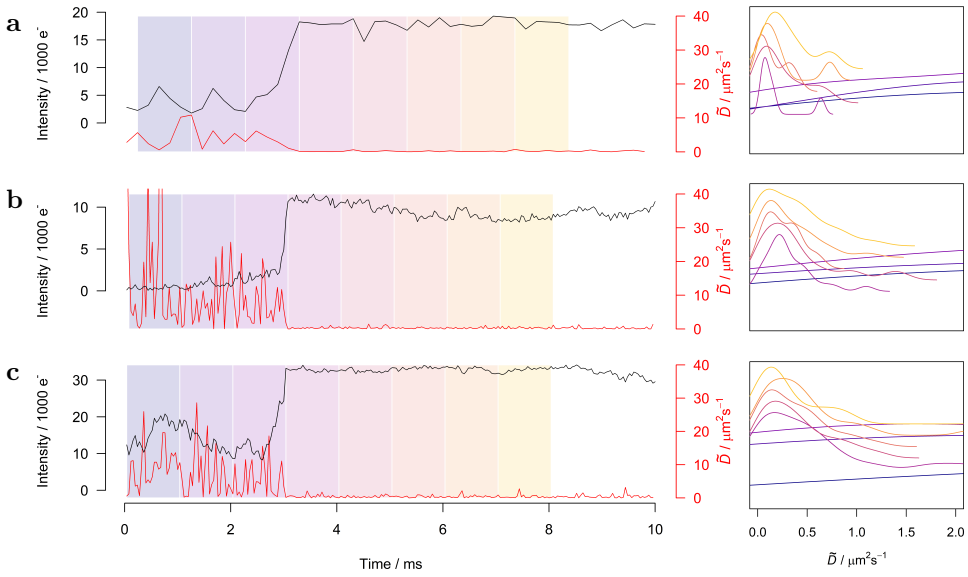


Figure 5.6: Adsorption of 40 nm nanoparticles to MQ interfaces at 25 kHz compared to a trajectory sampled at 5 kHz. a) 5 kHz; b)-c) 25 kHz. Intensity and instantaneous diffusion coefficient vs. time are shown on the left and density distributions of the instantaneous diffusion coefficient on the right, with each line corresponding to a shaded interval of 1 ms in the time trace. The diffusion coefficients after the adsorption events are 0.22, 0.12 and 0.18 $\mu m^2 s^{-1}$, respectively. The noticeably slower diffusion in the 5 kHz trajectory compared to the 25 kHz trajectories is only present in some of the 5 kHz trajectories.

Despite the five-fold increase in resolution, the adsorption event remains

instantaneous or near-instantaneous: Detailed analysis shows that at both sampling rates, the instantaneous diffusion coefficient reaches the level that is typical for the adsorbed state immediately upon reaching the adsorbed-state intensity or slightly earlier, i.e., for a frame index t at which the intensity reaches the adsorbed-state intensity, the instantaneous diffusion coefficient reaches or has reached the adsorbed-state value. Reaching this value earlier does not necessarily indicate that the motion of the particle has changed earlier; the values for the adsorbed state also occur in more loosely bound states.

At DDM interfaces, adsorption events did not show this highly characteristic combination of a sudden increase in intensity and decrease in diffusivity, instead maintaining a high diffusivity or undergoing fluctuations in it. Selected adsorption events at DDM interfaces are contrasted with an adsorption to a MQ interface in Fig. 5.7.

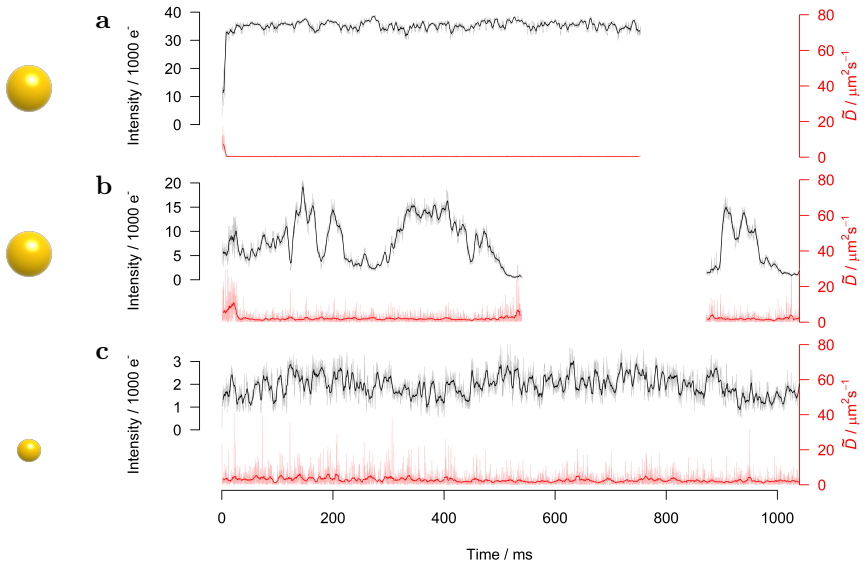


Figure 5.7: Adsorptions at MQ vs. at DDM interfaces, with the instantaneous diffusion coefficient shown to scale for the three trajectories. a) MQ, 40 nm, b) DDM, 40 nm, c) DDM, 20 nm. All sampled at 5 kHz (MQ particle averaged down).

Whereas the adsorption to the MQ interface is instantaneous and the particle immediately reaches a diffusive state that is typical of the fully adsorbed state, the adsorptions to DDM interfaces appear less complete: The 40 nm particle desorbs from the interface enough to not be trackable anymore before returning, and both it and the 20 nm particle retain diffusive behaviours that resemble the state immediately before adsorption in MQ for the typical duration of the observation time.

5.3.2 Desorptions

Desorption events from the fully adsorbed state were not observed at MQ interfaces. At DDM interfaces, the dynamics varied greatly with the particle size. In 20 nm particles, desorptions appeared to be common under certain conditions. At two of the interfaces prepared, skims and desorptions were common, at the other one that was stable for more than 30 minutes, they were not observed. Many of the desorptions occured from loosely bound states; however, desorptions from fully adsorbed states occurred as well. For 40 nm particles, the few observed desorptions resemble a reversal of the adsorptions at MQ interfaces (see Fig. 5.4). Typically, an abrupt transition from the adsorbed state to a very loosely attached state is rapidly followed by the disappearance of the particle from the observable part of the sample. In 80 nm particles, no desorptions were observed other than during skims, but this could be the result of a small sample size due to a low rate of more than superficial adsorption of 80 nm particles to DDM interfaces.

No desorption could be verified to be complete: Especially with the 40 nm particles, despite a clear transition to a more loosely bound regime, skims were always observed in the vicinity after the particle had supposedly des-

orbed, indicating that a particle is likely to remain nearby and interact with the interface even when it can no longer be observed with our method.

Examples of clear desorptions of 40 nm particles are shown in Fig. 5.8.

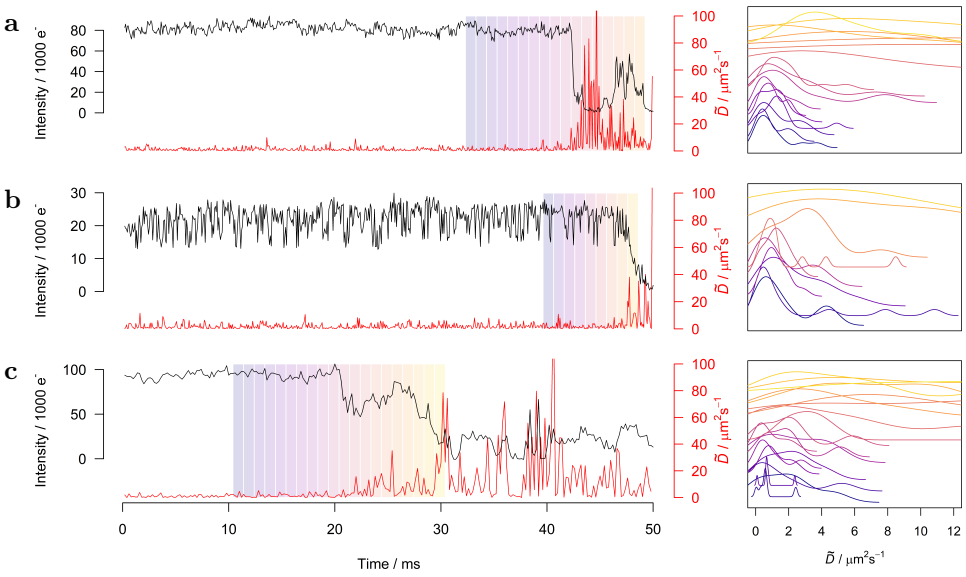


Figure 5.8: Desorption of 40 nm particles from DDM interfaces. a)-b) 12.5 kHz, c) 5 kHz. Density distributions of the instantaneous diffusion coefficient of the shaded 1 ms intervals in the time trace.

From the time traces in Fig. 5.8, it is visible that the desorption events of 40 nm particles at DDM interfaces are considerably more gradual than the adsorptions to MQ interfaces shown in section 5.3.1. In Figs. 5.8a and 5.8b, the time at which the intensity drops and the instantaneous diffusion coefficient increases can only be defined to within about 1 ms, and this

point is preceded by slightly increased diffusivity, which fluctuates on this time scale. The desorption in Fig. 5.8c appears to proceed in several steps, and within these steps, there are gradual changes.

The increase in diffusivity before the intensity drops is most evident in Fig. 5.8b, indicating that acceleration can likely take place before a change in immersion depth (see Fig. 5.9).

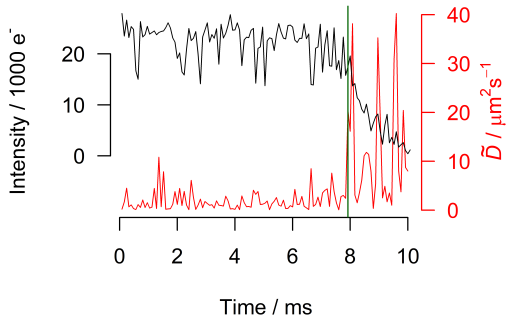


Figure 5.9: Detailed view of the final 10 ms of Fig. 5.8b. The first image with significantly increased diffusivity is marked with a vertical line. Note the high intensity at this point.

Desorptions of 20 nm particles from DDM interfaces were frequently observed, but none were as sharp as the 40 nm trajectories shown above, instead undergoing slow ($\approx$ 1 s) changes in diffusivity, and are therefore included in section 5.3.5 rather than here.

5.3.3 Skims

Skims are effectively unsuccessful adsorption events. They are likely to share many aspects of the early stage of the adsorption process and may give an indication of what determines whether an adsorption takes place, i.e. the presence and nature of kinetic barriers, as well as thermodynamic factors. High kinetic barriers in a thermodynamically favoured adsorption process are likely to result in long skims. Sustained deep skims without adsorption suggest kinetic barriers at deeper immersions, or a flat potential energy landscape. In the case of irreversible adsorption, skims can give an approximate measure of the lowest diffusivity (and thereby likely deepest immersion in the oil phase) a particle can exhibit before escape back into the water phase becomes impossible.

We originally believed that particles that only briefly appear in the field of view were not interacting with the interface, and therefore did not usually capture these events at MQ interfaces. At DDM interfaces, they were more common, and visibly slower; we therefore have more data on them.

Skims for each particle size at MQ interfaces are shown in Fig. 5.10 and at DDM interfaces in Fig. 5.11. The trajectories include both the beginning and

the end of the skim, i.e. the observation began before the appearance and ended after an extended disappearance of the particle, except in the case of the 20 nm particle at the DDM interface, for which fewer uninterrupted trajectories were obtained because of their low scattering intensity.

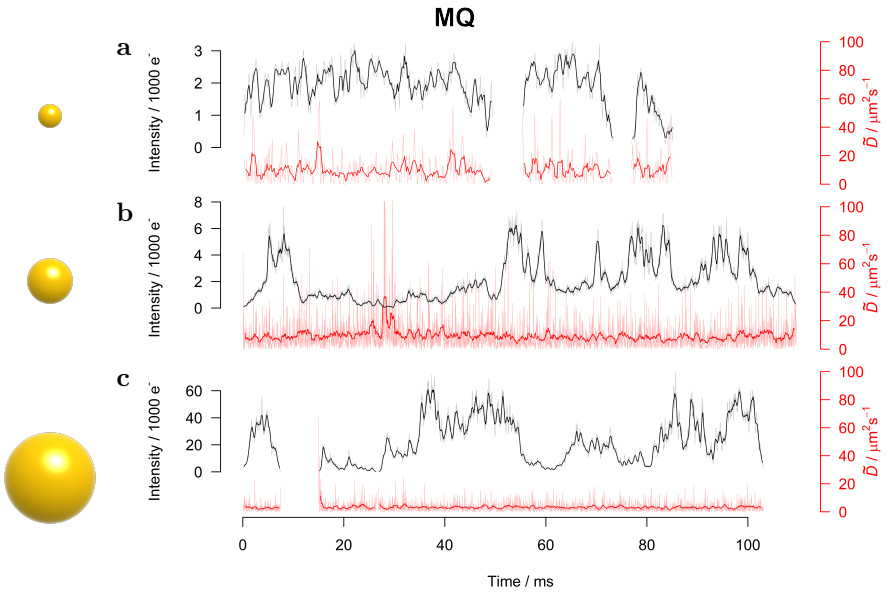


Figure 5.10: Skims of nanoparticles at MQ interfaces. a) 20 nm gold at 5 kHz, b) 40 nm gold at 25 kHz, c) 80 nm gold at 25 kHz.

The mean instantaneous diffusion coefficients for the 20 nm skim are 9.8, 10.1 and 11.2 $\mu m^2 s^{-1}$ for the 20 nm particle, 9.5 $\mu m^2 s^{-1}$ for the 40 nm particle and 3.0, 4.0 and 3.2 $\mu m^2 s^{-1}$ for the 80 nm particle. The theoretical diffusion coefficients in the water phase are 11.0, 7.0 and 4.6 $\mu m^2 s^{-1}$, respectively, using the hydrodynamic radius, and 24.1, 12.1 and 6.0 $\mu m^2 s^{-1}$, respectively,

using the particle diameter (see Eqn. (4)).

In the 20 nm trajectory, the intensity patterns reflect the different diffusivities, with the mean intensity decreasing as the diffusivity increases (2000, 2100 and 1100 e^-, respectively). The 40 nm particle appears to skim the interface at a certain height, with occasional deeper sampling. The 80 nm particle appears to spend more time at a lower position, judging by the intensity, in keeping with the finding of a lower diffusivity compared to the theoretical value for the water phase. The fact that the particle nevertheless leaves the interface suggests that 80 nm particles may have a larger kinetic barrier to adsorption, but more data is needed to confirm this.

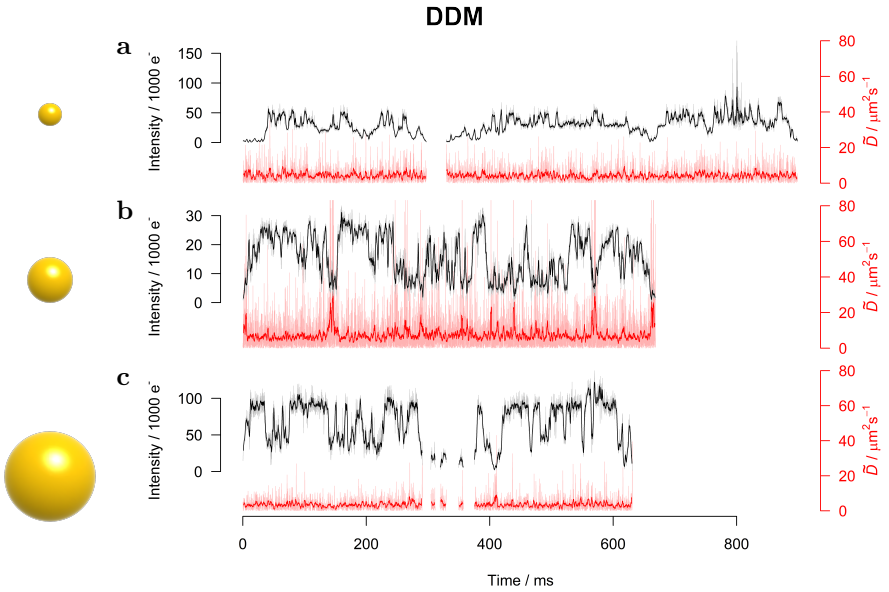


Figure 5.11: Skims of nanoparticles at DDM interfaces. a) 20 nm Au at 5 kHz. The intensity spikes near the end of the trajectory are not present in the amplitude, and are therefore likely to be a result of strong fluctuations in the shape of the point spread function. b) 40 nm gold at 12.5 kHz. c) 80 nm gold at 5 kHz. The 80 nm particle saturates the detector at the highest intensities.

Many skims at DDM interfaces are significantly longer than the ones observed at MQ interfaces. This is likely to be a result of more loosely bound states at DDM interfaces being energetically favourable enough to persist for longer observation times. At both interface types, 40 nm particles appear to be the fastest skimming particles. This is believed to be due to the difficulty of observing 20 nm particles at loosely bound states because of their lower scattering intensity, which means that the ones that are observed are likely

to be most deeply immersed in the interface.

The mean instantaneous diffusion coefficients for the 20 nm skim are 4.5 and 4.3 $\mu m^2 s^{-1}$ for the 20 nm particle, 7.7 $\mu m^2 s^{-1}$ for the 40 nm particle and 3.5, 4.2, 4.5, 3.6 and 3.6 $\mu m^2 s^{-1}$ for the 80 nm particle. The 20 nm particle is clearly slower than at the MQ interface, indicating deeper immersion. The 40 nm particle is also somewhat slower than at the MQ interface. It also has a higher relative intensity for a larger proportion of the trajectory, suggesting that it is partially adsorbed and occasionally moving farther away from the interface rather than skimming in the water and occasionally touching the interface. The 80 nm particle has similar diffusive behaviour as at the MQ interface. The intensity is difficult to assess due to saturation, but appears to resemble the 40 nm DDM particle more closely than the 80 nm MQ particle.

In summary, 20 and 40 nm particles at DDM interfaces appear to have deeper skims than their counterparts at MQ interfaces, and longer skims are observed at DDM interfaces for all particle sizes. At MQ interfaces, particles appear to be mostly surrounded by water and occasionally become more immsersed in the interface. At DDM interfaces, this behaviour is often replaced with one in which the particle is partially adsorbed, with z motion both towards the oil and towards the water.

5.3.4 Other partially adsorbed states

At DDM interfaces, trajectories were recorded that deviated from the fully adsorbed state (see section 4.2.1) but were different from the skims shown in section 5.3.3 both in terms of their diffusive and scattering behaviour and in that no adsorption or desorption events were included in the trajectory. Notably, there were many trajectories with increased diffusion compared to the fully adsorbed state, often accompanied by characteristic patterns in the intensity that varied considerably with the particle size. This was very prevalent in 80 nm particles, somewhat common in 20 nm particles and uncommon in 40 nm particles.

Fig. 5.12 shows representative trajectories of the three particle sizes in which characteristic intensity dips are visible.

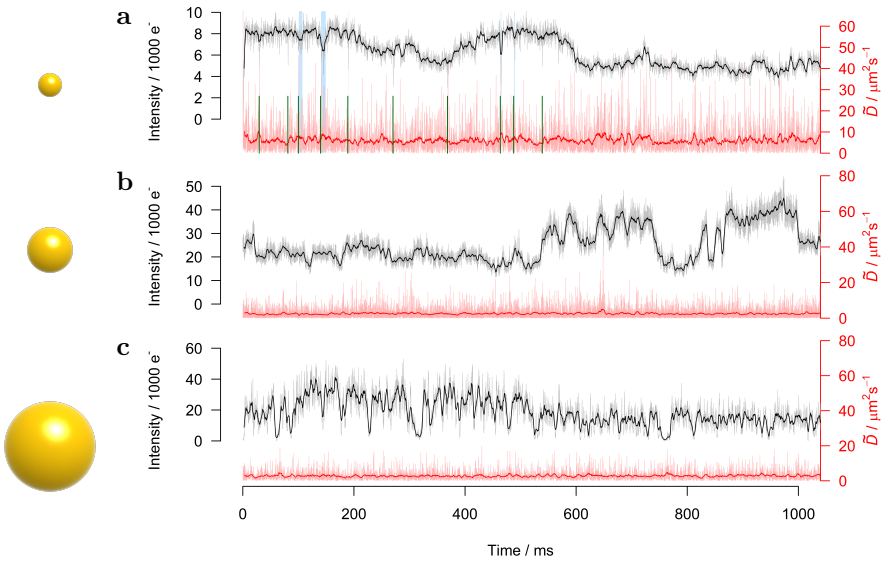


Figure 5.12: Representative intensity and instantaneous diffusion coefficient traces of particles at DDM interfaces in metastable immersion states. a) 20 nm particles, sampled at 5 kHz, b) 40 nm (12.5 kHz) and c) 80 nm (5 kHz). In the 20 nm trajectory, the intensity dips are shaded in blue and marked with a vertical line.

The intensity profile of loosely bound particles often shows sharp dips, and sometimes broader ones. With 20 nm particles, the majority of noticeable dips have a duration of up to approximately 3 ms, with the shortest ones that can be discerned at the given noise level lasting for approximately two frames (check) at 5 kHz, i.e. 0.4 ms. Longer-lasting dips (up to 24 ms) are more often accompanied by noticeable increases in instantaneous diffusion coefficient. The very brief intensity dips were not observed in 40 and 80 nm particles; instead, their intensity dips are usually broader and less well-

defined. Longer flights were observed in 20 nm particles too, but it was difficult to track these particles.

With 80 nm, trajectories with diffusion coefficients $D > 2\ \mu\mathrm{m}^2\mathrm{s}^{-1}$ have intensity dips, whereas trajectories with $D < 1.7\ \mu\mathrm{m}^2\mathrm{s}^{-1}$ do not (we did not observe trajectories with D between these values). Similarly, with 20 nm particles, the dips shown in Fig. 5.12 occurred in the fastest trajectories, with $D \gtrsim 5\ \mu\mathrm{m}^2\mathrm{s}^{-1}$, and slower intensity fluctuations were most pronounced in fast trajectories, but visible in very slow trajectories ($D \lesssim 0.2\ \mu\mathrm{m}^2\mathrm{s}^{-1}$). With 40 nm particles, faster particles' intensities were not more likely to have dips, perhaps suggesting a more stable loosely adsorbed state.

5.3.5 Transitions between immersion states

Besides the transitions between unobservable and partially adsorbed states that were often easy to identify by eye, at DDM interfaces we observed transitions between different diffusive states that did not involve adsorption or desorption. This was especially common in 20 nm particles. Examples are shown in Fig. 5.13.

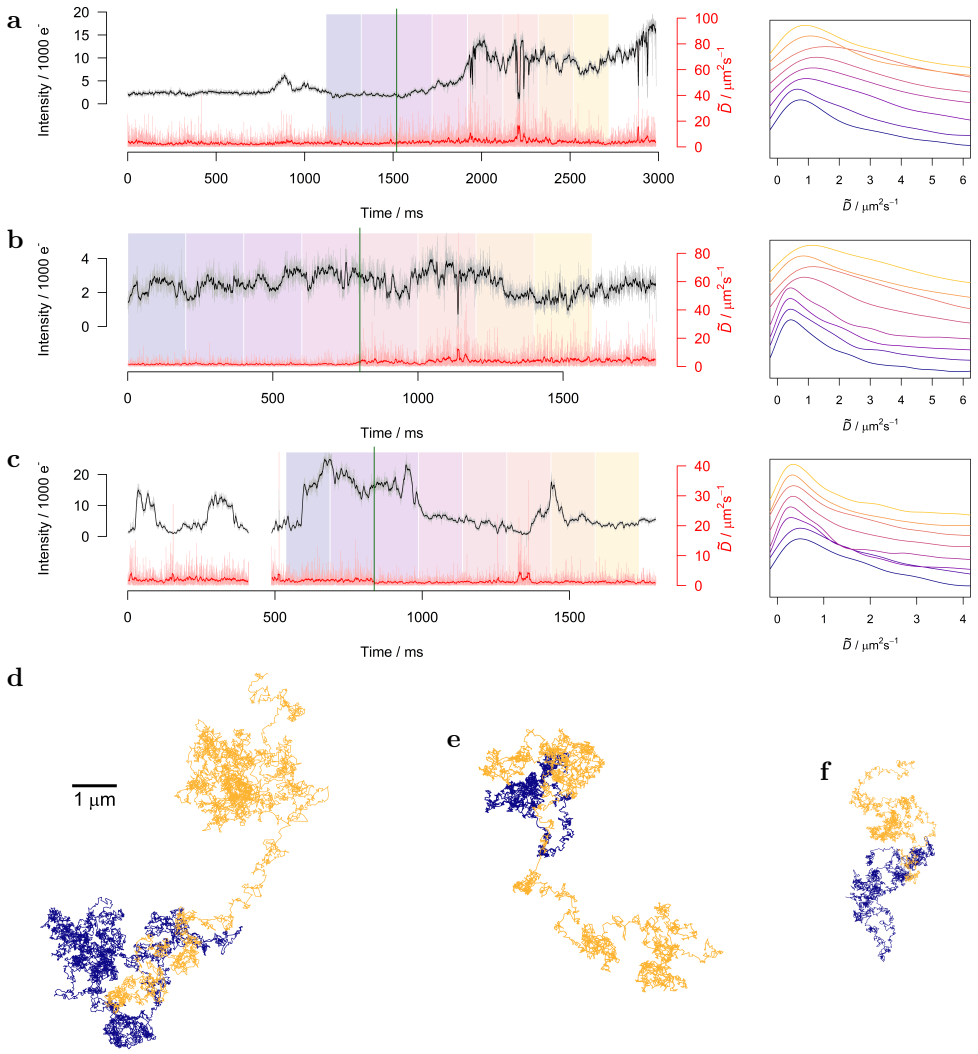


Figure 5.13: Transitions between diffusive states at DDM interfaces, all sampled at 5 kHz. a)-b) 20 nm gold particles before desorption. Note the intensity dips in the faster segments. c) A 40 nm particle loosely adsorbed at a DDM interface. Left: Intensity and instantaneous diffusion coefficient as a function of time. Visually identified transition times are marked with a vertical line. Right: Density distribution of instantaneous diffusion coefficients of trajectory segments corresponding to shaded regions in the time trace. d-f) Corresponding in-plane trajectories, in blue before the transition and in orange afterwards.

The instantaneous diffusion coefficient distributions in Figs. 5.13a and 5.13b show accelerating diffusion before desorption events — this is especially sharp in Fig. 5.13b — and a slowing-down in Fig. 5.13c. In Fig. 5.13a, there is a clear difference between the first two shaded segments and the later ones. Interestingly, the increased instantaneous diffusion coefficient becomes visible before the onset of intensity dips.

If the transitions were caused by local changes in the properties of the interface, for example in DDM coverage, this would be visible in the in-plane trajectories. However, from Figs. 5.13d, 5.13e and 5.13f, this does not appear to be the case. It is noticeable that particles appear to leave the immediate area soon after the transition, but this is likely to be a consequence of the faster diffusion rather than its cause.

5.4 Summary and conclusions

The rarely observed events that clearly involve out-of-plane motion, such as adsorption events, demonstrate clearly that the scattering intensity, instantaneous diffusion coefficient and height at the interface are related, supporting interpretations in chapter 4. Particles furthermore sample partially adsorbed states at DDM interfaces — validating the assumption that particles

at MQ interfaces straddle (rather than skim) the interface, and undergo little motion in z — and more generally exhibit a broader range of behaviours than at MQ interfaces. The different immersion states observed in this work are summarised in Fig. 5.14.

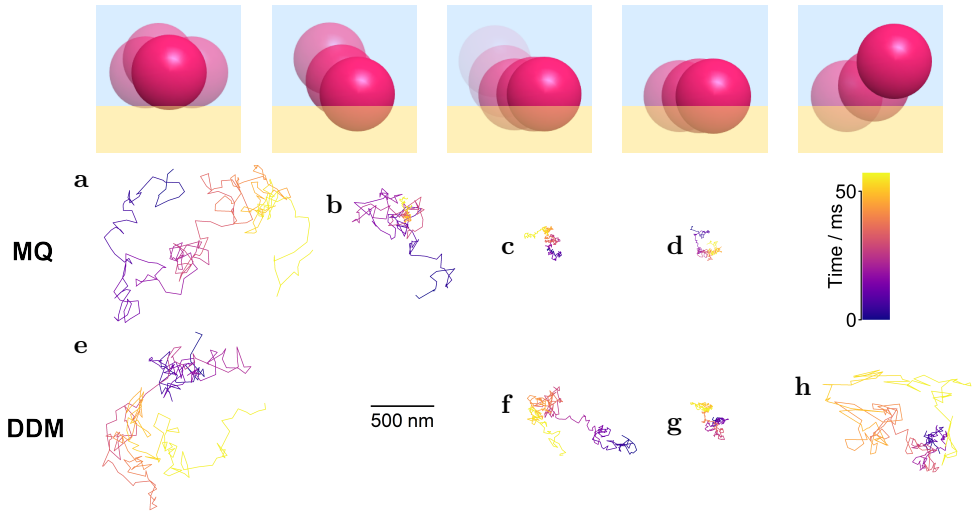


Figure 5.14: Representative in-plane trajectories of particles in different states at the interface. 40 nm particles sampled at 5 kHz at MQ (upper row) and DDM interfaces (lower row). From left to right: skimming, during adsorption, after adsorption, in what appears to be a fully adsorbed state, and in the case of the DDM particle during desorption. In the adsorption (b) and desorption (h) trajectories, the event occurs roughly in the centre of the trajectory.

Particles at DDM interfaces can move towards the water phase (and even desorb) as well as in the more typical direction towards the oil, and take a longer time to reach a fully adsorbed state after adsorption. This reversibility of immersion depth gain indicates that energy states are much

closer together at DDM interfaces, with a different dependence on particle size than at MQ interfaces. This is in keeping with the conclusions drawn in section 4.3, where interactions with surfactant molecules are proposed as an important factor in particle dynamics at DDM interfaces. The slow rate of change in the immersion depth and the sometimes abrupt transitions additionally indicate energetic barriers, i.e. metastable immersion states. These are likely associated with different configurations of the particle and surfactant molecules at the interface, possibly defined by inhomogeneities in the particle aligning with the interface.

6 Summary and future directions

This study shows that there are new and unexpected interfacial particle dynamics to be explored in systems with an added surfactant, underlining how advantageously chosen and carefully optimised imaging methods can shed light on otherwise inaccessible dynamics.

The following sections briefly summarise this thesis, covering the preparation of interface samples, the imaging system and data analysis in section 6.1, observed particle dynamics and implications in section 6.2, and ending with an outlook on possible future experiments in section 6.3.

6.1 Methods

We prepared stable samples of functionalised gold nanoparticles (diameters 20, 40 and 80 nm) at water-on-oil interfaces, with and without a surfactant (DDM) added to the water phase (section 2.2.1). The interfaces had to be suitable for imaging with TIR-DF, which we achieved by placing oil into a thin copper ring on a thin glass slide and adding an aqueous solution of particles to the top of the sample, with the water phase contained by a

silicone structure forming a seal with the glass slide. Critical factors were a small spatial extent between the interface and the microscopy coverslip holding the sample, adding a suitable amount of oil (i.e., enough to stop the interface from collapsing, and a small enough amount to produce a planar interface) and keeping contamination to a minimum.

We then used a TIR-DF microscope to image the particles (section 2.3): A laser beam was directed at the sample at an angle that resulted in total internal reflection at the interface, illuminating only the interface and a small volume above and below it and thereby minimising background light. The scattered light, mostly from particles because of their optical properties and the efficient background suppression of the setup, was imaged onto a high-speed camera. We achieved a spatiotemporal resolution of 1 nm and 20 μs, but could only image the least-scattering 20 nm particles at time steps of down to 80 μs at our maximum laser power density of $\approx$25 kW/cm^2. The cutting-edge spatiotemporal resolution enabled us to track dynamics that would otherwise have been impossible to image, including rapid adsorption and desorption events, skims and partially adsorbed particles undergoing sometimes very brief (600 μs and likely shorter) flights in a less deeply immersed state.

To obtain readily quantifiable data from the raw images, we analysed the image data by tracking the particles with a Gaussian-fit model and linking trajectories based on proximity and similarity in brightness in consecutive frames (section 3.2.2). The resulting diffusive and scattering behaviour, other properties such as trajectory length and deviations from ensemble behaviour, and correlations between properties were assessed within individual trajectories as well as within trajectory ensembles (section 3.1). We wrote our own analysis software for this, as requirements changed with our understanding of the data and could not be readily fulfilled by existing software.

6.2 Results and implications

At surfactant-free (MQ) interfaces, adsorption is rapid ($\lesssim 100$ μs) and no relaxation to equilibrium was observed. No desorption events were observed. At DDM interfaces, both adsorption and desorption events were recorded, indicating a significantly lower interfacial stabilisation energy. This is expected from the addition of a surfactant. However, larger particles were found to adsorb to DDM interfaces significantly less frequently than to MQ interfaces, with 80 nm particles hardly adsorbing at all — despite larger particles usually stabilising interfaces more than smaller ones, as they remove

a larger interfacial area given the same contact angle.

Particles at DDM interfaces also differ from their counterparts at MQ interfaces in other ways: Larger particles exhibit significantly faster diffusion, and a proportional increase in relative fluctuations in scattering intensity with particle size implies more out-of-plane motion (the values do not change significantly with particle size at MQ interfaces). Differently shaped step-size distributions (power-law tails), increased deviation from ensemble averages (ergodicity-breaking) and confined diffusion in these particles are also linked to both generally higher mobility perpendicular to the interface and a larger number of transitions between immersion states, including adsorption and desorption events.

Lastly, some particles at DDM interfaces exhibit dynamics that we did not observe at MQ interfaces. Partially adsorbed states are common, and the faster-diffusing of these states often feature brief flights through the water phase, with duration increasing with particle size. Some trajectories contain abrupt transitions between immersion states.

These findings lead us to propose competition between particles and surfactant molecules for space at the interface as the mechanism inhibiting adsorption of larger particles to DDM interfaces (see Fig. 6.1), preventing

them from becoming deeply embedded in the interface when they do attach and affecting their lateral as well as vertical dynamics (Fig. 6.1a). If our interpretation is correct, this could open an avenue to replacing larger particles at interfaces with smaller ones, in a reversal of the typical behaviour in which larger particles displace smaller ones in systems with mixed particle sizes [22] (Fig. 6.1b).

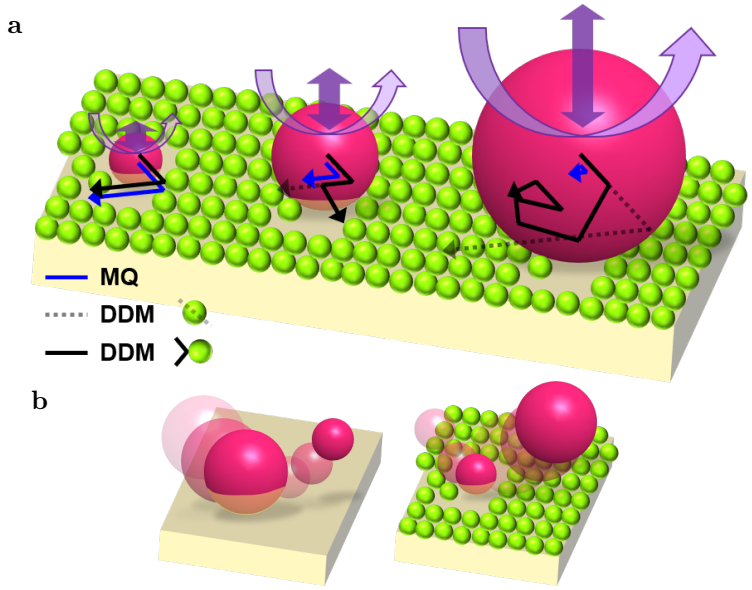


Figure 6.1: Changes in particle dynamics caused by the addition of a surfactant. a) 20, 40 and 80 nm particles at identical gaps in a surfactant layer at the interface: At DDM interfaces, black arrows represent in-plane motion — confinement by surfactant molecules taken into account (solid), and not (dotted and transparent) — and straight purple arrows out-of-plane motion. Dynamics at MQ interfaces are shown using blue arrows. Besides different diffusive behaviours when adsorbed to the interface, larger particles experience barriers to adsorption at DDM interfaces (curved purple arrows). b) At MQ interfaces, larger particles displace smaller particles, and at DDM interfaces, this trend is likely to be reversed.

Dense coverage of the interface with surfactant molecules both reduces the thermodynamic driving force for particle adsorption by lowering the interfacial tension, and may pose a kinetic and statistical barrier to adsorption, with the added requirement for surfactant molecules to move aside during the adsorption process, or for particles to encounter a sufficiently large vacant area. The shallow immersion resulting from an incomplete adsorption would lead to the observed faster diffusion, as a larger proportion of the particle is immersed in the less viscous water phase. In addition, locally varying resistance from surfactant molecules may lead to confined in-plane diffusion. Multiple metastable immersion states, closely spaced in energy, can explain the observed increase in out-of-plane motion, transitions between diffusive and scattering states, and the different step-size distributions and ergodicity-breaking — the observation of abrupt transitions indicates distinct energy minima, close enough together to allow thermally induced transitions between them. The increase with particle size of the duration of flights through more shallowly immersed states is in agreement with barriers to adsorption for larger particles.

Interestingly, the lateral diffusion in 20s and 40s is not much faster despite the expected lower contact angle and the observed reduced scattering intensity. A reason for this could be increased motion perpendicular to the

interface, increasing the dimensionality of the diffusion and thereby distributing the same thermal energy over more degrees of freedom. Another possible reason is an increase in the effective viscosity of the interface by the presence of surfactant molecules, resulting in slower lateral diffusion at a given immersion depth.

6.3 Future directions

Our findings demonstrate that there are unexplored, but technologially relevant dynamics in systems including mixtures of particles and surfactants, with surfactants considerably altering the particle dynamics. Varying the surfactant concentration, adding salt and otherwise testing expanding the range of experimental conditions would shed more light on the mechanisms behind these dynamics, and is likely to provide insights that will enable more control in applications. Investigating the dynamics of mixtures of different particle sizes would similarly be likely to yield new insights, with no changes to the experimental setup required.

In addition, it would be possible to probe the potential energy landscape of the interface using methods very similar to ours, which could be used to establish whether the anomalously slow diffusion observed by us and others at

surfactant-free interfaces can be explained by the effects of the line tension or other causes, and quantitatively investigate the dynamics observed at DDM interfaces. We attempted a semi-quantitative approach to determining a potential energy landscape by assuming a relationship between intensity and z position (see section 7.4 in the appendix), but could not obtain significant results as our method does not offer a quantitative relationship between the intensity and z. In future experiments, we could capture the z position of the particle by adding a cylindrical lens to our imaging system, causing the optical signal of particles to change as a function of the displacement from the interface. This three-dimensional spatial information could contribute greatly to the characterisation of the relationship between the structure of the composite system and its properties, deepening scientific understanding and opening new pathways in the design of functional materials.

References

[1] B. P. Binks, *Langmuir* **2017**, *33*, *28*, 6947.

[2] A. Imhof and D. J. Pine, *Nature* **1997**, *389*, 948.

[3] J. Tang, P. J. Quinlan and K. C. Tam, *Soft Matter* **2015**, *11*, *18*, 3512.

[4] Y. Hu, Y. Yang, C. Wang and Z. Tong, *Colloids Surf. B* **2013**, *112*, 96.

[5] H.-L. Cheng and S. S. Velankar, *Langmuir* **2009**, *25*, *8*, 4412.

[6] L. Hu, M. Chen, X. Fang and L. Wu, *Chem. Soc. Rev.* **2012**, *41*, 1350.

[7] V. J. Anderson and H. N. W. Lekkerkerker, *Nature* **2002**, *416*, 811.

[8] R. Metzler, *J. Stat. Mech.* **2019**, 114003.

[9] F. Bresme and M. Oettel, *J. Phys.: Condens. Matter* **2007**, *2007*, 413101.

[10] T. Moschakis, *Curr. Opin. Colloid Interface Sci.* **2013**, *18*, *4*, 311.

[11] A. E. Nel, L. Mädler, D. Velegol, T. Xia, E. M. V. Hoek, P. Somasundaran, F. Klaessig, V. Castranova and M. Thompson, *Nat. Mater.* **2009**, *8*, 543.

[12] Y. Yang, Z. Fang, X. Chen, W. Zhang, Y. Xie, Y. Chen, Z. Liu and W. Yuan, *Front. Pharmacol.* **2017**, *8*, 287.

[13] M. Peter, N. S. Binulal, S. V. Nair, N. Selvamurugan, H. Tamura and R. Jayakumar, *Chem. Eng.* **2010**, *158*, 353.

[14] T. Gong, J. Xie, J. Liao, T. Zhang, S. Lin and Y. Lin, *Bone Res.* **2015**, *3*, 15029.

[15] J. Frelichowska, M.-A. Bolzinger, J.-P. Valour, H. Mouaziz, J. Pelletier and Y. Chevalier, *Int. J. Pharm.* **2009**, *368*, 7.

[16] J. Marto, L. Gouveia, I. M. Jorge, A. Duarte, L. M. Gonçalves, S. M. C. Silva, F. Antunes, A. A. C. C. Pais, E. Oliveira, A. J. Almeida and H. M. Ribeiro, *Colloids Surf. B* **2015**, *135*, 183.

[17] K. Stratford, R. Adhikari, I. Pagonabarraga, J. C. Desplat and M. E. Cates, *Science* **2005**, *309*, *5744*, 2198.

[18] J. A. Witt, D. R. Mumm and A. Mohraz, *J. Mater. Chem. A*, **2016**, *4*, 1000.

[19] S. Cha, H. G. Lim, M. F. Haase, K. J. Stebe, G. Y. Jung and D. Lee, *Sci. Rep.* **2019**, *9*, 6363.

[20] S. Shi and T. P. Russel, *Adv. Mater.* **2018**, *30*, 1800714.

[21] J. L. Plawsky, J. K. Kim and E. F. Schubert, *Mater. Today* **2009**, *12*, *6*, 36.

[22] Y. Lin, H. Skaff, T. Emrick, A. D. Dinsmore and T. P. Russell, *Science* **2003**, *299*, 226.

[23] S. Boncel, A. Kolanowska, A. W. Kuziel and I. Krzyżewska, *ACS Appl. Nano Mater.* **2018**, *1*, *12*, 6542.

[24] C. K. Chan, H. Peng, G. Liu, K. McIlwrath, X. F. Zhang, R. A. Huggins and Y. Cui, *Nat. Nanotechnol.* **2008**, *3*, 31.

[25] A. Tao, P. Sinsermsuksakul, P. Yang, *Nature Nano.* **2007**, *2*, 435.

[26] M. Sarovar, A. Ishizaki, G. R. Fleming and K. B. Whaley, *Nat. Phys.* **2010**, *6*, 462.

[27] S. Dasgupta, T. Auth and G. Gompper, *J. Phys.: Condens. Matter* **2017**, *29*, 373003.

[28] E. Guzmán and E. Santini, *Curr. Opin. Colloid Interface Sci.* **2019**, *39*, 24.

[29] E. Conticini, B. Frediani and D. Caro, *Environ. Pollut.* **2020**, *261*, 114465.

[30] Y. Cui, Z.-F. Zhang, J. Froines, J. Zhao, H. Wang, S.-Z. Yu and R. Detels, *Environ. Health* **2003**, *2*, 15.

[31] M. D. Lebowitz, *Eur. Respir. J.*, **1996**, *9*, 1029.

[32] Y. Cao, M. Chen, D. Dong, S. Xie and M. Liu, *Thorac. Cancer* **2020**, *11*, *3*, 505.

[33] *Nat. Nanotechnol.* **2019**, *14*, 299.

[34] K. Mattsson, E. V. Johnson, A. Malmendal, S. Linse, L.-A. Hansson and T. Cedervall, *Sci. Rep.* **2017**, *7*, 11452.

[35] S. Wilhelm, A. J. Tavares, Q. Dai, S. Ohta, J. Audet, H. F. Dvorak and W. C. W. Chan, *Nat. Rev. Mater.* **2016**, *1*, 16014.

[36] A. R. Bausch, M. J. Bowick, A. Cacciuto, A. D. Dinsmore, M. F. Hsu, D. R. Nelson, M. G. Nikolaides, A. Travesset and D. A. Weitz, *Science* **2003**, *299*, 1716.

[37] A. L. Thorneywork, J. L. Abbott, D. G. A. L. Aarts and R. P. A. Dullens, *Phys. Rev. Lett.* **2017**, *118*, 158001.

[38] B. Wang, J. Kuo, S. C. Bae and S. Granick, *Nat. Mater.* **2012**, *11*, 481.

[39] A. J. Mendoza, E. Guzmán, F. Martínez-Pedrero, H. Ritacco, R. G. Rubio, F. Ortega, V. M. Starov and R. Miller, *Adv. Colloid Interface Sci.* **2014**, *206*, 303.

[40] R. McGorty, J. Fung, D. Kaz and V. N. Manoharan, *Mater. Today* **2010**, *13*, *6*, 34.

[41] W. Ramsden, *Proc. R. Soc. London* **1903**, *72*, *477*, 156.

[42] S. U. Pickering, *J. Chem. Soc., Trans.*, **1907**, *91*, 2001.

[43] P. Pieranski, *Phys. Rev. Lett.*, **1980**, *45*, *7*, 569.

[44] D. Wang, R. Hu, M. J. Skaug and D. K. Schwartz, *J. Phys. Chem. Lett.* **2015**, *6*, 54.

[45] A. G. Kanellopoulos and M. J. Owen, *Trans. Faraday Soc.* **1971**, *67*, 3127.

[46] F. Peters and D. Arabali, *Coll. Surf. A* **2013**, *426*, 1.

[47] K. Du, J. A. Liddle and A. J. Berglund, *Langmuir* **2012**, *28*, 9181.

[48] G. Boniello, C. Blanc, D. Fedorenko, M. Medfai, N. Ben Mbarek, M. In, M. Gross, A. Stocco and M. Nobili, *Nat. Mater.* **2015**, *14*, 908.

[49] A. Wang, J. W. Zwanikken, D. M. Kaz, R. McGorty, A. M. Goldfain, W. B. Rogers and V. N. Manoharan, *Phys. Rev. E* **2019**, *100*, 042605.

[50] C. C. Miller, *Proc. R. Soc. A* **1924**, *106*, *740*, 724.

[51] J. T. Edwards, *J. Chem. Educ.* **1970**, *47*, *4*, 261.

[52] D. Wang, S. Yordanov, H. M. Paroor, A. Mukhopadhyay, C. Y. Li, H.-J. Butt and K. Koynov, *Small* **2011**, *7*, *24*, 3502.

[53] B. Wang, S. M. Anthony, S. C. Bae and S. Granick, *Proc. Nat. Ac. Sci.* **2009**, *106*, *36*, 15160.

[54] C. Xue, X. Zheng, K. Chen, Y. Tian and G. Hu, *J. Phys. Chem. Lett.* **2016**, *7*, 514.

[55] R. Metzler, *Eur. Phys. J. Spec. Top.* **2020**, *229*, 711.

[56] D. M. Kaz, R. McGorty, M. Mani, M. P. Brenner and V. N. Manoharan, *Nat. Mater.* **2012**, *11*, 138.

[57] A. Wang, W. B. Rogers and V. N. Manoharan, *Phys. Rev. Lett.* **2017**, *119*, 108004.

[58] M. Oettel and S. Dietrich, *Langmuir* **2008**, *24*, *4*, 1425.

[59] I. B. Liu, N. Sharifi-Mood and K. J. Stebe, *Annu. Rev. Condens. Matter Phys.* **2018**, *9*, 283.

[60] M. G. Nikolaides, A. R. Bausch, M. F. Hsu, A. D. Dinsmore, M. P. Brenner, C. Gay and D. A. Weitz, *Nature* **2002**, *420*, 299.

[61] P. Y. Kim, Y. Gao, Y. Chai, P. D. Ashby, A. E. Ribbe, D. A. Hoagland and T. P. Russell, *ACS Nano* **2019**, *13*, 3075.

[62] F. Giorgi, D. Coglitore, J. M. Curran, D. Gilliland, P. Macko, M. Whelan, A. Worth and E. A. Patterson, *Sci. Rep.* **2019**, *9*, 12689.

[63] A. Maestro, E. Santini, D. Zabiegaj, S. Llamas, F. Ravera, L. Liggieri, F. Ortega, R. G. Rubio and E. Guzman, *Adv. Cond. Matter Phys.* **2015**, 917516.

[64] B. B. Niraula, T. K. Chun, H. Othman and M. Misran, *Coll. Surf. A* **2004**, *248*, 157.

[65] R. Aveyard, B. P. Binks and J. H. Clint, *Adv. Colloid Interface Sci.* **2003**, *100*, 503.

[66] B. P. Binks, L. Isa and A. Terhemen Tyowua, *Langmuir* **2013**, *29*, *16*, 4923.

[67] J. Smits, F. Vieira, B. Bisswurn, K. Rezwan and M. Maas, *Langmuir* **2019**, *35*, 11089.

[68] C. Whitby, D. Fornasiero, J. Ralston, L. Liggieri and F. Ravera, *J. Phys. Chem. C* **2012**, *116*, *4*, 3050.

[69] R. Huang, I. Chavez, K. M. Taute, B. Lukić, S. Jeney, M. G. Raizen and E. L. Florin, *Nat. Phys.* **2011**, *7*, 576.

[70] S. Kheifets, A. Simha, K. Melin, T. Li and M. G. Raizen, *Science* **2014**, *343*, 1493.

[71] H. Shen, L. J. Tauzin, R. Baiyasi, W. Wang, N. Moringo, B. Shuang and C. F. Landes, *Chem. Rev.* **2017**, *117*, *11*, 7331.

[72] P. W. Winter and H. Shroff, *Curr. Op. in Chem. Biol.* **2014**, *20*, 46.

[73] J. Ortega-Arroyo, P. Kukura, *Phys. Chem. Chem. Phys.*, **2012**, *14*, 15625.

[74] R. W. Taylor, V. Sandoghdar, *Nano Lett.* **2019**, *19*, 4827.

[75] Y.-H. Lin, W.-L. Chang and C.-L. Hsieh, *Opt. Express* **2014**, *22*, *8*, 9159.

[76] H. Ueno, S. Nishikawa, R. Iino, K. Tabata, S. Sakakihara, T. Yanagida and H. Noji, *Biophys. J.* **2010**, *98*, 2014.

[77] Y. Sowa, B. C. Steel and R. M. Berry, *Rev. Sci. Instrum.* **2010**, *11*, 113704.

[78] P. K. Jain, K. S. Lee, I. H. El-Sayed and M. A. El-Sayed, *J. Phys. Chem. B* **2006**, *110*, *14*, 7238.

[79] A. L. Mattheyses and D. Axelrod, *J. Biomed. Opt.* **2006**, *11*, *1*, 014006.

[80] P. A. Kralchevsky, K. D. Danov, Interactions between Particles at a Fluid Interface, in: *Nanoscience: Colloidal and Interfacial Aspects*, V. M. Starov, Ed.; **2010**, CRC Press, New York, Chapter 15, 397.

[81] R. Walder and D. K. Schwartz, *Soft Matter* **2011**, *7*, 7616.

[82] R. B. Walder, A. Honciuc and D. K. Schwartz, *J. Phys. Chem. B* **2010**, *114*, 11484.

[83] R. B. Walder and D. K. Schwartz, *Langmuir* **2010**, *26*, *16*, 13364.

[84] M.-V. Meli, I-H. Lin and N. L. Abbott, *JACS* **2008**, *130*, 4326.

[85] R. Pesché and G. Nägele, *Phys. Rev. E* **2000**, *62*, *4*, 5432.

[86] M. D. Carbajal-Tinoco, R. Lopez-Fernandez and J. L. Arauz-Lara, *Phys. Rev. Lett.* **2007**, *99*, 138303.

[87] J. Larson, M. Kirk, E. A. Drier, W. O'Brien, J. F. MacKay, L. J. Friedman and A. A. Hoskins, *Nature Protocols* **2014**, *9*, *10*, 2317.

[88] R. E. Thompson, D. R. Larson and W. W. Webb, *Biophys. J.* **2002**, *82*, 2775.

[89] L. Li, M. Li, Z. Zhang and Z.-L. Huang, *J. Innov. Opt. Heal. Sci.* **2016**, *9*, *3*, 1630008.

[90] J. R. Janesick, *Photon Transfer: DN→ λ*, **2007**, SPIE Press, Washington, USA.

[91] R. Diekmann, K. Till, M. Müller, M. Simonis, M. Schüttpelz and T. Huser, *Scientific Reports* **2017**, *7*, 14425.

[92] B. Stuhrmann, M. Soares e Silva, M. Depken, F. C. MacKintosh and G. H. Koenderink, *Phys. Rev. E* **2012**, *86*, 020901(R).

[93] N. Chenouard, I. Smal, [...] and E. Meijering, *Nat. Methods* **2014**, *11*, 281.

[94] D. Wang, H. Wu and D. K. Schwartz, *Phys. Rev. Lett* **2017**, *119*, 268001.

[95] S. Kutuzov, J. He, R. Tangirala, T. Emrick, T. P. Russell and A. Böker, *Phys. Chem. Chem. Phys.* **2007**, *9*, 6351.

[96] D. C. Prieve and N. A. Frej, *Langmuir* **1990**, *6*, *2*, 396.

[97] L. Helden, K. Dietrich and C. Bechinger, *Langmuir* **2016**, *32*, *51*, 13752.

7 Appendix

7.1 Reduction of interfacial energy

Eqn. (1), neglecting the line tension, reduces to

$$\Delta E = \gamma_{1\mathrm{p}}\Delta A_{1\mathrm{p}} + \gamma_{2\mathrm{p}}\Delta A_{2\mathrm{p}} + \gamma_{12}\Delta A_{12}.$$

For a reference energy state in which the particle is fully immersed in phase 2,

$$\begin{aligned}\Delta E &= (\gamma_{1\mathrm{p}} - \gamma_{2\mathrm{p}})\Delta A_{1\mathrm{p}} + \gamma_{12}\Delta A_{12} \\ &= (\gamma_{1\mathrm{p}} - \gamma_{2\mathrm{p}})(2\pi R^2(1+\cos\theta)) - \gamma_{12}\pi R^2 \sin^2\theta \\ &= \pi R^2 \gamma_{12}(\frac{\gamma_{1\mathrm{p}} - \gamma_{2\mathrm{p}}}{\gamma_{12}} 2\pi R^2(1+\cos\theta) - \sin^2\theta). \qquad (34)\end{aligned}$$

Young's equation relates the equilibrium contact angle θ_0 to the interfacial tensions via $\cos(\theta_0) = \frac{\gamma_{2\mathrm{p}} - \gamma_{1\mathrm{p}}}{\gamma_{12}}$, resulting in

$$\Delta E = -\pi R^2 \gamma_{12} (2 \cos\theta_0 (1 + \cos\theta) + \sin^2\theta), \tag{35}$$

leading to the Pieranski equation (2) for $\theta = \theta_0$.

7.2 Time dependence of experimental variables

To investigate whether external conditions such as irradiation over an extended period of time or flows at the interface intensifying with evaporation (and therefore time) affect the measurements, we show aggregated data on diffusive behaviour in Fig. 7.1.

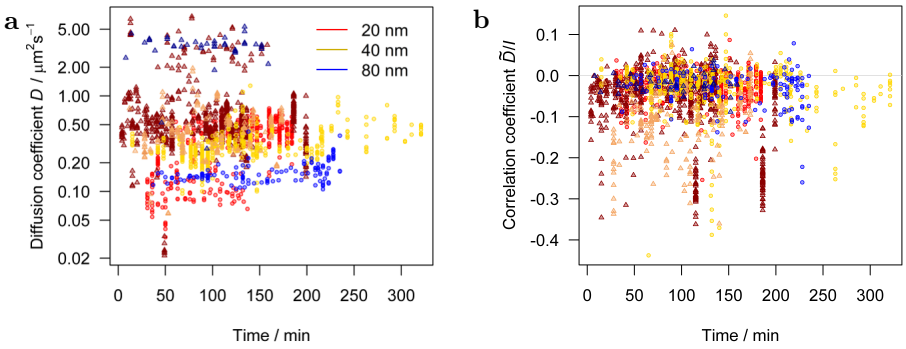


Figure 7.1: Time dependence of diffusive behaviour. Diffusion coefficient (a) and correlation coefficient between intensity and instantaneous diffusion coefficient (b) for each trajectory plotted against the time elapsed between the measurement and the making of the interface. Circles represent MQ interfaces and triangles DDM ones; the colours in the legend correspond to MQ particles and particles at DDM interfaces are represented in corresponding darker colours. Three of the 22 interfaces considered in Tab. 3 are not included because the time of making the interface is not known.

There is minor in-plane acceleration of particles at MQ interfaces over time.

7.3 Correlation between scattering intensity and instantaneous diffusion coefficient

Strong negative correlations were sometimes observed for particles with low intensities. Poor localisation precision can lead to an artificially increased instantaneous diffusion coefficient, which would result in an artificially lowered correlation. However, anti-correlations do not coincide with the lowest intensities (see Fig. 7.2), indicating clearly that localisation precision is not

the most important factor in the observation of negative correlation between intensity and instantaneous diffusion coefficient on an ensemble level.

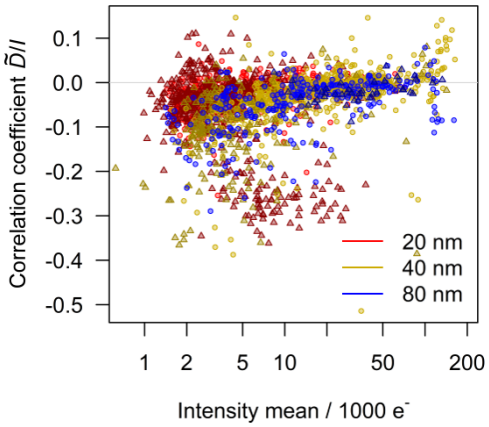


Figure 7.2: Correlation coefficient between intensity and instantaneous diffusion coefficient vs. trajectory-averaged intensity for the data in Tab. 3. Trajectories with mean intensities above ≈50 ke$^-$ are usually saturated at some times ($I = 2\pi(A-b)\sigma_x\sigma_y$ with maximal amplitude A, minimal amplitude offset b and point spread function standard deviations σ_i of 1.5 pixels yields 56 ke$^-$).

7.4 Towards probing the interfacial potential energy landscape

The relationship between the scattered intensity and the vertical position of the particle at the interface can, in principle, be used to derive the potential energy landscape experienced by the particle. The method has been employed in total-internal-reflection microscopy (TIRM) [96, 97] for 30 years,

as the illumination intensity, and consequently the intensity of the light scattered by the particle, is known to undergo an exponential decay above the interface. Relative energies are obtained by applying a Boltzmann model to the distribution of vertical positions.

We are not aware of a known quantitative relationship between the scattered intensity and the vertical position of a particle that is partially immersed in the phase from which the illumination occurs. We use both a linearly and an exponentially decaying function and compare the results to obtain qualitative information.

With z indicating the distance between the oil-facing end of the particle and the interface, the intensity of the evanescent field is given by

$$I = I_0 e^{-z/d}, \tag{36}$$

where d is the penetration depth given in Eqn. (11). d is not relevant to the energy distribution. The second model, scaling with the surface area of the particle that is in contact with the oil phase, is given by

$$I = -az, \tag{37}$$

where a is a factor that analogously to d is irrelevant to the energy distribution. From the z distributions obtained from these two models, the associated potential energies are obtained by fitting the data to a Boltzmann distribution:

$$p_i = \frac{1}{Q} e^{-\epsilon_i / k_\mathrm{B} T}, \tag{38}$$

where p_i is the probability of the state i with energy ϵ_i and Q is the sum of the energies of all states of the system. Consequently, the relative energy of a state within a trajectory is determined using

$$\epsilon_i = -k_\mathrm{B} T \ln p_i + \epsilon_0, \tag{39}$$

where the experimental distribution of p is given by the z values obtained from the scattering intensity. ϵ_0 is not measured. Ensemble-averaged results from our data are shown in Fig. 7.3.

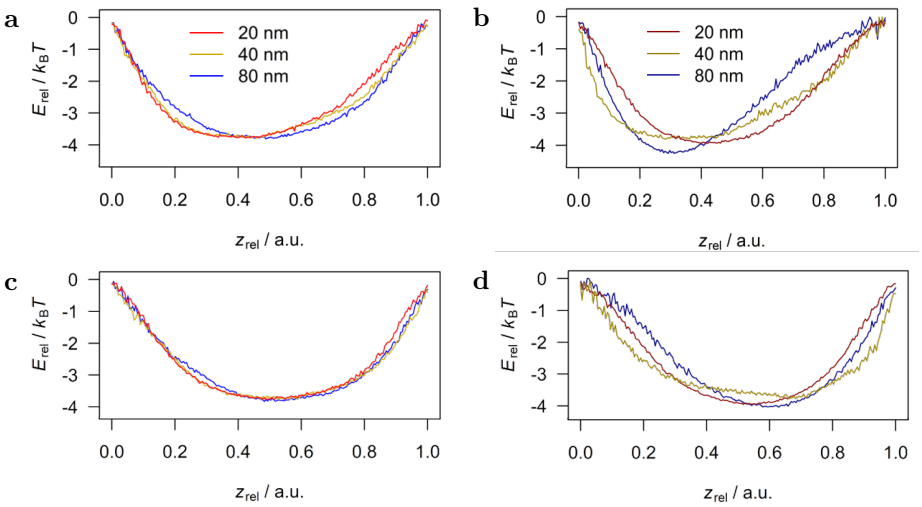


Figure 7.3: Relative potential energy vs. relative particle height at the interface; overlay of mean values using Eqns. (36) (a-b) and (37) (c-d). a) and c) contain MQ data; b) and d) DDM. Trajectories were split into segments of 5000 frames; sampling rate 12.5 kHz.

Irrespective of the intensity-position model, at DDM interfaces, there are more differences between particle sizes at DDM interfaces than at MQ interfaces, indicative of their more diverse behaviours. In the exponential model (Eqn. (36)), 80 and 40 nm particles at DDM interfaces, in particular, have different potential energy curves from the other particles, reflecting the difference noted in other parts of this thesis.